

Contents

Combination of Chemical and Biological Methods for Effective Plant Protection DÁVID VOZIK AND KATALIN BÉLAFI-BAKÓ	1–4
Enhancement of Oxygen Transfer Through Membranes in Bioprocesses PÉTER KOMÁROMY, KATALIN BÉLAFI-BAKÓ, ÉVA HÜLBER-BEYER, AND NÁNDOR NEMESTÓTHY	5–8
The Role of Water Activity in Terms of Enzyme Activity and Enantioselectivity During Enzymatic Esterification in Non-Conventional Media PIROSKA LAJTAI-SZABÓ, NÁNDOR NEMESTÓTHY, AND LÁSZLÓ GUBICZA	9–12
Follow-up Control of a Second Order System in Sliding Mode MÁRK DOMONKOS AND NÁNDOR FINK	13–21
Informative Environment Qualifying Index ANETT UTASI, VIKTOR SEBESTYÉN, AND ÁKOS RÉDEY	23–36
The Effect of pH on Biosurfactant Production by <i>Bacillus Subtilis</i> DSM10 RÉKA CZINKÓCZKY AND ÁRON NÉMETH	37–43
Adsorption of Nickel Ions From Petroleum Wastewater Onto Calcined Kaolin Clay: Isotherm, Kinetic and Thermodynamic Studies ALEXANDER ASANJA JOCK, ANIETIE NDARAKE OKON, UCHECHUKWU HERBERT OFFOR, FESTUS THOMAS, AND EDMOND OKWUDILICHUKWU AGBANAJE	45–49
Considerations to Approach Membrane Biofouling in Microbial Fuel Cells SZABOLCS SZAKÁCS AND PÉTER BAKONYI	51–53
New Chaining Criteria in Dipolar Fluids Based on Monte Carlo Simulations SÁNDOR NAGY	55–58
Temperature and Electric Field Dependence of the Viscosity of Electrorheological (ER) Fluids: Warming Up of an Electrorheological Clutch SÁNDOR MESTER AND ISTVÁN SZALAI	59–64

COMBINATION OF CHEMICAL AND BIOLOGICAL METHODS FOR EFFECTIVE PLANT PROTECTION

DÁVID VOZIK¹ AND KATALIN BÉLAFI-BAKÓ*¹

¹Research Institute on Bioengineering, Membrane Technology and Energetics, University of Pannonia, Egyetem u. 10, Veszprém, 8200, HUNGARY

The application of combined biological and chemical techniques to control undesirable processes in plant cultivation is becoming ever more important to maintain sustainable and environmentally friendly agricultural systems. Entomopathogenic nematodes and bacteria can provide an effective and special technology in the field of plant protection.

Keywords: antimicrobial, entomopathogenic nematodes, bacteria

1. Introduction

Nowadays, one of the most important challenges worldwide is the sufficient cultivation of edible plants and crops due to the rising trend in population growth and food demand. Moreover, it is important to solve this problem by implementing sustainable agriculture which prefers natural protection and tries to minimize the intervention of radical chemicals. It was confirmed recently that some synthetic pesticides are environmental hazards. Since the biological degradation of certain pesticides is slow, their bioaccumulation might cause significant damage to ecosystems, soil, natural waters, etc. Therefore, the idea of protecting crops has been extended and a new concept, “Integrated Pest Management” (IPM), introduced which involves chemical, biological and biotechnological methods together with modern cropping, cultivation and breeding technologies [1] in a way which minimizes any risk of environmental damage.

To apply this concept in practice requires comprehensive knowledge of the crops, fitopathogenic microorganisms as well as their enemies, and the behaviour of chemicals (e.g. pesticides) that may be used. A field that has hardly been researched are the so-called entomopathogenic nematodes and bacteria which have been studied in Hungary for a significant period of time [2].

2. Entomopathogenic nematodes and bacteria

Entomopathogenic nematodes are a group of thread worms that kill certain insects. They enter – in the form of infective juveniles – into the insects, live as parasites

inside them and cause host mortality within 1-2 days. It has turned out, however, that this is not only caused by the nematodes themselves but certain bacteria play an important role as well.

Entomopathogenic bacteria live in symbiosis with entomopathogenic nematodes [3,4]. The nematodes provide shelter for the bacteria, an area of the interior part of the intestine of the infective juveniles is transformed into a bacterial chamber where cells of symbiotic bacteria are located. The relationship is highly specific: e.g. the nematodes of *Steinernema* usually carry species of *Xenorhabdus* bacteria, while *Heterorhabditis* carry *Photorhabdus* bacteria.

When entering an insect, infective juveniles release the bacteria, which start multiplying rapidly in the haemolymph. It has been proven that although the bacteria are primarily responsible for the mortality of the insect host, the nematodes also produce a toxin which is lethal to the insect. These nematode-bacteria complexes can be applied successfully as biological control agents against insect pests in agriculture [5]. Some of these agents are available commercially, as listed in Table 1, where the target insects, habitats and places of usage are presented [6–8].

3. Antimicrobial compounds

Entomopathogenic bacteria contribute not only to the successful activity of entomopathogenic nematodes but can produce special compounds with an antimicrobial effect as well. The main purpose of producing these compounds is to protect the colonized cadaver in the soil [9]. The antimicrobial compounds of entomopathogenic bacteria have been tested and it would seem that these natural agents show a wide range of bioactivities of medical and

*Correspondence: bako@almos.uni-pannon.hu

Table 1: Examples of the successful application of nematode-bacteria complexes [6–8]

	Target	Habitat	Where
Japanese beetle	<i>Popillia japonica</i>	subterranean	lawn, turf
black vine weevil	<i>Otiorhynchus sulcatus</i>	subterranean	strawberry plants
fungus gnats	<i>Lycoriella</i> species, <i>Bradysia</i> species	subterranean	mushroom production
diaprepes root weevil	<i>Diaprepes abbreviatus</i>	epigeal	citrus
invasive mole cricket	<i>Scapteriscus vicinus</i>	epigeal	lawn, turf
codling moth	<i>Cydia pomonella</i>	cryptic	apple, pome fruit

Table 2: Plant pathogens tested

Pathogen	Effect	Ref.
<i>Phytophthora nicotianae</i>	root rot disease of tobacco	[13]
<i>Erwinia amylovora</i>	fire blight disease of several plants that belong to Rosaceae, e.g. apple, pear, etc.	[14]
<i>Ralstonia solanacearum</i>	brown rot disease of potato	[15]

agricultural interest, e.g. antibiotic, antimycotic and insecticidal effects [10,11]. For analytical purposes, Fourier Transform Infrared spectrometry (FTIR) was used to identify these compounds [12].

In our laboratories, secondary metabolites of *Xenorhabdus budapestiensis* (isolated in Hungary) have been investigated [13]. The bacterium was maintained on a Luria Agar (LA) medium and freshly subcultured. The cells were cultured in 1000 mL flasks and incubated on a gyrorotary shaker at 25 °C. Then the cells were removed by centrifugation and the supernatant extracted. The cell-free filtrate was further purified by chemical methods (adsorption and filtration) to obtain a peptide-rich fraction. This fraction was applied to test for various plant pathogens, as listed in Table 2, including pathogens of tobacco, apple and potato (the latter of which is widespread in Hungary, causing serious damage to inland agriculture).

The investigations involved *in vitro* bioassays, where the antibacterial activity of the biofraction was determined on solid media. In an agar diffusion test, the tested bacterium was mixed with soft agar poured onto LA plates, then a small hole was made in the centre and the biopreparation of the filtrate added [13]. For the so-called overlay test [13], the antimicrobial preparation was incubated on the solid Luria Broth Agar (LA) plate then the pathogenic microorganism in soft agar was spread onto the surface. In both cases, an inhibition zone can be identified and determined, if the biopreparation was effective against the pathogenic strain. An example of the agar diffusion bioassay is given in Fig. 1. A picture taken from a successful overlay bioassay test is shown in Fig. 2. In our laboratory, *in vitro* bioassays proved that the biopreparations containing the antimicrobial compounds could be successfully used against these pathogens.

Moreover, *in planta* (in field trials), a bioassay was conducted using infected apple blossom (*Erwinia amylovora*) which was treated with the biopreparation. It was concluded to be suitable to reduce the symptoms of the infected plants, thus it can be considered as a promis-

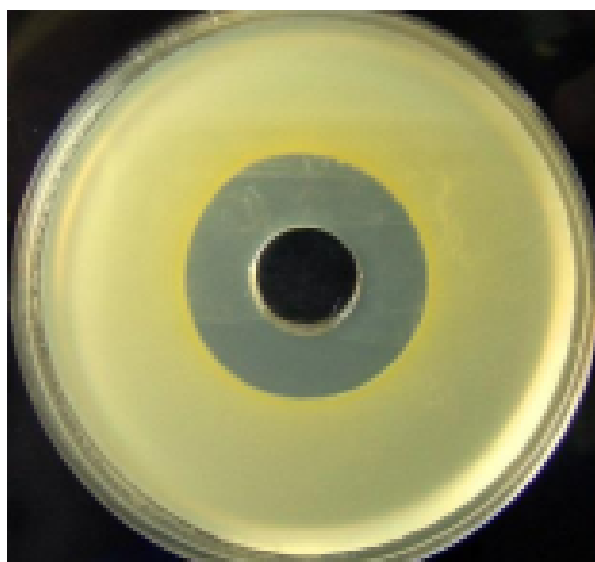


Figure 1: Antibacterial effect of the preparation in the agar diffusion test.

Figure 2: The antagonistic effect of *X. budapestiensis* against *E. amylovora* EA1 bacteria in an overlay test.



Figure 3: Infected apple blossom treated with the bio-preparation.

ing biological agent [14, 15]. This successful treatment is illustrated in Fig. 3.

Other than plant pathogens, the peptide-rich fraction of *Xenorhabdus budapestiensis* has recently been tested against species of fungi in vitro [16] in clinical samples. *Candida albicans*, *Candida lusitanae*, *Candida krusei*, *Candida kefyr*, *Candida tropicalis* and *Candida glabrata* were used in the research by applying the agar diffusion method. The results proved that every *Candida* species is sensitive to the preparation, thus it would seem that the fraction has a fungicide impact as well.

4. Conclusion

In summary, the symbiotic complex of entomopathogenic nematodes and bacteria can be considered as efficient biological agents to control some insect pests, but the secondary metabolites of the bacteria can be effectively used against other pathogenic bacteria and fungi. As a result, their applications can contribute significantly to successful plant protection by providing numerous environmental benefits and can be considered as an important component of “Integrated Pest Management” (IPM).

REFERENCES

- [1] Act XXXV on plant protection (2000, Hungary) http://www.kvvm.hu/szakmai/hulladekgazd/jogsabalyok/2000_XXXV_tv.htm
- [2] Lengyel, K.; Lang, E.; Fodor, A.; Szállás, E.; Schumann, P.; Stackebrandt, E.: Description of four novel species of *Xenorhabdus*, family *Enterobacteriaceae*: *Xenorhabdus budapestensis* sp. Nov., *Xenorhabdus ehlersii* sp. nov., *Xenorhabdus innexi* sp. nov., and *Xenorhabdus szentirmaii* sp. nov., *Syst. Appl. Microbiol.* 2005, **28**(2), 115–122 DOI: 10.1016/j.syapm.2004.10.004
- [3] Boemare, N. E.; Akhurst, R. J.; Mourant, R. G.: DNA relatedness between *Xenorhabdus* spp. (Enterobacteriaceae), symbiotic bacteria of entomopathogenic nematodes, and a Proposal to transfer *Xenorhabdus luminescens* to a new genus, *Photorhabdus* gen. nov., *Int. J. Syst. Bacteriol.* 1993, **43**(2), 249–255 DOI: 10.1099/00207713-43-2-249
- [4] Thomas, G. M.; Poinar, G. O.: *Xenorhabdus* gen. nov., a genus of entomopathogenic, nematophilic bacteria of the family *Enterobacteriaceae*, *Int. J. Syst. Bacteriol.* 1979, **29**(4), 352–360 DOI: 10.1099/00207713-29-4-352
- [5] Smart, G. C.: Entomopathogenic nematodes for the biological control of insects, *J. Nematology* 1995, **27**(4S), 529–553 <https://www.ncbi.nlm.nih.gov/pmc/articles/PMC2619649/pdf/529.pdf>
- [6] Koppenhöfer, A. M.: Nematodes, in Lacey, L.A.; Kaya, H.K. (Eds.): Field manual of techniques in invertebrate pathology. Application and evaluation of pathogens for control of insects and other invertebrate pests (Springer, Dordrecht, The Netherlands) 2007, ISBN: 978-1-4020-5933-9
- [7] Georgis, R.; Koppenhöfer, A. M.; Lacey, L. A.; Bélair, G.; Duncan, L. W.; Grewal, P. S.; Samish, M.; Tan, L.; Torr, P.; van Tol, R. W. H. M.: Successes and failures in the use of parasitic nematodes for pest control, *Biol. Control* 2006, **38**(1), 103–123 DOI: 10.1016/j.biocontrol.2005.11.005
- [8] Lacey, L. A.; Georgis, R.: Entomopathogenic nematodes for control of insect pests above and below ground with comments on commercial production, *J. Nematology* 2012, **44**(2), 218–225 <https://www.ncbi.nlm.nih.gov/pmc/articles/PMC3578470/pdf/218.pdf>
- [9] Akhurst, R. J.: Antibiotic activity of *Xenorhabdus* spp., bacteria symbiotically associated with insect pathogenic nematodes of the families Heterorhabditidae and Steinernematidae, *J. Gen. Microbiol.* 1982, **128**(12), 3061–3065 DOI: 10.1099/00221287-128-12-3061
- [10] McInerney, B. V.; Gregson, R. P.; Lacey, M. J.; Akhurst, R. J.; Lyons, G. R.; Rhodes, S. H.; Smith, D. R.; Engelhardt, L. M.; White, A. H.: Biologically active metabolites from *Xenorhabdus* spp., Part 1. Dithiopyrrolone derivatives with antibiotic activity, *J. Nat. Prod.* 1991, **54**(3), 774–784 DOI: 10.1021/np50075a005
- [11] Webster, J. M.; Chen, G.; Hun, K.; Li, J.: Bacterial metabolites, In: Gaugler, R. (Ed.) Entomopathogenic Nematology (CABI Publishing, New York, USA) 2002, 145–168 ISBN: 08-5199-567-5
- [12] Vozik, D.; Madarász, J.; Csanádi, Zs.; Fodor, A.; Dublec, K.; Bélafi-Bakó, K.: Study on analysis of antibiotic compounds from entomopathogenic bacteria by FT-IR, *Hung. J. Ind. Chem.* 2012, **40**(2), 83–86 <https://mk.uni-pannon.hu/hjic/index.php/hjic/article/download/346/316>
- [13] Böszörményi, E.; Érsek, T.; Fodor, A.; Földes, L. Sz.; Hevesi, M.; Hogan, J. S.; Katona, Z.; Klein, M. G.; Kormány, A.; Pekár, Sz.; Szentirmai, A.; Sztaricskai, F.; Taylor, R. A. J.: Isolation and activity of

- Xenorhabdus* antimicrobial compounds against the plant pathogens *Erwinia amylovora* and *Phytophthora nicotianae*, *J. Appl. Microbiol.* 2009, **107**(3), 746–759 DOI: [10.1111/j.1365-2672.2009.04249.x](https://doi.org/10.1111/j.1365-2672.2009.04249.x)
- [14] Vozik, D.; Bélafi-Bakó, K.; Hevesi, M.; Böszörményi, E.; Fodor, A.: Effectiveness of a peptide-rich fraction from *Xenorhabdus budapestensis* culture against fire blight disease on apple blossoms, *Not. Bot. Horti Agrobot. Cluj-Napoca* 2015, **43**(2), 547–553 DOI: [10.15835/nbha4329997](https://doi.org/10.15835/nbha4329997)
- [15] Vozik, D.; Bélafi-Bakó, K.; Hevesi, M.; Böszörményi, E.; Polgár, Zs.; Fodor, A.: Effectiveness of antimicrobial compounds produced by entomopathogenic nematode symbiotic bacteria to control pests and bacterial plant diseases, *International Organization For Biological Control - West Palaearctic Regional Section Bulletin* 2016, **113** 17–21 ISBN: 978-92-9067-296-8
- [16] Burgetti-Böszörményi, E.; Németh, S.; Bélafi-Bakó, K.; Vozik, D.; Barcs, I.; Csima, Z.: The antifungal effect of *Xenorhabdus budapestensis* bacteria biopreparatum on some *Candida* species in vitro, *Dev. Health Sci.* 2018, **1**(7), 57–62 DOI: [10.1556/2066.2.2018.17](https://doi.org/10.1556/2066.2.2018.17)

ENHANCEMENT OF OXYGEN TRANSFER THROUGH MEMBRANES IN BIOPROCESSES

PÉTER KOMÁROMY ^{*1}, KATALIN BÉLAFI-BAKÓ¹, ÉVA HÜLBER-BEYER¹, AND NÁNDOR NEMESTÓTHY¹

¹Research Institute on Bioengineering, Membrane Technology and Energetics, University of Pannonia, Egyetem u. 10, Veszprém, 8200, HUNGARY

In several aerobic bioprocesses, it is extremely important to provide a sufficient amount of oxygen, which is a difficult task since the solubility of oxygen in aqueous systems, namely in water, is low. Thus oxygen transfer techniques should be designed, built, studied and operated very carefully in biosystems. Moreover, in certain cases, special techniques, e.g. involving membranes, must be applied. In this paper, three different bioprocesses are presented where oxygen was supplied by membrane aeration: wastewater treatment by microbial consortia (i), itaconic acid fermentation by a single microorganism (ii) and an oxidative enzyme catalytic process for the elimination of glucose (iii).

Keywords: biotechnology, aerobic microbes, silicone membrane, enzyme

1. Introduction

At the dawn of applied and industrial biotechnology, the use of engineering tools to establish reliable bioprocesses for manufacturing certain bioproducts was inevitable [1–4]. For the effective production of acetic acid, ethanol and later citric acid, etc. by biological processes, the technical skills and experience of chemical engineering were used together with microbiological knowledge and practices to establish *bioengineering* and *bioprocess engineering*.

Several bioprocesses require oxygen for various purposes, e.g., respiration, certain energy-producing metabolic pathways, direct oxidation, the oxidative degradation of some substrates, etc. [1–3]. Oxygen is usually supplied by surface aeration, bubble aeration (sparging), by entering oxygen or air directly, aeration combined with agitation or in airlift bioreactors. Regardless, oxygen is always transported from a gas stream to an unsaturated liquid [5]. The steps of this pathway are as follows and are outlined in Fig. 1:

- from the inside of the bubble to the surface (gas side) (1);
- through the boundary layer of the bubble (liquid side) (2);
- from the surface to the bulk liquid (broth) (3);
- from the bulk liquid to the liquid film layer of the cell (4);

- into the microbial cells (through the liquid film layer) (5).

Moreover, it is important to take into consideration that the oxygen demand changes as a function of time and according to the characteristics of the particular form of cell.

In the liquid film layers, the transfer occurs by diffusion, while in the bulk phase, it always takes place via convective transport (which can be enhanced by mixing). The rate-limiting step is diffusion through the boundary film layer of the bubble on the liquid side, which is highly influenced by its surface area.

On the other hand, membranes have been used in bioprocesses for an extensive period of time [6–9]. However, firstly they were exclusively applied for separations [6–8]. Membranes that are distinctly selective towards certain gases were used to develop gas separation techniques. Some of these membranes are permeable to oxygen molecules in the gaseous phase, therefore, it was a breakthrough to apply them for oxygen transfer into the aqueous (liquid) phase [9]. One of the most important benefits of this kind of aeration is the amplified surface area between the gaseous (air or pure oxygen) and liquid phases.

In this work, three different bioprocesses are presented where oxygen was supplied by membrane aeration:

- wastewater treatment by microbial consortia;
- fermentation by a single microorganism (under sterile conditions) for the manufacture of an organic

*Correspondence: komaromy.peter@mk.uni-pannon.hu

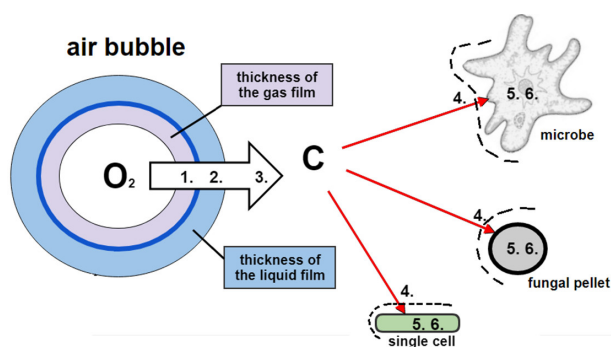


Figure 1: The pathway of oxygen transfer.

acid;

- an enzymatic oxidation for the elimination of glucose.

2. Membrane-aerated bioreactors for the treatment of wastewater

The combination of membrane technology with the biological treatment of municipal and industrial wastewater has been investigated and applied for an extensive period of time. Coupling the two systems resulted in a special, new type of reactor called a membrane bioreactor (MBR). The roles of membranes in these biological systems include:

- separation of solids;
- aeration;
- extraction of special pollutants.

The supply of oxygen to microbes through a membrane is carried out by a membrane-aerated bioreactor (MABR). This type of bioreactor was developed in 1978 and has been studied ever since. The membrane itself has to exhibit a high degree of oxygen permeability. Among gas-separation membranes, silicone (polydimethylsiloxane) was used for oxygen enrichment (from air), thus seemed suitable for this purpose. Oxygen mass transfer through a silicone membrane was closely examined [9] and it was determined that the membrane aeration system was approximately 7 times more effective in terms of oxygen supply than the standard activated sludge process, hence it was experimentally proven to have strong potential.

In different wastewater treatment processes, various gas-permeable membranes were tested with regard to oxygen supply systems [11–14]:

- polyethylene;
- ethyl cellulose;
- polystyrene;
- polytetrafluorethylene;
- polypropylene;

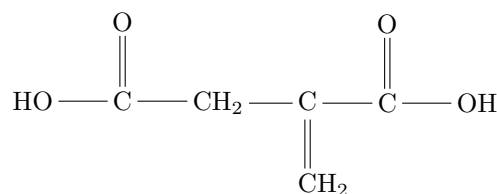


Figure 2: Chemical structure of itaconic acid.

- polyetherimide;
- silicone.

In terms of configuration, mainly hollow fibre modules were successfully applied (though plate-and-frame modules can also be used). The membrane was placed into the liquid waste (submerged system) and oxygen from the air was pumped inside the lumen. Oxygen was transferred by diffusion through the membrane directly into the biomass that formed on the shell side of the membrane. The main benefits of the system are that no bubbles are formed and bubble-to-liquid transfer (diffusion limitation) could be avoided.

The membrane aerated bioreactor system is continuously being developed and finally a truly reliable, robust and viable system was established [15], namely the ZeeLung system. It consists of a silicone, non-porous polymer membrane with an extremely small outer diameter (50–70 μm) and wall thickness (5–20 μm). Thus the module has a very high surface area, low packing density and an efficient rate of oxygen transfer can be maintained under low pressure. The new system (technology) resulted in an energy efficiency four times greater than that of conventional bubble aeration.

By comparing membrane aeration with traditional bubble aeration, another benefit can be recognized. A homogeneous oxygen concentration can be achieved throughout the reactor by pumping through air or oxygen bubbles. When membrane aeration is applied, it is possible to establish different oxygen levels within the reactor: several zones with various oxygen levels (as required for certain biological processes) can be created.

3. Fermentation of itaconic acid

Itaconic acid is an unsaturated five-carbon dicarboxylic acid that is considered to be an important platform molecule of high potential (bio-based building block) (Fig. 2). It was specified by the United States Department of Energy as one of the 12 most promising chemicals obtained from biomass.

Itaconic acid is mainly produced biologically by filamentous fungi, e.g. *Aspergillus terreus* [16–20].

The fermentation of itaconic acid is a quite sensitive process that requires a high initial substrate concentration of glucose, precise control of operational parameters (e.g. pH, temperature, presence/deficiency of certain ions, etc.) and a high oxygen level since a high level of oxygen tension in the fermenter enhances the formation of itaconic

acid. A sufficient oxygen supply can be ensured by increasing the mixing rate, however, filamentous fungi are generally very sensitive to high shear rates. Moreover, intensive foaming may result which must be avoided. As the fermentation progresses, ever more biomass and protein is produced in the broth, hence these phenomena may occur more acutely. In addition, the oxygen demand continuously increases.

Oxygen can be supplied by conventional techniques, e.g. airlift bioreactors, air bubbling equipped with propeller agitators, etc. For example, an airlift bioreactor was combined with a modified draft tube to achieve a high (2,430 l/h) volumetric oxygen transfer coefficient [21].

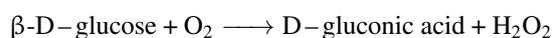
In our laboratory, membrane aeration was applied by pumping 600 l/h of air at a pressure of 1.1 bar into the broth by using a special PermSelect hydrofluoric acid (HF) silicone membrane which was immersed into the fermenter. This membrane was originally an oxygen-selective gas separation membrane, consisting of 10 thousand fibres (OD = 150 μm) with a surface area of 1 m². Since oxygen permeated faster than other compounds, it resulted in a high oxygen supply. Our successful experiments have proven that by applying membrane aeration, enhanced oxygen transport and a higher yield of itaconic acid are achieved.

4. Enzymatic removal of glucose

In the food industry, some processes require the removal of glucose [22]. For example, in the manufacture of powdered egg white, the reaction between glucose and protein results in the Maillard browning reaction during the spray-drying step, leading to an undesirable brown discoloration and poor quality [23]. Another example is the manufacture of low-calorie, low-alcohol beverages from fruit juices [24]. The content of fermentable sugar can be reduced significantly by converting it into other compounds which cannot be metabolised into ethanol (less alcohol forms).

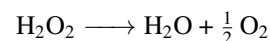
Glucose (or dextrose, its chemical name is D-glucopyranose) is the most abundant monosaccharide, a six-carbon sugar (hexose) with five hydroxyl groups. Its name is derived from the Greek word "glukos" which means "sweet".

The extraction of glucose from a mixture containing compounds of similar molecular size is generally difficult as well-known separation techniques are unsuitable [6–8]. Therefore, a special enzymatic method has been developed where glucose is oxidised. The enzyme catalysing the reaction is called glucose oxidase (GOD), E.C. 1.1.3.4 [25, 26]. During the reaction, glucose is converted into D-glucono-1,5-lactone, which spontaneously hydrolyses non-enzymatically into gluconic acid:



The reaction uses oxygen and releases hydrogen peroxide as a by-product, which has a strong inactivation effect on GOD itself, therefore, it must be eliminated

from the mixture. H₂O₂ can be converted into water and molecular oxygen by another enzyme called catalase, E.C. 1.11.1.6.:



The two enzymes can be applied together, such an enzyme mixture can be manufactured by various moulds, e.g., species of *Aspergillus*.

For the successful operation of the enzyme, a sufficient amount of oxygen should be supplied. In the case of the production of powdered egg white, traditional aeration methods (e.g. bubble aeration) cause a high degree of foaming, thus another technique should be implemented. In our laboratory, membrane aeration was studied and applied [27]. The enzyme complex was immobilized on a resin and a packed column reactor set up for the reaction. Then a perforated silicone tube membrane was placed inside the bioreactor in a spiral configuration to provide oxygen directly to the site of the enzymatic oxidation reaction.

5. Conclusion

In summary, three different bioprocesses were presented in this paper where oxygen was supplied using a special method, namely membrane aeration. Firstly, the treatment of wastewater by microbial consortia (i), secondly, the fermentation of itaconic acid by a single microorganism (ii) and finally, an oxidative enzymatic process (iii) for the elimination of glucose were examined in detail.

Acknowledgement

The research work was supported by the National Research, Development and Innovation Fund Project K 119940 entitled "Study on electrochemical effects on bio-product separation by electrodialysis" and project EFOP-3.6.1-16-2016-00016.

REFERENCES

- [1] Doran, P. M.: *Bioprocess Engineering Principles* (Academic Press, Waltham, Massachusetts, USA) 2013, ISBN: 978-00-8091-770-2
- [2] Ratledge, C.; Kristiansen, B. (Eds.): *Basic Biotechnology* (Cambridge University Press, Cambridge, UK) 2006, ISBN: 978-05-2154-958-5
- [3] Bailey, J. E.; Ollis, D. F.: *Biochemical Engineering Fundamentals* (McGraw Hill, New York, USA) 1986, ISBN: 978-00-7003-212-5
- [4] Atkinson, B.; Mavituna, F.: *Biochemical Engineering and Biotechnology Handbook* (The Nature Press, London, UK) 1983, ISBN: 0-333-33274-1
- [5] Komaromy, P., Sisak, Cs.: Investigation of gas-liquid oxygen transport in three-phase bioreactor, *Hung. J. Ind. Chem.* 1994, **22**(2), 147–151

- [6] Mulder, M.: Basic principles of membrane technology (Kluwer Academic Publisher, Dordrecht, The Netherlands) 1996, ISBN: 978-94-009-1766-8
- [7] Baker, R. W.: Membrane Technology and Applications (Wiley, New York, USA) 2012, ISBN: 978-04-708-5445-7
- [8] van Reis, R.; Zydney, A.: Membrane separations in biotechnology, *Current Opin. Biotechnology* 2001, **12**(2) 208–211 DOI: 10.1016/S0958-1669(00)00201-9
- [9] Charcosset, C.: Membrane Processes in Biotechnology and Pharmaceuticals (Elsevier, Amsterdam, The Netherlands) 2012, ISBN: 978-04-445-6334-7
- [10] Hirasa, O.; Ichijo, H.; Yamauchi, A.: Oxygen transfer from silicone hollow fiber membrane to water, *J. Ferm. Bioeng.* 1991, **71**(3), 206–207 DOI: 10.1016/0922-338X(91)90113-U
- [11] Irvine, R.; Sikdar, S. H.: Fundamentals and Application of Bioremediation: Principles (CRC Press, New York, USA) 1997, ISBN: 978-15-667-6308-0
- [12] Stephenson, T.; Brindle, K.; Judd, S.; Jefferson, B.: Membrane Bioreactors for Wastewater Treatment (IWA Publishing, London, UK) 2000, ISBN: 978-19-002-2207-5
- [13] Brindle, K.; Stephenson, T.: The application of membrane biological reactors for the treatment of wastewaters, *Biotechnol. Bioeng.* 1996, **49**(6), 601–610 DOI: 10.1002/(SICI)1097-0290(19960320)49:6<601::AID-BIT1>3.0.CO;2-S
- [14] Brepols, C.: Operating large scale membrane bioreactors for municipal wastewater treatment (IWA Publishing, London, UK) 2010, ISBN: 978-18-433-9305-4
- [15] Stricker, A. E.; Lossing, H.; Gibson, J. H.; Hong, Y.; Urbanic, J. C.: Pilot scale testing of a new configuration of the membrane aerated biofilm reactor (MABR) to treat high-strength industrial sewage, *Water Env. Res.* 2011, **83**(1), 3–14 DOI: 10.2175/106143009X12487095236991
- [16] Jang, Y. S.; Kim, B.; Shin, J. H.; Choi, Y. J.; Song, C. W.; Lee, J.; Park, H. G.; Lee, S. Y.: Bio-based production of C2-C6 platform chemicals, *Biotechnol. Bioeng.* 2012, **109**(10), 2437–2459 DOI: 10.1002/bit.24599
- [17] da Cruz, J. C.; Camporese Servulo, E. F.; de Castro, A. M.: Microbial production of itaconic acid, in Microbial production of food ingredients and additives in Handbook of Food Bioengineering Holban, A. M., Grumuzescu, A.M. (Eds.) (Academic Press, Elsevier, Amsterdam, The Netherlands) 2017, pp. 291–316, DOI: 10.1016/B978-0-12-811520-6.00010-6
- [18] Varga, V.; Bélafi-Bakó, K.; Vozik, D.; Nemestóthy, N.: Recovery of itaconic acid by electro dialysis, *Hung. J. Ind. Chem.* 2018, **46**(2), 43–46 DOI: 10.1515/hjic-2018-0017
- [19] Karaffa, L.; Diaz, R.; Papp, B.; Fekete, E.; Sandor, E.; Kubicek, C. P.: A deficiency of manganese ions in the presence of high sugar concentrations is the critical parameter for achieving high yields of itaconic acid by *Aspergillus terreus*, *Appl. Microbiol. Biotechnol.* 2015, **99**, 7937–7944 DOI: 10.1007/s00253-015-6735-6
- [20] Komáromy, P.; Bakonyi, P.; Kucska, A.; Tóth, G.; Gubicza, L.; Bélafi-Bakó, K.; Nemestóthy, N.: Optimized pH and its control strategy lead to enhanced itaconic acid fermentation by *Aspergillus terreus* on glucose substrate, *Fermentation*, 2019, **5**(2), 31–39 DOI: 10.3390/fermentation5020031
- [21] Okabe, M.; Ohta, N.; Park, Y. S.: Itaconic acid production in an air-lift bioreactor using a modified draft tube, *J. Ferm. Bioeng.* 1993, **76**(2), 117–122 DOI: 10.1016/0922-338X(93)90067-1
- [22] Varzakas, T.; Tzia, C.: Food Engineering Handbook, Food Process Engineering (CRC Press, Amsterdam, The Netherlands) 2014, ISBN: 978-14-665-8226-2
- [23] Kilara, A.; Shahani, K. M.: Removal of glucose from eggs: A review, *J. Milk Food Technol.* 1973, **36**(10), 509–514 DOI: 10.4315/0022-2747-36.10.509
- [24] Heresztyn, T.: Conversion of glucose to gluconic acid by glucose oxidase enzyme in Muscat Gordo juice, *The Australian Grapegrower and Winemaker*, 1987, **4**, 25–27
- [25] Sisak, Cs.; Csanádi, Z.; Rónay, E.; Szajáni, B.: Elimination of glucose in egg white using immobilized glucose oxidase, *Enzyme Microb. Technol.*, 2006, **39**(5), 1002–1007 DOI: 10.1016/j.enzmictec.2006.02.010
- [26] Pečar, D.; Vasić-Rački, Đ.; Presečki, V.: Immobilization of glucose oxidase on Eupergit C: Impact of aeration, kinetic and operational stability studies of free and immobilized enzyme, *Chem. Biochem. Eng. Q.* 2018, **32**(4), 511–522 DOI: 10.15255/CABEQ.2018.1391
- [27] Bélafi-Bakó, K.: Possibilities for removal of glucose from various foodstuffs and food bioprocesses, in New Topics in Food Engineering, Siegler, B.C. (Ed.) (Nova Science Publishers, New York, USA) 2010, pp. 289–299 ISBN: 978-161209599-8

THE ROLE OF WATER ACTIVITY IN TERMS OF ENZYME ACTIVITY AND ENANTIOSELECTIVITY DURING ENZYMATIC ESTERIFICATION IN NON-CONVENTIONAL MEDIA

PIROSKA LAJTAI-SZABÓ¹, NÁNDOR NEMESTÓTHY¹, AND LÁSZLÓ GUBICZA ^{*1}

¹Research Institute on Bioengineering, Membrane Technology and Energetics, University of Pannonia, Egyetem u. 10, Veszprém, 8200, HUNGARY

During enzymatic esterification in non-conventional media, the activity and enantioselectivity of the enzyme is significantly influenced by the water content of the reaction medium, which continuously changes as water is produced during the esterification. To provide constant reaction parameters, water activity should be kept constant. The commonly used salt hydrate pairs may be difficult to apply and often hinder enzyme activity. During the enantioselective esterification of racemic 2-bromopropanoic acid in various solvents (organic solvents, ionic liquids), it was proven that the conditions related to the optimal water content required for kinetic examinations can be provided without using any salt or salt hydrate pairs. This conclusion is based on the realization that the optimal water activity can be set by first determining the initial water content that is necessary to achieve the maximum reaction rate in the given solvent.

Keywords: enzymatic enantioselective esterification, non-conventional media, ionic liquid, racemic acid, effect of water content

1. Introduction

The history of the intentional use of enzymes as biocatalysts stretches back several decades. In recent years, intensified interest has been shown in applying enzymes in chemical reactions. Enzyme technology as an important discipline of biotechnology has begun to develop rapidly. Nowadays, it is of great importance in the pharmaceutical and pesticide industries where, in many cases, it has produced intermediates and active substances with enzymes or microorganisms more easily than by chemical synthesis and usually with a high degree of (enanti)selectivity [1–3].

The known advantages of these reactions are the mild reaction conditions, pure products, high yield and, in many cases, environmentally friendly by-products. At first, enzymes were only applied in aqueous media as they exert their catalytic activity under such conditions in various organisms. Later, the recognition that enzymes can exert their catalytic activity in organic solvents promoted intensive investigation among organic chemists who tested more and more enzymes from various classes as catalysts of organic chemical reactions [1, 4–7].

Contradictory results concerning how the activity and enantioselectivity of a lipase depend on the physical and chemical properties of the solvents can be found in the literature. In some cases, the different enzyme activities and

enantioselectivities observed in various organic solvents are not only affected by the solvents, e.g., when solvents with very different polarities are compared without fixing the water activity. In these experiments, the variation in the water activity probably contributes to the change in enzyme activity [6, 8–10].

In terms of the reaction, the water content of the reaction medium is twice as significant. To keep the enzyme activity and enantioselectivity of the lipase constant, a constant amount of water should be provided. As the content of the reaction medium changes as the conversion proceeds, the water adsorption capacity of the reaction medium does not remain constant during the reaction either. Water activity is an index which indicates how much water is accessible to the enzyme. Polar solvents can adsorb more water, while in non-polar solvents less water is required to achieve saturation and form a new aqueous phase where the water activity of the organic solvent is equal to one ($a_w = 1$). Therefore, two solvents of different polarities but equal water activities may contain significantly different amounts of water [11–13].

Based on the aforementioned considerations, in the literature a constant water activity is sought instead of a constant concentration of water during enzymatic reactions, e.g. by pervaporation of salt hydrates [14–16]. In reactions where water is not produced, the initial water activity of the reaction medium is fixed and the change in water activity, which is caused by changes in the polarity

*Correspondence: gubiczal@almos.uni-pannon.hu

of the reaction medium, is neglected. In the case of esterifications, where the water activity of the reaction medium significantly increases as the reaction proceeds, the water activity must be constantly controlled [16–19].

In this study, the resolution of (*R,S*)-2-bromopropanoic acid was analyzed. Changes in the activity and enantioselectivity of the enzyme *Candida rugosa lipase*, which is suitable when the water content of the reaction medium is changed during the aforementioned reaction, were investigated. Identification of the simplest method to sustain a constant water activity required for kinetic examinations was also sought.

2. Experimental

2.1 Samples and Measurements

All chemicals were commercially available and used without further purification.

Candida rugosa lipase (EC 3.1.1.3) (nominal activity: $920 \text{ U mg}_{\text{enzyme}}^{-1}$) was obtained from Sigma-Aldrich (St. Louis, USA). Racemic 2-bromopropanoic acid and the ionic liquids used, namely [BMIM]PF₆ (1-Butyl-3-methylimidazolium hexafluorophosphate), [NMIM]PF₆ (1-Methyl-3-nonylimidazolium hexafluorophosphate) and [BMIM]BF₄ (1-Butyl-3-methylimidazolium tetrafluoroborate), were obtained from Merck KGaA (Darmstadt, Germany). Butan-1-ol as well as all the other organic solvents and salts used were manufactured by Reanal Laboratory Chemicals Ltd. (Budapest, Hungary).

In a typical experiment, 2 mmol of racemic 2-bromopropanoic acid and 12 mmol of butan-1-ol were added to 5 ml of solvent. The water concentration of the reaction mixture was measured using a Mettler DL35 Karl Fischer titrator. The water activity was adjusted using salts of different a_w values (LiCl ($a_w = 0.11$), MgCl₂ ($a_w = 0.33$), NaBr ($a_w = 0.57$), KI ($a_w = 0.69$), KCl ($a_w = 0.84$) and K₂SO₄ ($a_w = 0.97$)). The reaction was started by adding 0.1 g of enzyme and the closed flasks were shaken in a New Brunswick G-24 horizontal shaker incubator.

2.2 Analysis

The (*R*)- and (*S*)-esters produced were analyzed by an HP 5890A GC (gas chromatograph) using a 25 m FS-LIPODEX E chiral capillary GC column from MACHEREY-NAGEL (Aachen, Germany). The samples from organic solvents were directly injected into the GC after being extracted from ionic liquids using n-hexane. The activity of the lipase was characterised by the amounts of (*R*)- and (*S*)-esters produced.

3. Results and Analysis

3.1 Experiments

To investigate the actual effect of solvents on the enzyme's activity, the same water activity should be pro-

vided in the reaction media to avoid differences in enzyme activity originating from variations in water activity. By choosing the most suitable method, the application of [BMIM]BF₄ must be considered, which is a polar solvent and miscible with water. The setting of the water activity with salt hydrate pairs and saturated salt solutions can be hindered as salts dissolve in ionic liquids [19]. As an alternative, the fact that the maximum enzyme activity of *Candida rugosa lipase* is achieved at the same water activity in any solvent was exploited [16]. According to the polarity of the solvents, the same water activity results in different water contents in various solvents, namely the reaction rate or conversion that indicate enzyme activity will be at their maxima with different water contents. An opportunity arises from the inversion of these considerations: the optimal initial water activity, required for kinetic examinations, can be set by determining the initial water content that provides the maximum reaction rate for each solvent.

Naturally, to precisely set a given water activity, the reaction rate should be measured by monitoring the water content infinite times. Instead of this, at least five different initial concentrations of water were set for each solvent. To calculate the reaction rates, the amounts of (*R*)- and (*S*)-2-Bromopropanoic acid butyl esters produced until 10% conversion was achieved or over two hours were considered. To determine the equilibrium constant necessary for calculating the enantiomeric ratio, quick reactions with (*R*)-2-bromopropanoic acid butyl ester were studied in organic solvents until the equilibrium concentration was reached. In contrast, with ionic liquids numerous reaction media had to be prepared as many samples were taken because for gas chromatography (*R*)- and (*S*)-2-bromopropanoic acid butyl esters had to be extracted from the ionic liquids using n-hexane and the subsequent extracts analysed. As a result, 15 reaction media were prepared simultaneously and the products extracted from them when samples were taken.

3.2 Effect of water content

The reaction rate altered as a function of water content according to optimum curves (Fig. 1). The highest reaction rate was obtained in n-hexane and the ionic liquid [BMIM]PF₆ when the concentrations of water were 0.15 mol dm^{-3} ($8.9 \times 10^{-3} \text{ mol h}^{-1} \text{ g}^{-1}$) and 0.38 mol dm^{-3} , respectively. The esterification reaction rate was very similar in toluene and [BMIM]PF₆ ($3.2 \times 10^{-3} \text{ mol h}^{-1} \text{ g}^{-1}$ and $3.0 \times 10^{-3} \text{ mol h}^{-1} \text{ g}^{-1}$, respectively), while in the more polar tetrahydrofuran, [BMIM]BF₄ esters were produced at a very low reaction rate ($10^{-3} \text{ mol h}^{-1} \text{ g}^{-1}$) which was observed to be only slightly dependent on the concentration of water.

The enantioselectivity of *Candida rugosa lipase* also varied as a function of water content according to optimum curves, however, was shown to be less dependent on the concentration of water than the reaction rate (Fig. 2).

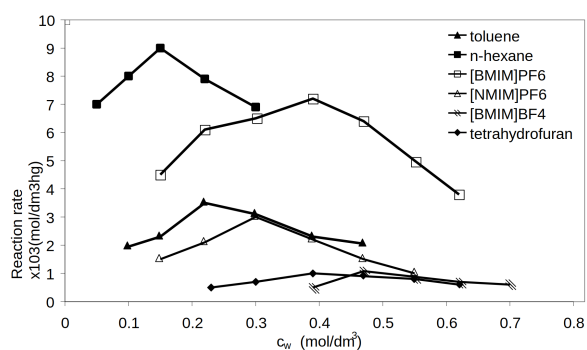


Figure 1: Dependence of the reaction rate on the initial concentration of water

The enantioselectivities in [NMIM]PF₆ and [BMIM]PF₆ were modest (25 and 19, respectively), while were significantly lower in the other solvents. The highest enantioselectivity ($E = 10$) was obtained in n-hexane among other classic organic solvents.

3.3 Discussion

In Table 1, the concentrations of water are summarized. It is shown that the maximum reaction rate ($c_w(\text{conv})$) or enantioselectivity (E) ($c_w(E)$) can be achieved at 30 °C after 2 hours. The enzyme activity and enantioselectivity of *Candida rugosa lipase* varied according to optimum curves that plots water activity, moreover, the maximum reaction rate and enantioselectivity can be obtained at the same water activity regardless of the solvent used. Based on these observations, it is probable that the water activity will be the same in reaction media if a suitable $c_w(\text{conv})$ concentration of water is set in every solvent. Similarly, the water activity of reaction media will be approximately the same by setting the suitable $c_w(E)$ concentration of water. It is possible to set approximately the same water activity in reaction media indirectly, even in the absence of salt pairs or salt hydrates.

However, it should be mentioned that the c_w values required to reach the maximum conversion or enantioselectivity are not necessarily the same. As can be observed in the case of the ionic liquid [BMIM]PF₆, a maximum conversion of 29.0% was achieved when $c_w(\text{conv}) = 0.38 \text{ mol dm}^{-3}$, while only a conversion of 26.2% was ob-

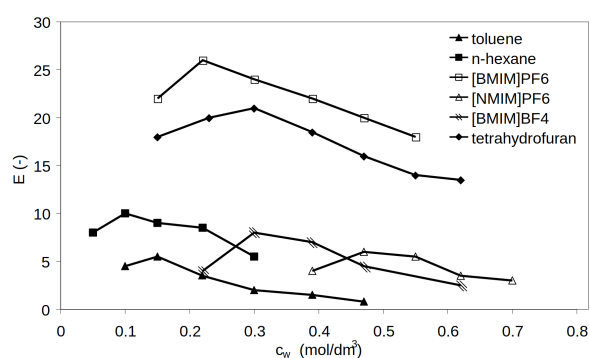


Figure 2: Dependence of the enantioselectivity on the initial concentration of water

tained when $c_w(E) = 0.31 \text{ mol dm}^{-3}$ required for the maximum enantioselectivity of just 20.0. Similar observations may be seen in the case of organic solvents, e.g. n-hexane in which a maximum conversion (36.1%) was achieved when $E = 8$, while maximum enantioselectivity ($E = 10$) resulted when the conversion was only 31.7%. Therefore, it must be decided whether reaching the maximum conversion or maximum enantioselectivity is the aim. The determination of the maximum conversion as a function of the required enantioselectivity will be the subject of future research.

4. Conclusion

In this study, it has been proven by the esterification of 2-bromopropanoic acid in the presence of *Candida rugosa lipase* that during reactions conducted in such non-conventional media, the determination of the optimal water content can be significantly simplified by setting the optimal concentration of water instead of the water activity, which is difficult to accomplish. For this purpose, the initial water content required to achieve the maximum reaction rate must be determined. As the water contents needed to achieve the maximum conversion or maximum enantioselectivity are usually different, further optimization tasks are necessary.

Acknowledgement

The financial support of Széchenyi 2020 under the project EFOP-3.6.1-16-2016-00015 is acknowledged.

Table 1: Conversion and enantioselectivity during the enantioselective esterification reaction at the optimum $c_w(\text{conv})$ and $c_w(E)$ values in different solvents ($T = 30 \text{ }^\circ\text{C}$, $t = 2 \text{ h}$).

Solvent	$\log P$	$c_w(\text{conv})$ mol dm ⁻³	Conversion %	E	$c_w(E)$ mol dm ⁻³	Conversion %	E
[BMIM]BF ₄	-2.44	0.54	4.6	5	0.46	4.0	6
[BMIM]PF ₆	-2.38	0.38	29.0	18	0.31	26.2	20
[NMIM]PF ₆	-2.19	0.31	13.4	24	0.23	8.9	25
Tetrahydrofuran	0.50	0.38	4.3	4	0.31	3.2	5
Toluene	2.50	0.23	13.9	3	0.15	10.1	5
n-Hexane	3.50	0.15	36.1	8	0.08	31.7	10

REFERENCES

- [1] Carrea, G.; Riva, S.: Organic synthesis with enzymes in non-aqueous media (Wiley-VCH Verlag GmbH & Co. KGaA, Weinheim, Germany) 2008, pp. 169–190 ISBN: 978-3-527-31846-9
- [2] Bommaris, A. S.; Riebel, B. R.: Biocatalysis (Wiley-VCH Verlag GmbH & Co. KGaA, Weinheim, Germany) 2004, pp. 339–372 DOI: 10.1002/3527602364.ch12
- [3] Gholivand, S.; Lasekan, O.; Tan, C. P.; Abas, F.; Wei, L. S.: Optimization of enzymatic esterification of dihydrocaffeic acid with hexanol in ionic liquid using response surface methodology, *Chem. Cent. J.*, 2017, **11**(44), 1–10 DOI: 10.1186/s13065-017-0276-2
- [4] Ghaffari-Moghaddam, M.; Eslahi, H.; Aydin, Y. A.; Saloglu, D.: Enzymatic processes in alternative reaction media: a mini review, *J. Biol. Met.*, 2015, **2**(3), 25–35 DOI: 10.14440/jbm.2015.60
- [5] Hobbs, H. R.; Thomas, N. R.: Biocatalysis in supercritical fluids, in fluorinated solvents, and under solvent-free conditions, *Chem. Rev.*, 2007, **107**(6), 2786–2820 DOI: 10.1021/cr0683820
- [6] Naushad, M.; AlOthman, Z. A.; Khan, A. B.; Ali, M.: Effect of ionic liquid on activity, stability, and structure of enzymes: A review, *Int. J. Biol. Macromol.*, 2012, **51**(4), 555–560 DOI: 10.1016/j.ijbiomac.2012.06.020
- [7] Ulbert, O.; Fráter, T.; Bélafi-Bakó, K.; Gubicza, L.: Enhanced enantioselectivity of *Candida rugosa* lipase in ionic liquids as compared to organic solvents, *J. Mol. Catal. B: Enzym.*, 2004, **31**(1–3), 39–45 DOI: 10.1016/j.molcatb.2004.07.003
- [8] Wu, B.-P.; Wen, Q.; Xu, H.; Yang, Z.: Insights into the impact of deep eutectic solvents on horseradish peroxidase: Activity, stability and structure, *J. Mol. Catal. B: Enzym.*, 2014, **101**, 101–107 DOI: 10.1016/j.molcatb.2014.01.001
- [9] Ghaffari-Moghaddam, M.; Ahmad, F. B. H.; Basri, M.; Abdul Rahman, M. B.: Lipase-catalyzed esterification of betulonic acid using phthalic anhydride in organic solvent media: Study of reaction parameters, *J. Appl. Sci.*, 2010, **10**(4), 337–342 DOI: 10.3923/jas.2010.337.342
- [10] Peres, C.; Gomes da Silva, M. D. R.; Barreiros, S.: Water activity effects on geranyl acetate synthesis catalyzed by Novozym in supercritical ethane and in supercritical carbon dioxide, *J. Agric. Food Chem.*, 2003, **51**(7), 1884–1888 DOI: 10.1021/jf026071u
- [11] Svensson, I.; Wehtje, E.; Adlercreutz, P.; Mattiasson, B.: Effects of water activity on reaction rates and equilibrium positions in enzymatic esterifications, *Biotechnol. Bioeng.*, 1994, **44**(5), 549–556 DOI: 10.1002/bit.260440502
- [12] Páez, B. C.; Medina, A. R.; Rubio, F. C.; Moreno, P. G.; Grima, E. M.: Modeling the effect of free water on enzyme activity in immobilized lipase-catalyzed reactions in organic solvents, *Enzyme Microb. Technol.*, 2003, **33**(6), 845–853 DOI: 10.1016/S0141-0229(03)00219-9
- [13] Kwon, C. H.; Lee, J. H.; Kim, S. W.; Kang, J. W.: Lipase-catalyzed Esterification of (S)-naprofen ethyl ester in supercritical carbon dioxide, *J. Microbiol. Biotechnol.*, 2009, **19**(12), 1596–1602 DOI: 10.4014/jmb.0905.05051
- [14] Gubicza, L.; Bélafi-Bakó, K.; Fehér, E.; Fráter, T.: Waste-free process for continuous flow enzymatic esterification using a double pervaporation system, *Green Chem.*, 2008, **10**(12), 1284–1287 DOI: 10.1039/B810009H
- [15] Benedict, D. J.; Parulekar, S. J.; Tsai, S.-P.: Pervaporation-assisted esterification of lactic and succinic acids with downstream ester recovery, *J. Membr. Sci.*, 2006, **281**(1–2), 435–445 DOI: 10.1016/j.memsci.2006.04.012
- [16] Fontes, N.; Harper, N.; Halling, P. J.; Barreiros, S.: Salt hydrates for in situ water control have acid-base effects on enzymes in nonaqueous media, *Biotechnol. Bioeng.*, 2003, **82**(7), 802–808 DOI: 10.1002/bit.10627
- [17] Márkus, Zs.; Bélafi-Bakó, K.; Tóth, G.; Nemestóthy, N.; Gubicza, L.: Effect of chain length and order of the alcohol on enzyme activity during enzymatic esterification in organic media, *Hung. J. Ind. Chem.*, 2017, **45**(2), 35–39 DOI: 10.1515/hjic-2017-0018
- [18] Robb, D. A.; Yang, Z.; Halling, P. J.: The use of salt hydrates as water buffers to control enzyme activity in organic solvents, *Biocatalysis*, 2009, **9**(1–4), 277–283 DOI: 10.3109/10242429408992127
- [19] Eckstein, M.; Wasserscheid, P.; Kragl, U.: Enhanced enantioselectivity of lipase from *Pseudomonas* sp. at high temperatures and fixed water activity in the ionic liquid, 1-butyl-3-methylimidazolium bis[(trifluoromethyl)sulfonyl]amide, *Biotechnol. Lett.*, 2002, **24**(10), 763–767 DOI: 10.1023/A:1015563801977

FOLLOW-UP CONTROL OF A SECOND ORDER SYSTEM IN SLIDING MODE

MÁRK DOMONKOS ^{*1} AND NÁNDOR FINK¹

¹Department of Mechatronics, Optics and Mechanical Engineering Informatics, Budapest University of Technology and Economics, Bertalan Lajos u. 4-6, Budapest, 1111, HUNGARY

This paper deals with an instantaneous feedback controlled inverter using sliding mode control. The theoretical contribution of this paper is that a common state-space-based sliding surface design method is extended for follow-up control. Starting from the basic theory of sliding mode control, the trajectory of the error signal is modelled. The practical contribution of this paper is the relationship between the trajectory of the error signal and the Total Harmonic Distortion (THD) of the output voltage signal. The conditions of the sliding mode control using an Uninterruptible Power Supply (UPS) are discussed. A rectifier as a non-linear load is simulated. Experimentally validated simulation results are presented.

Keywords: sliding mode control, hysteresis control, second order system, UPS

1. Introduction

Power electronics equipment that produces alternating voltage and current impulses is typical of Variable Structure Systems (VSSs). A VSS usually consists of a state when it is insensitive to variations in parameters and load disturbances. This state is referred to as the sliding mode. The cost of insensitivity is an infinitely high switching frequency. Due to the limits with regard to switching delays and frequencies of controlled switches, an ideal sliding mode does not exist. However, the ideal sliding mode can be approximated with an acceptable degree of accuracy.

The theory of Variable Structure Systems and sliding mode control was developed decades ago in the Soviet Union, mainly by Vadim I. Utkin [1] and David K. Young [2]. According to the theory, sliding mode control should be robust but experiments have shown that it is subject to serious limitations. The main problem with applying the sliding mode is the high frequency of oscillation around the sliding surface, referred to as chattering, which strongly reduces the performance of the control. Very few have managed to put the robust behavior predicted by the theory into practice. Many have concluded that the presence of chattering makes the sliding mode control a good game theory, which is not applicable in practice. Over the following period, researchers invested most of their energy in chattering-free applications, leading to the development of numerous solutions like the discrete-time sliding mode [3], sector sliding mode [4], adaptive sliding mode [5] and terminal sliding mode [6].

Sliding modes can also be used for feedback compensation [7].

The design of a sliding mode controller consists of three main steps. The first is the design of the sliding surface, the second step is the design of the control law which holds the system trajectory on the sliding surface, and the third and key step is implementation of the chattering-free sliding mode control. The systematic sliding manifold design for linear systems was proposed by Utkin [1]. This method was extended in several ways and optimal sliding manifold designS proposed, e.g. frequency-shaped sliding mode control (FSSMC) [8] surface design based on H^∞ control theory [9, 10] and Tensor Product Model Transformation-based Sliding Surface Design [11]. The reference signal was constant in all the aforementioned papers. Recently, the application of predictive control has become popular [12]. The new element in this paper is that the original method was extended for Follow-up Control.

According to Refs. [13] and [14], Uninterruptible Power Supplies (UPSs) are being broadly adopted for the protection of sensitive loads, e.g. PCs, air traffic control systems, life care medical equipment, etc., against line failures or other perturbations in AC mains. Ideally, an UPS should be able to deliver: 1) a sinusoidal output voltage with low total harmonic distortion during normal operation, even when feeding nonlinear loads (particularly rectified loads); 2) the voltage dip and recovery time due to a change in load step must be kept as small as possible, that is, provide a fast dynamic response; 3) the steady-state error between the sinusoidal reference and load regulation must be zero. To achieve these, a Proportional In-

*Author for correspondence: domonkos@mogi.bme.hu

tegral (PI) controller is usually used [15], moreover, issues concerning robust stability and controller robustness are discussed in [16]. However, the system using the PI controller subject to a variable load rather than the nominal ones cannot produce a fast and stable output voltage response. In the literature, some hybrid solutions to overcome this problem can be found [17, 18]. The principle of Pulse Width Modulation (PWM) plays a very important role in power electronics [19]. In the field of inverter technology, which produces a sinusoidal voltage, a great number of "optimized PWM" techniques have been proposed in the literature. These types of PWM inverters have very good steady-state characteristics, but for the voltage regulator to respond to a sudden change in the load takes a few cycles and nonlinear loads can cause high "load harmonics". This is unacceptable in UPS applications for which instantaneous feedback is preferred [20, 21]. The sliding mode control of power electronic inverters is suggested in Refs. [22] and [23]. On the one hand the main advantage of the sliding mode-based method proposed in this paper is the direct control of the transistor switches, but on the other hand uncontrolled THD results. That is why the THD is the focus of this paper.

The structure of this paper is as follows. After the Introduction, Section 2 presents the problem statement, describes the system configuration and summarizes the design of the sliding mode control. Section 3 describes the equations of the system and shows how the mathematical foundations are applied to a practical example. Following the main steps of sliding mode design, namely the surface design, a control law is selected by taking into consideration the reduced chattering. Section 4 presents the simulation results, which are validated by experimental measurements of a 10 kVA UPS. Finally, in Section 5, the presented results are analyzed.

2. Problem Statement

2.1 System Configuration

A simplified diagram of the inverter and filter is shown in Fig. 1 V_b denotes the battery voltage and v_i stands for the input voltage of the system, which is a filter with a load. The input signal consists of three different values (V_b , $-V_b$ and 0) depending on the switching states of the transistors. The goal is that the transistors must be switched in such a way that v_o , the output voltage of the system, follows the sinusoidal reference signal. L_s in Fig.1 denotes the leakage inductance of the transformer, which has a special structure to increase and set the value of L_s . The main field inductance L_p cannot be ignored from the point of view of the resonance circuit. The loss of the transformer is modelled by an increased load.

$$v_o(t) = \sqrt{2} \cdot 230 \cos(2\pi 50t) \quad (1)$$

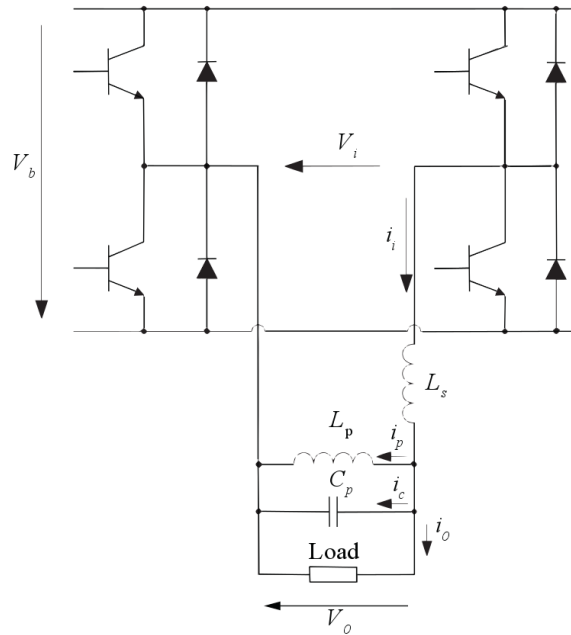


Figure 1: Simplified figure of the inverter and filter

2.2 Sliding Mode Control

A Single-Input Single-Output (SISO) system is given in state-space controllable canonical form.

$$\dot{\mathbf{x}}(t) = \mathbf{A}\mathbf{x}(t) + \mathbf{b}u(t) \quad (2)$$

$$y(t) = \mathbf{c}\mathbf{x}(t) \quad (3)$$

where $\mathbf{x}(t) \in \mathbb{R}^n$, $\mathbf{A} \in \mathbb{R}^{n \times n}$, $\mathbf{b} \in \mathbb{R}^{n \times 1}$, $\mathbf{c} \in \mathbb{R}^{1 \times n}$ and $u(t), y(t) \in \mathbb{R}$. $y(t)$, the output variable of the controlled plant, can be described by a n -th order differential equation supposing that the reference signal $y_r(t)$ can be differentiated at least n times.

The goal is given in

$$y_r(t) = y(t) \text{ if } t > T_c \quad (4)$$

where T_c denotes the control period. The system error, $e_y(t)$, is given by

$$e_y(t) = y_r(t) - y(t) \quad (5)$$

Thus the error signal, $e_y(t)$, can also be differentiated at least n times, so the $n - 1$ -th derivative must exist and is continuous. Due to the latter property, when trying to eliminate the error, it is also useful to control its derivatives (including the $n - 1$ -th derivative). Otherwise, because of the system inertia, an oscillation with a large amplitude could arise. The essence of sliding mode control could be summarized as follows: in order to eliminate the error in the n -th dimensional phase space, a continuous error trajectory running into the origin has been designed. Whilst planning, the physical limits should be taken into account. By implementing our very own transient, the ideal system follows the reference signal without any errors. The control signal is designed so that the

trajectory realized does not deviate from the prescribed one or once the origin has been reached, it remains at rest.

Usually σ , a scalar variable, can be defined as a positive or negative distance between the desired and actual trajectories, or each trajectory sector can be prescribed by a single scalar variable. The task of the controller is to ensure this scalar variable remains zero. In the classical method of sliding mode control, this scalar variable is calculated as a linear combination of the error and its derivatives [1]. When $n = 2$, the scalar variable can be defined by the following equation:

$$\sigma(t) = e_y(t) + \tau \dot{e}_y(t) \quad (6)$$

where τ denotes a time constant-type control parameter chosen by us. In sliding mode control:

$$\sigma = 0 \quad (7)$$

and the trajectory is described by the following equation:

$$e_y(t) = -\tau \dot{e}_y(t) \quad (8)$$

that corresponds to a $-1/\tau$ gradient in the phase plane. This is usually referred to as the sliding line or sliding surface in multidimensional phase space. The solution of Eq. 8 is an exponential function with a negative exponent:

$$e_y(t) = E_0 e^{-\frac{t}{\tau}} \quad t \geq 0 \quad (9)$$

where $E_0 = e_y(0)$. Consequently, the error will decrease according to the chosen time constant, τ , independently from the system parameters, e.g. load. After an exponential transient process, $y_r(t) = y(t)$. To ensure that the system moves in all cases towards the sliding mode (i.e. towards $\sigma(t) = 0$), the following condition is necessary:

$$\sigma(t)\dot{\sigma}(t) \leq 0 \quad (10)$$

The design of a sliding mode controller does not require accurate modelling, it is sufficient to only know the boundaries of the model parameters and the disturbance. During sliding mode control, the only task is to switch the control signal so that Eq. 10 is valid in every instance. No other information concerning the controlled plant and the disturbances is needed. It is sufficient to determine whether Eq. 10 holds or not. In simple cases (or within a range of errors and its derivatives), the signs of the control signal and $\dot{\sigma}(t)$ are opposite. Thus it is often satisfactory to use a relay controller, which switches the control signal according to the sign of the parameter $\sigma(t)$.

2.3 Follow-up Control

Since $y_r(t)$ is not constant, $W_{y_r,u}(s)$, the transfer function from $u(t)$ ($v_i(t)$) to $y_r(t)$ ($v_o(t)$), must be calculated. According to Eq. 4, it is the inverse of the transfer function with regard to the inverted system:

$$y(s) = W_{u,y}(s)u(s) \quad (11)$$

$$W_{y_r,u}(s) = W_{u,y}^{-1}(s) \quad (12)$$

Usually, the inverse of $W_{u,y}(s)$ cannot be realized. In our case, $y_r(t)$ is sinusoidal:

$$y_r(t) = \sqrt{2}V_r \cos(\omega_r t) \quad (13)$$

Only two parameters must be calculated, namely the gain (G_r) and phase shift (φ_r) of the transfer function of the system at the reference angular frequency (ω_r). The definition of the error (Eq. 5) must be modified:

$$e_y(t) = \frac{\sqrt{2}}{G_r} V_r \cos(\omega_r t - \varphi_r) - y(t) \quad (14)$$

3. Equations of the System

3.1 Filter and Load

Using the notation of Fig. 1, the equation for the currents is:

$$i_i(t) = i_o(t) + i_p(t) + i_c(t) \quad (15)$$

By assuming resistive load R_L :

$$i_o(t) = \frac{1}{R_L} v_o(t) \quad (16)$$

The equation of the input voltage is

$$v_i(t) = L_s \frac{di_i(t)}{dt} + v_o(t) \quad (17)$$

By substituting Eqs. 15 and 16 into Eq. 17, the filter circuit with a resistive load can be described by the following differential equation:

$$v_i(t) = L_s C_p \ddot{v}_o(t) + \frac{L_s}{R_L} \dot{v}_o(t) + \frac{1}{G} v_o(t) \quad (18)$$

where

$$G = \frac{L_p}{L_s + L_p} \quad (19)$$

The transfer function from $u(t)$ ($v_i(t)$) to $y_r(t)$ ($v_o(t)$) (including the effect of the resistive load) can be calculated from the Laplace transformed form of Eq. 18:

$$v_o(s) = \frac{G}{GL_s C_p s^2 + \frac{GL_s}{R_L} s + 1} v_i(s) = W(s) v_i(s) \quad (20)$$

3.2 The states of the state-space equation

Since the inverter and load are handled separately, the system has two inputs, namely u_i and i_o . Since the input current must be calculated, three state variables are selected for the three storage elements, even if they are not independent and the rank of the system matrix is only 2. Using the notation of Fig. 1, the three state variables are $i_i(t)$, $i_p(t)$ and $v_c(t)$:

$$\mathbf{x}(t) = \begin{bmatrix} i_i(t) \\ i_p(t) \\ v_c(t) \end{bmatrix} \quad (21)$$

The load is connected in parallel to the inverter capacitor C_p . The load current includes the effect of transformer losses. The system has three outputs since $v_o(t) = v_c(t)$ as well as its derivative are necessary to calculate the scalar variable and $\dot{i}_i(t)$ is visualised. In the real system, the current of the capacitor is measured instead of $\dot{v}_o(t)$. According to Eqs. 15, 16, and 17, the matrices of the system are:

$$\begin{aligned} \mathbf{A} &= \begin{bmatrix} 0 & 0 & -\frac{1}{L_s} \\ 0 & 0 & \frac{1}{L_p} \\ \frac{1}{C_p} & -\frac{1}{C_p} & 0 \end{bmatrix} & \mathbf{B} &= \begin{bmatrix} 0 & -\frac{1}{L_s} \\ 0 & 0 \\ -\frac{1}{C_p} & 0 \end{bmatrix} \\ \mathbf{C} &= \begin{bmatrix} 1 & 0 & 0 \\ 0 & 1 & 0 \\ 0 & 0 & 1 \end{bmatrix} & \mathbf{D} &= \begin{bmatrix} 0 & 0 \\ 0 & 0 \\ 0 & 0 \end{bmatrix} \end{aligned} \quad (22)$$

3.3 Error Trajectory

To calculate the error defined by Eq. 14, G_r and φ_r must first be calculated. According to Eq. 20:

$$W(j\omega_r) = \frac{G}{GL_s C_p (j\omega_r)^2 + \frac{GL_s}{RL} j\omega_r + 1} \quad (23)$$

G_r and φ_r can be calculated from Eq. 23, where $W(j\omega_r)$ denotes a simple complex number:

$$G_r = |W(j\omega_r)| \quad (24)$$

$$\varphi_r = \text{angle}(W(j\omega_r)) \quad (25)$$

Since the filter must be inductive, φ_r must be negative. Therefore, the reference signal must lead to $v_o(t)$, which is the controlled signal in Eq. 14:

$$y(t) = v_o(t) \quad (26)$$

The derivative of the error is:

$$\dot{e}_y(t) = -\omega_r \frac{\sqrt{2}}{G_r} V_r \sin(\omega_r t - \varphi_r) - \dot{v}_o(t) \quad (27)$$

The scalar variable of the sliding mode control is calculated by Eq. 6.

3.4 Control Law

Three different control laws were examined. All of them can directly control the switching of the transistors. This is the main advantage of sliding mode control in the field of power electronics. More advanced controllers can be found in Ref. [24].

Simple Relay

The input voltage on the filter is switched according to the sign of $\sigma(t)$:

$$v_i(t) = V_b \text{sign}(\sigma(t)) \quad (28)$$

From a practical point of view, the main problems of Eq. 28 are

- the inverter has a zero state, which is not applied;
- the switching frequency is uncontrolled.

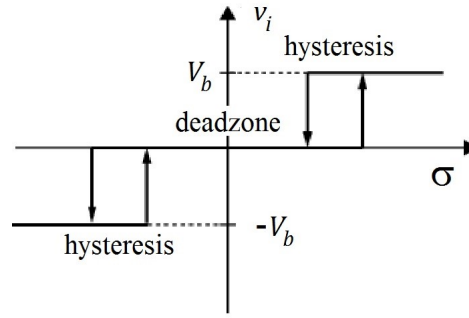


Figure 2: Double Relay with dead zone and hysteresis

Double Relay

The solution to the first problem is the usage of two relays:

$$v_i(t) = \frac{V_b}{2} \text{sign}(\sigma(t)) + \frac{V_b}{2} \text{sign}(\cos(\omega_r t - \varphi_r)) \quad (29)$$

V_b and 0 are switched in the positive half period, while $-V_b$ and 0 are switched in the negative half period. However, Eq. 29 does not solve the second problem.

Double Relay with dead zone and hysteresis

Both problems can be solved by a double relay with dead zone and hysteresis. This control law is shown in Fig. 2.

3.5 Stability Analysis

Using a simple relay controller, whether or not Eq. 10 holds can be verified. First, $\dot{\sigma}(t)$ must be expressed:

$$\dot{\sigma}(t) = \dot{e}_y(t) + \tau \ddot{e}_y(t) \quad (30)$$

According to Eq. 27:

$$\ddot{e}_y(t) = -\omega_r^2 \frac{\sqrt{2}}{G_r} V_r \cos(\omega_r t - \varphi_r) - \ddot{v}_o(t) \quad (31)$$

$\ddot{v}_o(t)$ can be expressed from Eq. 18:

$$\ddot{v}_o(t) = \frac{1}{L_s C_p} v_i(t) - \frac{1}{R_L C_p} \dot{v}_o(t) - \frac{1}{GL_s C_p} v_o(t) \quad (32)$$

By substituting Eq. 28 into Eq. 32:

$$\ddot{v}_o(t) = \frac{V_b \text{sign}(\sigma(t))}{L_s C_p} - \frac{\dot{v}_o(t)}{R_L C_p} - \frac{v_o(t)}{GL_s C_p} \quad (33)$$

According to Eqs. 30 and 31, if the value of $\ddot{v}_o(t)$ is sufficiently large and the system operates in an area which is close enough to the sliding mode, then the sign of $\ddot{v}_o(t)$ is the opposite to that of $\dot{\sigma}(t)$. From Eq. 33, it is clear that if the value of V_b is sufficiently large and the system operates in an area which is close enough to the sliding mode, then the sign of $\ddot{v}_o(t)$ is the same as that of $\sigma(t)$. In conclusion, if the value of V_b is sufficiently large and the

system operates in an area which is close enough to the sliding mode, then the sign of $\sigma(t)$ is the opposite to that of $\dot{\sigma}(t)$. Similar analyses can be conducted for all control laws. In practice, the simulations proved that by substituting the actual parameters of the system, all the control laws examined fulfil the condition (Eq. 10) during normal operations.

4. Simulation

MATLAB-Simulink simulations were carried out.

4.1 MATLAB-Simulink model

The main elements of the MATLAB-Simulink model are shown in Figs. 3–6. Even if the structure of the controller shown in Fig. 6 is quite simple, its performance is quite robust.

4.2 Model validation

The simulation results were compared to previous results measured by [25] as shown in Fig. 7. The nominal power of the inverter is 10 VA. All parameters of (14) and (22) in addition to the values of dead zone and hysteresis shown in Fig. 2 are known from Ref. [25].

Like in real systems, where σ is tuned manually to set the number of switches per period, σ is changed to achieve a similar result in the simulation as in real systems. The simulation result is shown in Fig. 8 after the value of σ was set.

The first problem faced in the simulation was the steady state. When the real system was measured, the screen of the oscilloscope seemed to be frozen for most settings of σ . Therefore, the error trajectory was a closed curve during a period in a steady state.

Using the default settings of Simulink, a quasi-steady-state period of the error trajectory of the simulation resulted as is shown in Fig. 9. The consequent periods are slightly different, which causes subharmonics that are crucial from a practical point of view.

The main question is whether these subharmonics are an immanent property of the applied switching method or a result of an insufficiently precise simulation. Several simulations were carried out using different model configuration parameters in Simulink. It is concluded that the precise calculation of the switching instant is key to simulating proper steady states. The Ode113(Adam) method is the most suitable integral method for switched systems. (The equation solvers for UPS are compared in Ref. [26]).

4.3 Analysis of the simulation results

The main advantage of the PWM technique is that the filter can be smaller resulting in a smaller no-load current. The parameters of the filter are given in

$$L_s = 3.5\text{mH}, L_p = 32\text{mH}, C_p = 320\mu\text{F} \quad (34)$$

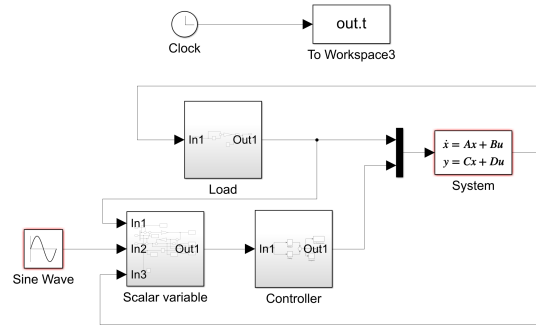


Figure 3: The whole system.

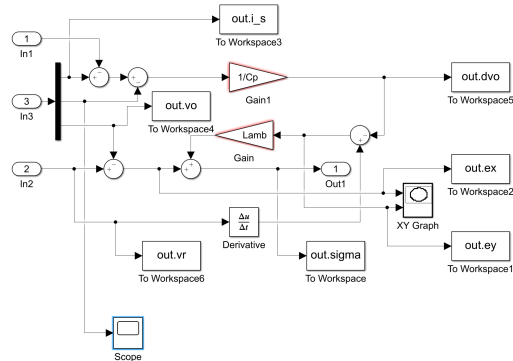


Figure 4: Subsystem for calculating scalar variable S.

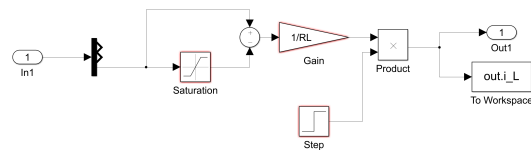


Figure 5: Subsystem for the load.

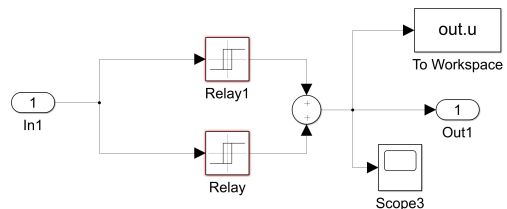


Figure 6: Subsystem for the relay controller of the dead zone and hysteresis

τ , the gradient of the switching line in the sliding mode, has been changed. The value of the nominal load is $R_L = 5.3\Omega$. The relationship between the gradient of the switching line and the number of switches is shown in Fig. 10. The larger the value of τ , the smaller the gradient of the switching line and the greater the number of switches per period. On the other hand, the bigger the value of τ , the longer the transient according to Eq. 9. The optimum must be calculated.

The number of switches per period and the total harmonic distortion (THD) are shown in Fig. 11 as a function of τ . The first ONE is staggered. The larger the num-

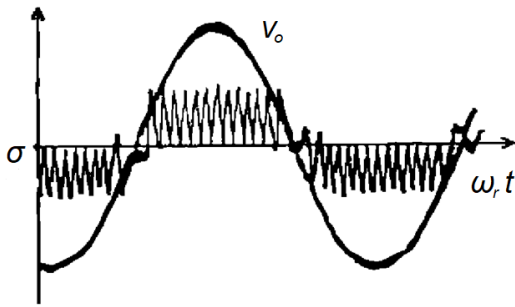


Figure 7: Reference measurement result

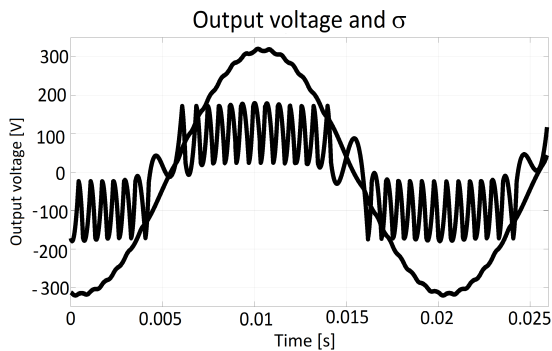


Figure 8: Reference simulation result

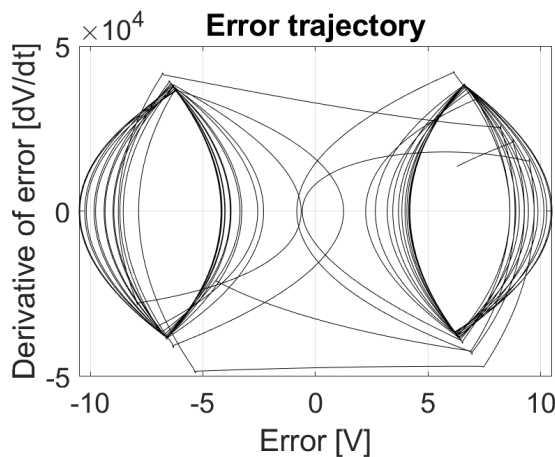


Figure 9: Error trajectory during a quasi-steady-state period

ber of switches is, the greater the switching loss and the smaller the THD are. The optimum is approximately 52 switches, therefore, 13 pulses per period, as is shown in Fig. 7 and Fig. 8. The step concerning the optimal number of switches is magnified in Fig. 12.

A local minimum of THD is located at the middle of a staircase (in Fig. 12) when the transient between the positive and negative half periods is smooth as is shown in Fig. 13.

By increasing τ , the transients change slightly. First, a V shape appears (see Fig. 14).

By further increasing τ , the V shape transforms into a loop (see Fig. 15) and the last pulses in all half periods have the opposite signs when compared to the reference signal (see Fig. 16) which increases the THD. Finally, the number of switches per period is increased by 4 and the

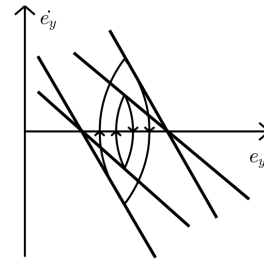


Figure 10: The effect of τ on the number of switches

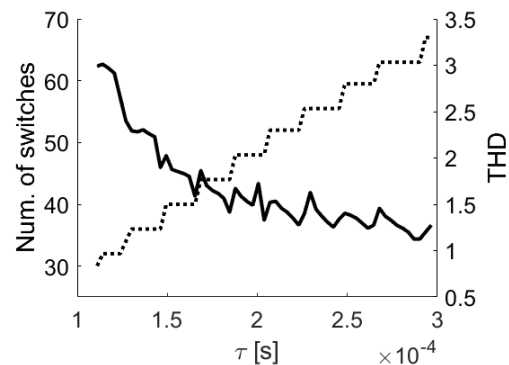


Figure 11: Number of switches and THD as a function of the gradient of the switching line

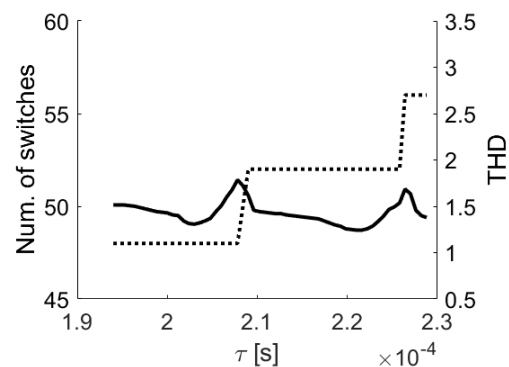


Figure 12: The optimal number of switches and its THD

transients are in the form of Vs and loops once more (see Fig. 17), which disappear at the middle of the staircase.

4.4 Non-linear load

The most challenging load is the rectifier [27], since its current is not sinusoidal and the value of its peak is relatively large. A rectifier resembling a load is simulated, which has approximately the same root mean square (RMS) value of the current as that of the nominal current. The time functions of the output voltage and current in addition to the input current are shown in Fig. 18. The RMS value of the input no-load current is zero at the beginning of the period, when the output current is zero. Since the load current is continuous and the reaction of the sliding mode controller is practically instantaneous as a result, this type of non-linear load has no significant ef-

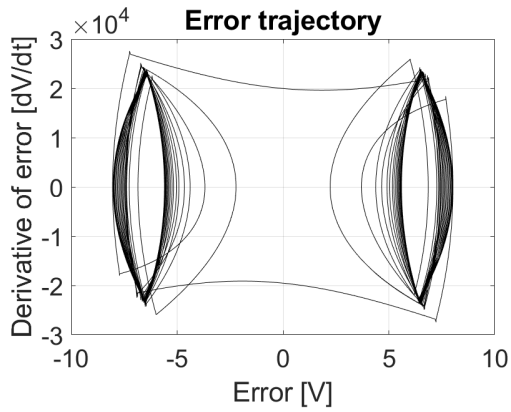


Figure 13: Smooth transient of error trajectory

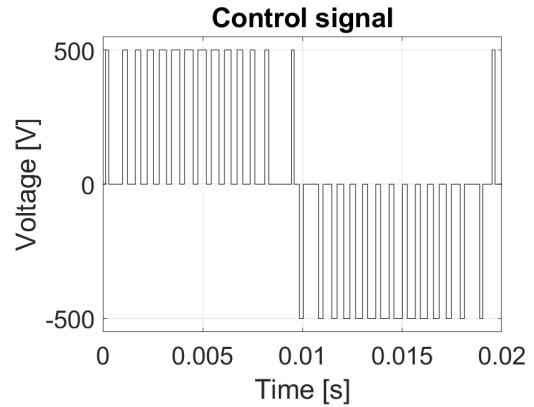


Figure 16: Control signal

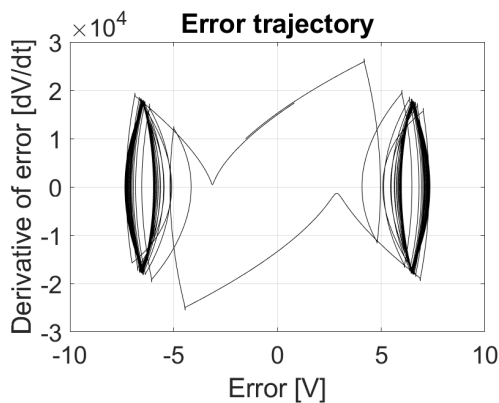


Figure 14: V-shaped transient of error trajectory

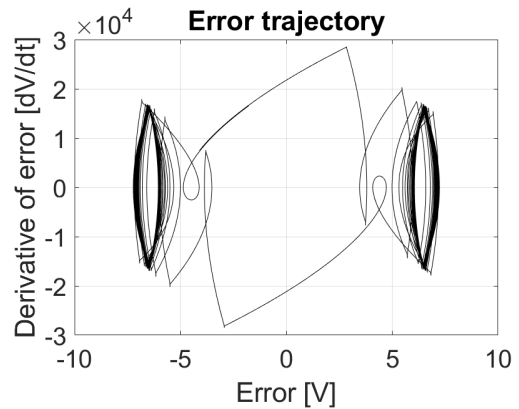


Figure 17: Transient of error trajectory after the number of switches is increased

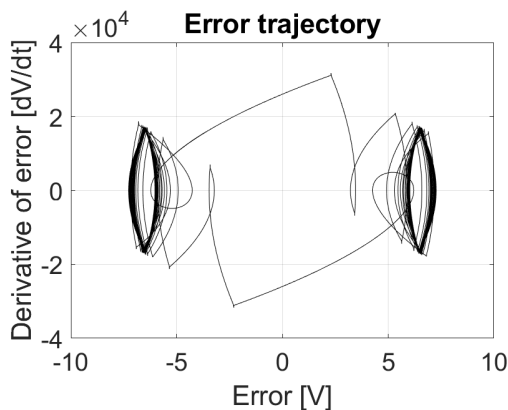


Figure 15: Loop-shaped transient of error trajectory

fect on the output voltage - the THD depends on the shape of the error trajectory, which is shown in Fig. 19:

4.5 Switching on the load

A nominal resistive load is assumed and the load is switched on at the peak value of the output voltage. The time functions of the voltage and current are shown in Fig. 20. Since the current is discontinuous, a transient is

present, which is recognizable in terms of the shape of the error trajectory in Fig. 21. The length of the transient depends on the value of τ , that is, 0.22 ms. The transient caused by any step change in the load occurs extremely quickly and only lasts approximately 1 ms.

5. Conclusions

This paper introduced a follow-up control method with a sinusoidal reference signal for the design of a sliding surface and the performance of a Double Relay controller with a dead zone and hysteresis operating in a sliding mode was analysed. The simulation of variable structure systems is very sensitive to the integral method of simulation. The zero-crossing must be detected. Even a relatively simple controller, which can be implemented by an analogue operational amplifier, also performs very well with a non-linear load. The positive and negative half periods can be separated by a dead zone and the switching frequency limited by hysteresis. The actual number of switches can be set by the gradient of the sliding line. The value of the THD depends on the shape of the error phase trajectory. A non-linear load with a continuous output current has no significant effect on the output voltage because of the instantaneous behavior of the sliding mode controller.

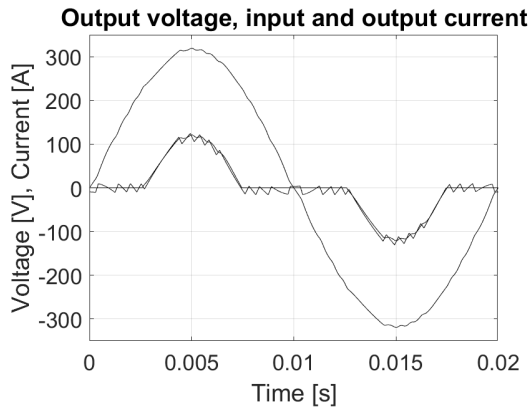


Figure 18: Output voltage as well as input and output currents with a rectifier-like load

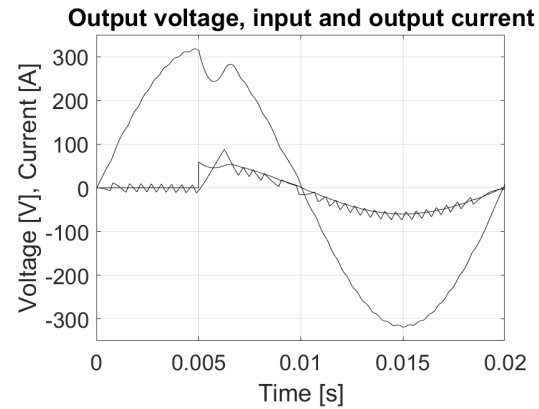


Figure 20: Output voltage as well as input and output currents after switching on the resistive load

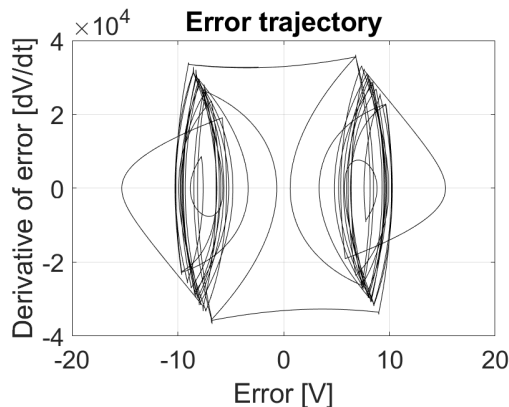


Figure 19: Error trajectory of the non-linear rectifier-like load

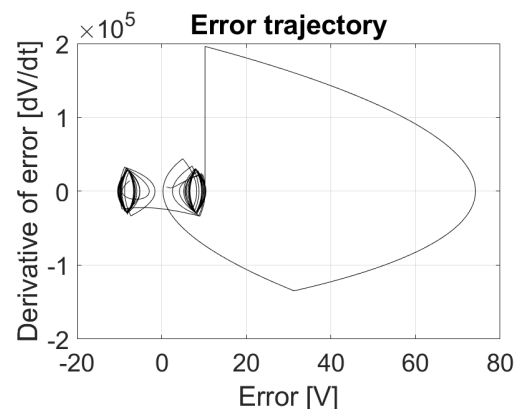


Figure 21: Error trajectory after switching on the resistive load

Acknowledgement

The research reported in this paper and carried out at the Budapest University of Technology and Economics has been supported by the National Research Development and Innovation Fund (TKP2020 Institution Excellence Subprogram, Grant No. BME-IE-MIFM) based on the charter of bolster issued by the National Research Development and Innovation Office under the auspices of the Ministry for Innovation and Technology.

REFERENCES

- [1] Utkin, V. I.: Variable structure control optimization (Springer-Verlag), 1992 DOI: [10.1007/978-3-642-84379-2](https://doi.org/10.1007/978-3-642-84379-2)
- [2] Young, K.: Controller design for manipulator using theory of variable structure systems, *IEEE Trans. Syst. Man Cybern. Syst.*, 1978, **8**(2), 101–109 DOI: [10.1109/TSMC.1978.4309907](https://doi.org/10.1109/TSMC.1978.4309907)
- [3] Korondi, P.; Hashimoto, H.; Utkin, V.: Discrete sliding mode control of two mass system, in: Proceedings of the 1995 IEEE International Symposium on Industrial Electronics, ISIE'95 (Piscataway (NJ), USA), 338–343 DOI: [10.1109/ISIE.1995.497019](https://doi.org/10.1109/ISIE.1995.497019)
- [4] Korondi, P.; Xu, J.; Hashimoto, H.: Sector sliding mode controller for motion control, in: Proceedings of the 8th international power electronics & motion control conference (PEMC, Prague, Czech), 254–259
- [5] Yu, H.; Ozguner, U.: Adaptive seeking sliding mode control, in IEEE American Control Conference (Minneapolis, USA), 2006 DOI: [10.1109/ACC.2006.1657462](https://doi.org/10.1109/ACC.2006.1657462)
- [6] Chang, E.-C.; Chang, F.-J.; Liang, T.-J.; Chen, J.-F.: DSP-based implementation of terminal sliding mode control with grey prediction for UPS inverters, *the 5th IEEE Conference on Industrial Electronics and Applications (ICIEA)*, 2010, 1046–1051 DOI: [10.1109/ICIEA.2010.5515790](https://doi.org/10.1109/ICIEA.2010.5515790)
- [7] Fink, N.: Model reference adaptive control for telemanipulation, *Hung. J. Ind. Chem.*, 2019, **47**(1), 41–48 DOI: [10.33927/hjic-2019-07](https://doi.org/10.33927/hjic-2019-07)
- [8] Young, K.; Özgüner, U.: Frequency shaped sliding mode synthesis, in International Workshop on VSS and Their Applications (Sarajevo)
- [9] Fodor, D.; Tóth, R.: Speed sensorless linear parameter variant H^∞ control of the induction motor, in Proceedings of the 43rd IEEE Conference Decision

- and Control (IEEE, Piscataway, USA), 4435–4440 DOI: [10.1109/CDC.2004.1429449](https://doi.org/10.1109/CDC.2004.1429449)
- [10] Hashimoto, H.; Konno, Y.: Sliding surface design in the frequency domain, in: Variable structure and Lyapunov control, 75–86 (Springer-Verlag), 1993 DOI: [10.1007/BFb0033679](https://doi.org/10.1007/BFb0033679)
- [11] Korondi, P.: Tensor product model transformation-based sliding surface design, *Acta Polytech. Hung.*, 2006, **3**(4), 23–36
- [12] Neukirchner, L. R.; Magyar, A.; Fodor, A.; Kutasi, N.D.; Kelemen, A.: Constrained predictive control of three-phase buck rectifiers, *Acta Polytech. Hung.*, 2020, **17**(1), 41–60 DOI: [10.12700/APH.17.1.2020.1.3](https://doi.org/10.12700/APH.17.1.2020.1.3)
- [13] Tai, T.-L.; Chen, J.-S.: UPS Inverter design using discrete-time sliding-mode control scheme, *IEEE Trans. Ind. Electron.*, 2002, **49**(1), 67–75 DOI: [10.1109/41.982250](https://doi.org/10.1109/41.982250)
- [14] Fedak, V.; Bauer, P.; Hájek, V.; Weiss, H.; Davat, B.; Manias, S.; Nagy, I.; Korondi, P.; Miksiewicz, R.; Duijsen, P.; Smékal, P.: Interactive E-learning in electrical engineering, in: 15th International Conference on Electrical Drives and Power Electronics (EDPE) (Podbanské), 368–373
- [15] Caceres, R.; Rojas, R.; Camacho, O.: Robust PID control of a buck-boost DC-AC converter, *Proc. IEEE INTELEC'02*, 2000, 180–185 DOI: [10.1109/intlec.2000.884248](https://doi.org/10.1109/intlec.2000.884248)
- [16] Precup, R.-E.; Preitl, S.: PI and PID controllers tuning for integral-type servo systems to ensure robust stability and controller robustness, *Electr. Eng.*, 2006, **88**(2), 149–156 DOI: [10.1007/s00202-004-0269-8](https://doi.org/10.1007/s00202-004-0269-8)
- [17] Al-Hosani, K.; Malinin, A.; Utkin, V. I.: Sliding mode PID control of buck converters, *European Control Conference*, 2009 DOI: [10.23919/ecc.2009.7074821](https://doi.org/10.23919/ecc.2009.7074821)
- [18] Li, H.; Ye, X.: Sliding-mode PID control of DC-DC converter, *5th IEEE Conference on Industrial Electronics and Applications (ICIEA)*, 2010, 730–734 DOI: [10.1109/ICIEA.2010.5516952](https://doi.org/10.1109/ICIEA.2010.5516952)
- [19] Holtz, J.: Pulsewidth modulation - A Survey, *IEEE Trans. Ind. Electron.*, 1992, **39**(5), 410–420 DOI: [10.1109/41.161472](https://doi.org/10.1109/41.161472)
- [20] Kawamura, A.; Hoft, R.: Instantaneous feedback controlled PWM inverter with adaptive hysteresis, *IEEE Trans. Ind. Appl.*, 1984, **20**(4), 769–775 DOI: [10.1109/TIA.1984.4504486](https://doi.org/10.1109/TIA.1984.4504486)
- [21] Aamir, M.; Kalwar, K. A.; Mekhilef, S.: Review: Uninterruptible power supply (UPS) system, *Renew. Sust. Energ. Rev.*, 2016, **58**, 1395–1410 DOI: [10.1016/j.rser.2015.12.335](https://doi.org/10.1016/j.rser.2015.12.335)
- [22] Korondi, P.; Hashimoto, H.: Park vector based sliding mode control of UPS with unbalanced and nonlinear load, in: Variable Structure Systems, Sliding Mode and Nonlinear Control (Springer, London, UK), 193–209 DOI: [10.1007/bfb0109978](https://doi.org/10.1007/bfb0109978)
- [23] Korondi, P.; Yang, S. H.; Hashimoto, H.; Harashima, F.: Sliding mode controller for parallel resonant dual converters, *J. Circ. Syst. Comp.*, 1995, **5**(4), 735–746 DOI: [10.1142/s0218126695000424](https://doi.org/10.1142/s0218126695000424)
- [24] Chang, E.-C.: Study and application of intelligent sliding mode control for voltage source inverters, *Energies*, 2018, **11**(10) 2544 DOI: [10.3390/en11102544](https://doi.org/10.3390/en11102544)
- [25] Széll, K.; Korondi, P.: Mathematical basis of sliding mode control of an uninterruptible power supply, *Acta Polytech. Hung.*, 2014, **11**(3), 87–106 DOI: [10.12700/APH.11.03.2014.03.6](https://doi.org/10.12700/APH.11.03.2014.03.6)
- [26] Keiel, G.; Flores, J. V.; Pereira, L. F. A.; Salton, A. T.: Discrete-time multiple resonant controller design for uninterruptible power supplies, *IFAC-PapersOnLine*, 2017, **50**(1), 6717–6722 DOI: [10.1016/j.ifacol.2017.08.1169](https://doi.org/10.1016/j.ifacol.2017.08.1169)
- [27] Khan, H. S.; Aamir, M.; Ali, M.; Waqar, A.; Ali, S. U.; Imtiaz, J.: Finite control set model predictive control for parallel connected online UPS system under unbalanced and nonlinear load, *Energies*, 2019, **12**(4), 581 DOI: [10.3390/en12040581](https://doi.org/10.3390/en12040581)

INFORMATIVE ENVIRONMENT QUALIFYING INDEX

ANETT UTASI ^{*1}, VIKTOR SEBESTYÉN¹, AND ÁKOS RÉDEY¹

¹Sustainability Solutions Research Lab, University of Pannonia, Egyetem u. 10, Veszprém, 8200, HUNGARY

Improvement in the quality of the environment and, as a result, in the quality of life, including environmental impact assessments and environmental management, play an important role in the practical implementation of environmental regulations.

The goal of this paper is to develop a new type of quantitative environmental impact assessment method to describe changes in environmental elements as well as the environment in an objective and reliable manner for various projects, investments, plans and proposals. An easily adaptable method was sought which provides a clear and well-interpretable result on the condition of and foreseeable changes in the environment.

The algorithm operates using the limit values of environmental elements set forth by national regulations. The evaluation is independent of the number of environmental parameters chosen as it was included in the informativity rates of the method. The process results in an aggregated index for qualifying the total environment but, nonetheless, the affected environmental elements and measured environmental parameters can be analysed independently. The Informative Environment Qualifying Index evaluates the environmental parameters in proportion to the strictness of the limit values. The final assessment of the total environment is performed by using varying intervals, therefore, the different cases can be compared to each other. Experts interpret the results as well as explain the changes in the state of the environment and, therefore, identify the cause-effect relationships.

Keywords: Environmental Impact Assessment, Quantitative methods, Informative Environment Qualifying Index, Environmental pollution

1. Introduction

The state of the environment has been changing drastically in an unfavourable direction due to economic development, rapid population growth, as well as increases in the rates of production and consumption resulting in extremely severe levels of environmental pollution amongst several other consequences. The European Union itself is committed to introduce actions and measures in order to take preventive steps to protect the environment. Regarding immediate actions to be implemented, environmental protection is an essential objective.

The Environmental Impact Assessment (EIA) and sustainability planning are intertwined. Both approaches aim to optimize future activities in an environmentally sound way and support decision-makers with appropriate, scientifically based evidence. Analyses must provide quantified information as well as easily understandable and comparable results, therefore, the aggregation of quantitative methods is widespread. The aim of this work is to develop an informative environment qualifying index. In addition to indexing based on immission limits, it is important to evaluate the sustainability of cities, for

which the SDEWES Index is an excellent approach [1]. This method has been implemented in Southeast European cities [2] and adapted for Hungarian cities [3].

Toro et al. developed a qualitative methodology for Environmental Impact Assessment (EIA) processes, which uses a double matrix to identify the impacts and assign quantitative values to the categories of quality [4].

Pavlickova and Vyskupova elaborated on a cumulative method for the evaluation of landscape vulnerability by taking this as well as ecological stability and the ratio of different measures of stability into account [5]. Herva and Roca reviewed the combined approaches and multi-criteria analysis for the purposes of evaluating corporate environmental performance. It was suggested to use the Multi-Criteria Decision-Making (MCDM) techniques in the industrial sector, decision-making in energy projects, waste management and wastewater treatment [6].

A possible method is the Environmental Impact Assessment, which comprises 25 different EIA methods as well as uses a quantitative framework and standard classification method as an optimal technique for the actual evaluation [7].

An integrated weight of evidence approach for environmental risk assessment proposed by Caeiro et al.

*Correspondence: utasi.anett@uni-pannon.hu

where anthropogenic pollution, the impacts on human health, the exposition of polluted wells and agricultural soils as well as pollutants in sediments are combined with 14 categories of absolute conditions [8]. Phillips used an enhanced Rapid Impact Assessment Matrix (RIAM) method to evaluate quantitatively the potential impacts of an onshore wind farm during its construction and operation [9], as well as for the sustainability evaluation of municipal solid waste management [10]. The RIAM approach was successfully used by Brindusa et al. to evaluate the environmental impacts resulting from heavy metal pollution on the southern coast of the Romanian Black Sea [11]. Sun and Wang developed a comprehensive EIA system for shale-gas exploration, which includes the evaluation systems of influence with regard to the natural and macro environments. The algorithm includes social, policy and economic impacts, therefore, it can be adapted to other fields of environmental analysis [12]. Robu et al. analysed the impacts and risks of heavy metal pollutants in bodies of surface water. The basis of such evaluations was the measured concentrations of the environmental parameters, therefore, the method is more objective [13]. The reliability of the different quantitative and qualitative methods may be increased by integrating the technical background of Environmental Risk Assessment [14]. An Environmental Evaluation System (EES) that incorporates relationships between environmental parameters and environmental quality was developed by Battelle Columbus Laboratories [15] and implemented for water resources planning by Ferreira et al. [16].

A review of aquatic environmental assessment methods was published by Foden et al. in which a new classification system is suggested that differentiates between static and dynamic links [17]. Yu et al. developed a universal calibrated model for the evaluation of bodies of surface- and groundwater. The main advantage of this algorithm is that it works with any combination of water quality indicators. It was developed in accordance with Chinese legislation, therefore, must be adapted for international applications [18].

On the basis of the literature review on EIA, it can be concluded that the aforementioned methods have several benefits, however, their limits should be taken into consideration. The main advantage of such methods is their suitability to compare different project alternatives. However, in light of its practical applications, two main issues need to be addressed. Namely, the assessment is based on the limit values of environmental parameters, measured/calculated values as well as the ranking/weighting/scaling of the environmental parameters and elements. In addition to these, it can also be concluded that the methods in the literature are less sensitive to extreme values, namely to discharges above the limit values.

In addition to environmental impacts, risk assessment is important for decision-makers. Wu et al. proposed a quantitative environmental risk assessment for the iron and steel industrial symbiosis network, which provides

an aggregate index value and is able to identify the most important driving forces [19]. Risks were identified in a chemical plant in Zhejiang province in China, where an index-based approach with the Analytic Hierarchy Process (AHP) and fuzzy operators was used for the evaluation [20].

The objective of this paper is to develop a new, easily adaptable, objective and reliable quantitative EIA method which provides an unambiguous outcome in the case of projects, investments, plants and proposals in comparison with the methods given in the literature. Environmental impacts should be identified during the early design phases [21] in order to avoid unlawful and polluting activities. A widely usable, target-oriented, objective and comprehensive new type of quantitative EIA technique was sought and its applicability verified.

The environmental impacts were linked to human activities in order to explore the cause-and-effect relationships, therefore, systems thinking is crucial in the case of an EIA. Rocha et al. developed a multiple indicator-based approach for environmental quality assessment in urban areas [22]. The proposed I_{IEQ} method is suitable for tracking environmental changes which can be linked to different human activities.

2. Results: Methodology

The Informative Environment Qualifying Index (I_{IEQ}) method was developed in accordance with legal and other relevant stipulations. The I_{IEQ} characterizing the total environment can be determined as depicted in Fig. 1.

The environmental assessment of alternatives to the project begins with screening the projects according to the applicable laws and regulations. The preparation of a reference databased Depends on the scope of the analysis. Firstly, the relevant environmental elements must be selected and their limit values determined. Following the preparation of the database, the algorithm is expanded by defining the environmental parameters studied for the selected environmental elements and the weighting of these parameters determined. The workflow of the method has been developed in such a way that it can be used to study an individual environmental element or complex cases, e.g. where several environmental elements are considered simultaneously. By analysing the environmental parameters (the second block in Fig. 1 which qualify the given environmental element, it is possible to plan the optimal mitigation strategy for that element. Therefore, the driving forces/drivers in the quality of the element are identified. The analysis with regard to the level of the environmental element provides a comprehensive picture of the state of the studied elements and important information in the evaluation of the environmental impacts of the projects. The environmental analysis (the last block in Fig. 1) ensures a basis for the comparison of the different cases investigated. The I_{IEQ} value helps decision-makers to determine the optimal measure or project alternative.

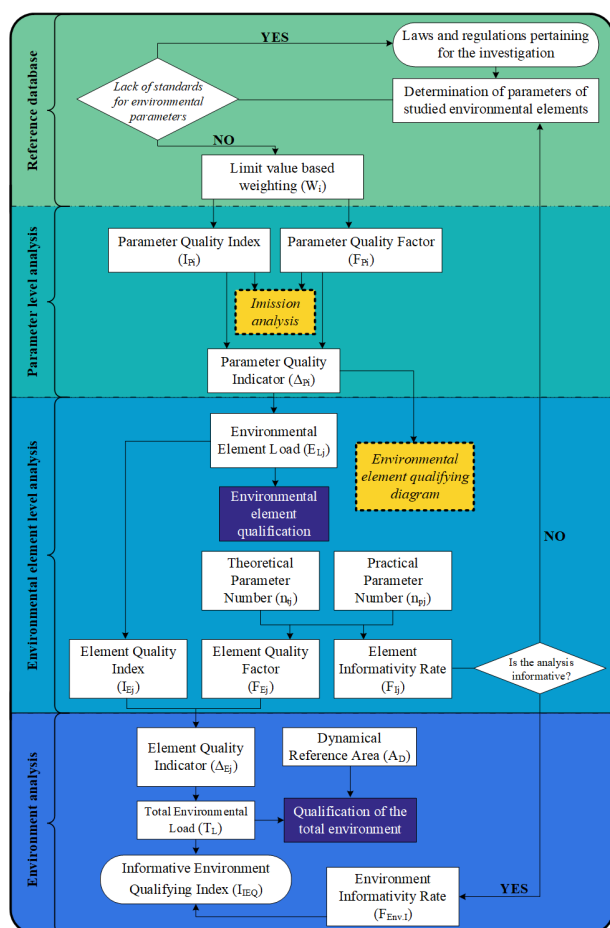


Figure 1: Methodology of the Informative Environment Qualifying Index

The method is suitable for multilevel analysis. The levels are represented by different colours in Fig. 1. The final outcome of the method is the determination of the I_{IEQ} . These steps are discussed in the following section.

2.1 Reference database

Laws and regulations pertaining to the investigation

The basis for the method is the set-up of the environmental reference database according to Hungarian stipulations. When used in other countries, the reference database should be adjusted to pertain to the legal regulations of the country in question. The environmental elements are studied in the present paper in light of the Hungarian law on the environment. The following environmental elements were taken into consideration:

1. Surface water: water flows (W)
2. Surface water: lakes (L)
3. Groundwater (G)
4. Soil (S)
5. Air (A)

Some EIA techniques, which were developed for the analyses of specific environmental elements, e.g. Németh

et al. provided a quantitative tool for bodies of surface water [23] to show changes in water quality of Lake Balaton, the largest natural shallow lake in Central Europe [24, 25]. In the case of air pollution, the Air Quality Index (AQI) is a useful tool to improve public understanding and participation [26]. Calculations of AQI can be supported by the two-phase decomposition technique and machine learning [27]. Indoor Environmental Quality (IEQ) can also be taken into consideration as this was analysed in a university building [28]. The EIA techniques can be sector-specific as well, e.g. Sanz et al. developed a new well-being index to describe the environmental quality of renewable energy sources and nuclear power [29].

One of the most important goals during the development of the I_{IEQ} was to provide a tool that facilitates the public understanding of environmental impacts in a simple, clear way, which includes more graphical representations of the impacts and is capable of describing changes in the state of the environment across an aggregated index value.

Determination of the environmental parameters for the environmental elements studied

Lists of environmental parameters are collected for every environmental element which is to be evaluated according to the pertaining stipulations. The database includes the names of the environmental parameters as well as their limit values and validity. The list for surface water is based on GD 2010 [31], the Water Framework Directive. The lists for soil as well as groundwater are based on GD 2006 [32], and the one for the environmental parameters of air can be defined on the basis of GD 2011 [33].

Environmental parameters for which no limit values are specified can be studied as well, since the numerical target for the environmental parameters should be determined by specialists and such values are to be included in the list of environmental parameters.

Weight of environmental parameters

Generally speaking, the objectivity of the EIA is compromised or questionable when a specialist defines the weighted preferences for the environmental parameters. In order to solve this problem, the authors have developed a weighting procedure based solely on environmental regulations and specifications. The hypothesis assumes that legislators took the risks and impacts of the environmental parameters into account whilst defining the limit values. The I_{IEQ} weighting procedure defines different categories of importance with regard to the environmental elements on the basis of the order of magnitude of the limit values. To determine the confined values of the intervals, the lowest (most severe) and highest (mildest) limit values should be sought in the specifications and classified in the appropriate categories of magnitude. The other limit values should be ranked between those two

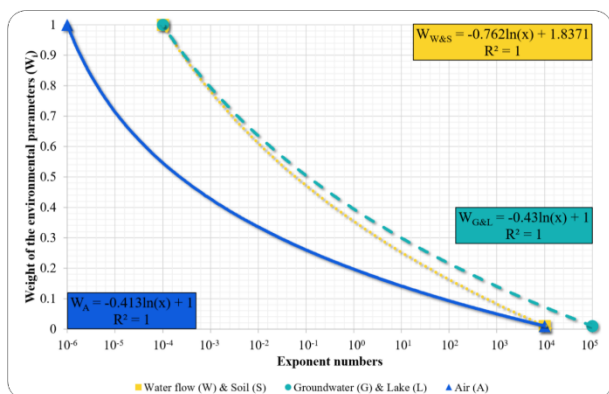


Figure 2: Weights of the various environmental elements

predefined confined values. The environmental parameters are classified by fitting a natural logarithmic curve as can be seen in Fig. 2, where the x and y axes indicate the magnitude and weight of the environmental parameters, respectively. Weights of 1 and 0.01 represent the most severe and mildest situations, respectively. The equations of the aligned curves are given in Fig. 2 by taking into consideration environmental elements (according to Hungarian regulations, the same magnitudes are assigned to certain environmental elements).

Fig. 2 presents the relationship between the air, bodies of surface water, soil and groundwater. Using the equations given in Fig. 2, weights, presented in Table 1, can be generated for the given environmental parameters. In the case of surface water, the limit value of $\text{PO}_4\text{-P}$ is $200\mu\text{g/l}$, which belongs to the order of magnitude of 10^2 , therefore, its value is 0.122. In the case of mercury, the limit value is $0.05\mu\text{g/l}$, which can be assigned to the order of magnitude of 10^{-2} , therefore, its value is 0.505.

Table 1: Weights according to orders of magnitude

Orders of magnitude of the environmental parameters studied	Exponent of 10	W_A	$W_{W\&S}$	$W_{G\&L}$
0.000001	-6	1	*o.r.	*o.r.
0.00001	-5	0.714	*o.r.	*o.r.
0.0001	-4	0.546	1	1
0.001	-3	0.427	0.687	0.714
0.01	-2	0.335	0.505	0.546
0.1	-1	0.26	0.375	0.427
1	0	0.196	0.274	0.335
10	1	0.141	0.192	0.26
100	2	0.093	0.122	0.196
1,000	3	0.049	0.062	0.141
10,000	4	0.010	0.010	0.093
100,000	5	*o.r.	*o.r.	0.01

*o.r.: outside the range of interpretation

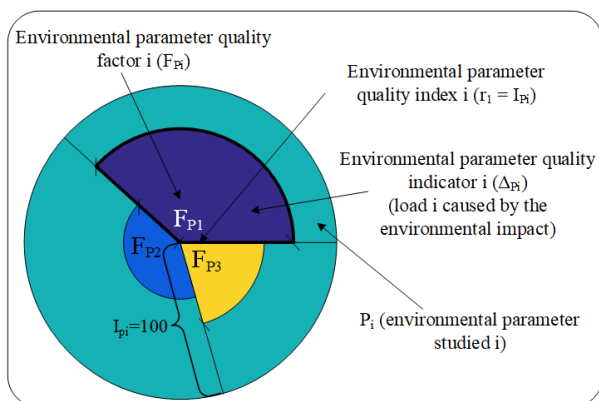


Figure 3: The qualifying diagram of an environmental element on the basis of the quality factor (F_{Pi}), quality index (I_{Pi}) and quality indicator (Δ_{Pi}) of the environmental parameter

2.2 Analysis of Parameters

In order to better understand the status of environmental elements, a visualization technique has been developed where the pollution/environmental load of an environmental element is represented by circles of defined radii and areas (Fig. 3). As a result, the parameters describing the environmental elements can be represented by segments of a circle (hereinafter referred to as “segment”). The following basic considerations were taken into consideration: the radii of the different segments are the ratios of the measured parameters to limit values expressed as percentages, referred to as the so-called environmental parameter quality index.

Environmental parameter quality index (I_{Pi})

The environmental parameter quality index (I_{Pi}) specifies the relationship between the immission concentration and limit values defined by the environmental specifications. I_{Pi} is determined by

$$I_{Pi} = \frac{M_{Vi}}{L_{Vi}} 100 \quad (1)$$

where I_{Pi} is the environmental parameter quality index for parameter i , M_{Vi} is the measured value of environmental parameter i , and L_{Vi} is the limit value of environmental parameter i .

If the value of I_{Pi} changes between 0 and 100%, the environmental parameter meets the legal specifications. However, if it exceeds 100%, the limit value is exceeded and mitigation measures must be considered.

Environmental parameter quality factor (F_{Pi})

The environmental parameter quality factor (P_i) is determined on the basis of the weight. The central angles (F_{P1} , F_{P2} , F_{P3}) of the circle as depicted in Fig. 3 are calculated by

$$F_{Pi} = W_i \frac{360}{\sum_{l=1}^{n_{Pj}} W_l} \quad (2)$$

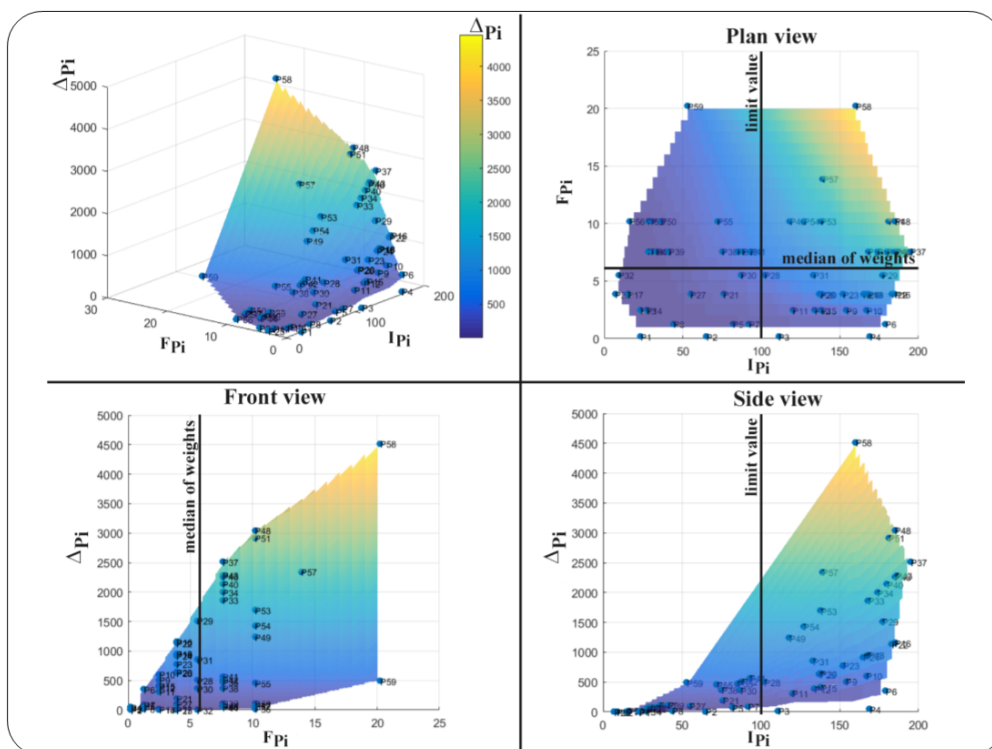


Figure 4: Immission analysis as a function of the environmental parameter quality index and factor

where F_{P_i} is the environmental parameter quality factor for environmental parameter i , W_i is the weight of the examined environmental parameter, and n_{P_j} is the number of environmental parameters in the case of environmental element i .

Environmental parameter quality indicator (Δ_{P_i})

The environmental parameter quality indicator (Δ_{P_i}) is given by

$$\Delta_{P_i} = (I_{P_i})^2 \pi \frac{F_{P_i}}{360} \tag{3}$$

where Δ_{P_i} is the environmental parameter quality indicator for environmental parameter i , I_{P_i} is the environmental parameter quality index for environmental parameter i (according to Eq. 1), and F_{P_i} is the environmental parameter quality factor for environmental parameter i (according to Eq. 2). The environmental parameter quality index for environmental parameter i is of square/quadratic form to emphasize the importance of the measured concentration of the parameter.

According to this interpretation, the different parameters with different units can be compared to each other so the environmental parameters can be easily qualified whether they exceed the limit values or fall within them. The central angles of the segments (F_{P_1} , F_{P_2} , F_{P_3}) represent the importance of the environmental parameter in question which is expressed as the environmental parameter quality factor as defined by Eq. 2.

Regarding Fig. 3, the expression of the environmental parameter quality indicator is introduced based on the

area of the segment (Eq. 3), which represents the extent to which the environmental parameter has an impact on the environmental element.

Immission analysis

The environmental parameters defined above can be illustrated in a three-dimensional system, therefore, the key parameters of the studied impact area identified. Fig. 4 illustrates the environmental parameter quality indicators (Δ_{P_i}) as a function of the environmental parameter quality factor (F_{P_i}) and the environmental parameter quality index (I_{P_i}). Fig. 4 shows the environmental parameters, their risks and the environmental damage caused should their values be extreme. According to the Informative Environment Qualifying Index method, the risk is a function of the specified limit value or target.

The following conclusions can be drawn on the basis of Fig. 4. The area (X_{min} ; Y_{min} ; Z_{min}) represents the group of environmental parameters for which the limit values are mildest and present in low concentrations, therefore, their negative impact on the environment is minimal.

The point (X_{max} ; Y_{max} ; Z_{max}) represents the group of environmental parameters for which the limit values are most severe and present in high concentrations, therefore, their negative impact on the environment is maximal.

According to the protocol defined here, the key factors can be identified on the basis of a system-oriented method and the outcome of the analysis used for plan-

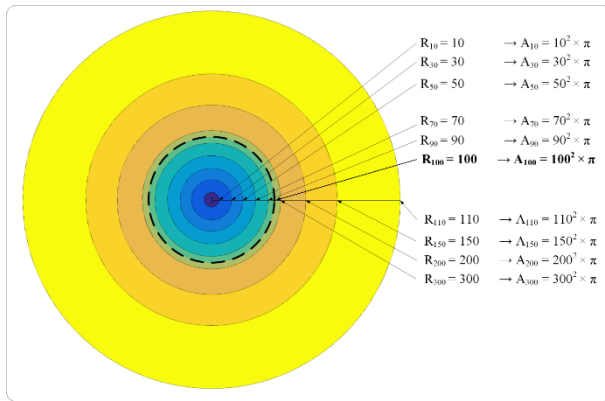


Figure 5: The relationship between the load of the environmental element and the reference areas

ning the environmental mitigation measures.

2.3 Analysis of the Environmental element level

The analysis of the environmental element level provides information to specialists about the cumulative impact of the environmental parameters on the environmental element in question.

Load of environmental elements (E_{Lj})

The cumulative environmental impacts of the environmental elements can be determined by totalling the environmental parameter quality indicators (ΔP_i), which are equal to the sum of the areas of the segments. The environmental element can be interpreted as a circle and the total levels of pollution stemming from the environmental parameters are represented by circles with different radii (Fig. 5).

In Fig. 4, the circle with $R = 100$ represents the case when the load of the environmental element is equal to the total limit load of the environmental parameters.

Qualification of environmental elements

For the numerical evaluation of an environmental element, the relationships required are defined in Table 2. On the basis of the outcome of case studies and professional experience, 10 categories were defined for the environmental evaluation: 10-30-50-70-90-100-110-150-200-300.

In Fig. 5, blue-coloured zones mark the acceptable categories (categories in Table 2: 10, 30 and 50), the green-coloured zones represent maximum environmental quality with regard to immission limit values (categories 70, 80 and 100), and the orange- as well as yellow-coloured zones represent situations when the level of pollution exceeds the limit value (categories 110, 150, 200 and 300).

Given these defined categories, the relative radius can be calculated from which, after working out the area of

the circle ($A_S = R^2\pi$), the corresponding area can be determined (A_S). This corresponding area can be interrelated to the load of the environmental parameters studied, that is to the total area of the segments (E_{Lj}) representing the environmental parameters.

From the load of the environmental parameters, the total area can be calculated by a numerical evaluation. The qualification/level of pollution of the environmental element can be determined from Table 2. The interval when the Load of the Environmental Element (E_{Lj}) is less than the reference area (A_S) needs to be determined.

Table 2 can be used generally to evaluate all environmental elements and is independent from the number of environmental parameters with regard to the environmental elements since the environmental parameter quality factors (F_{lip}) are normalized for 360°. The values of the environmental parameter quality factors depend on the number of environmental parameters and their weights.

Theoretical Number of Environmental Parameters (n_{tj})

The theoretical numbers of environmental parameters define the number of environmental parameters to be measured as well as monitored according to the stipulations and are based on the reference database. They are summarized in Table 3:

Practical Number of Environmental Parameters (n_{pj})

During the environmental impact assessment, specialists define the environmental elements to be studied and the scope of the environmental parameters. The set of environmental parameters can be different in the case of a natural environment, post-disaster situation or artificial environment. The method puts a special emphasis on the determination of the uncertainties.

Element Quality Index (I_{Ej})

The element quality index determines how the immission concentrations are related to the pollutants to be theoretically released into the environment:

$$I_{Ej} = \sqrt{\frac{E_{Lj}}{\pi}} \quad (4)$$

where I_{Ej} is the element quality index for environmental element j and E_{Lj} is the environmental load of environmental element j .

Element Quality Factor (F_{Ej})

The element quality factor (F_{Ej}) specifies the weight of the environmental element during the evaluation process. The goal of this factor is to take the number of environmental parameters into consideration (Eq. 7):

$$F_{Ej} = \frac{n_{pj}360}{\sum_{k=1}^m n_{tk}} \quad (5)$$

Table 2: The qualification system for evaluating the different environmental elements

Reference radius (R)	Reference area (A_S)	Evaluation
300	282743	The environmental element is seriously damaged which the ecosystem cannot tolerate.
200	125664	Natural regeneration is impossible because the environmental element is seriously damaged.
150	70686	Natural regeneration is inhibited because the environmental element is damaged.
110	38013	The concentrations of the environmental parameters defining the environmental element exceed the limit value.
100	31416	The concentrations of the environmental parameters defining the environmental element are equal to the limit values.
90	25447	The concentrations of the environmental parameters defining the environmental element are close to the limit value.
70	15394	The environmental element with environmental parameters below the limit value or influenced by anthropogenic impacts.
50	7854	The environmental element with minimal disturbances.
30	2827	The natural environmental element with indirect or direct anthropogenic impacts.
10	314	The natural environmental element free of anthropogenic impacts.

where F_{Ej} is the element quality factor for environmental element j , n_{pj} is the practical number of environmental parameters in the case of environmental element j , n_{tk} is the theoretical number of environmental parameters in the case of environmental element j (Table 3), and m is the number of environmental elements.

Environmental Element Informativity Rate (F_{Ij})

The environmental element informativity rate (F_{Ij}) represents the ratio of the number of theoretical environmental parameters (n_{tk}) for which legal requirements are in effect to the number of investigated environmental parameters. The ideal value of the environmental element informativity rate is equal to when all parameters set forth by the legal stipulations are involved in the investigation:

$$F_{Ij} = \frac{n_{pj}}{n_{tk}} \tag{6}$$

where F_{Ij} is the environmental element informativity rate for environmental element j , n_{pj} is the practical number of environmental parameters in the case of environmental element j , and n_{tk} is the theoretical number of environmental parameters in the case of environmental element k (Table 3).

2.4 Environmental analysis

The next step to be undertaken, following the investigation of the environmental parameters and elements, is the comprehensive analysis of the whole environment. The whole environmental system should be evaluated by taking the human, health, social, economic and cultural as-

Table 3: The theoretical numbers of environmental parameters (n_{tk}) for different environmental elements

Environmental element	Theoretical number of environmental parameters (pcs)
Surface water: water flow	59
Surface water: lake	59
Groundwater	58
Soil	52
Air	33

pects into consideration in an integrated way. It is insufficient to solely focus on the natural or artificial environment. The usability of a given project area depends on several factors, not only on the excellence of one environmental element. Therefore, a holistic approach is adopted during the evaluation.

Element Quality Indicator (Δ_{Ej})

The element quality indicator (Δ_{Ej}) enables the environmental element to be taken into consideration in light of the weights of the environmental parameters that describe the environmental element. Those environmental elements which are monitored less contribute to a lesser extent with regard to the characterization of the environment. During the analysis, the cumulative load of the environmental elements is taken into account:

$$\Delta_{Ej} = I_{Ej}^2 \pi \frac{F_{Ej}}{360} \tag{7}$$

where Δ_{Ej} is the element quality indicator for environmental element j , I_{Ej} is the element quality index for environmental element j (according to Eq. 4), and F_{Ej} is the element quality factor for environmental element j (according to Eq. 5).

Total Environmental Load (T_L)

The total environmental load (T_L) represents the proportional pollution of the whole environment, which can be generated by the summation of the element quality indicators (Δ_{EQj}). The environmental load is regarded as the most important issue during the calculation of the informative environment qualifying index (I_{IEQ}) as defined by

$$T_L = \sum_{j=1}^m \Delta_{Ej} \tag{8}$$

where T_L is the Total Environmental Load, Δ_{Ej} is the Element Quality Indicator for environmental element j (according to Eq. 7), and m is the number of environmental elements.

Table 4: Evaluation table of the whole environment

Reference radius (R)	Dynamical reference area (A_D)	Evaluation
300	$300^2\pi F_{Env.I}$	Degraded area which the ecosystems cannot accommodate.
200	$200^2\pi F_{Env.I}$	The natural regeneration of the environment is impossible because the area is severely damaged.
150	$150^2\pi F_{Env.I}$	Natural regeneration is inhibited because of the damaged area.
110	$110^2\pi F_{Env.I}$	The concentration of the environmental parameters exceeds the limit value.
100	$100^2\pi F_{Env.I}$	The concentration of the environmental parameters is equal to the limit value.
90	$90^2\pi F_{Env.I}$	The concentration of the environmental parameters is similar to the limit value.
70	$70^2\pi F_{Env.I}$	The environment is influenced by levels of pollution under the limit value and directly influenced by anthropogenic impacts.
50	$50^2\pi F_{Env.I}$	The environment closely resembles the natural conditions or with minimal disturbances.
30	$30^2\pi F_{Env.I}$	The natural environment with direct or indirect anthropogenic impacts.
10	$10^2\pi F_{Env.I}$	The natural environment free of anthropogenic impacts.

Qualification of the total environment

Table 4 is used to evaluate the total environment, which is based on dynamical reference areas as calculated from

$$A_D = R^2\pi F_{Env.I} \quad (9)$$

where A_D is the dynamical reference area (the level of the whole environment), R is the reference radius (Table 4), and $F_{Env.I}$ is the environment informativity rate (Eq. 10).

The basis of the dynamical reference area is the reference radius (Fig. 5 and Table 2) by which 10 different categories of quality were defined. The dynamical reference area depends on the ratio of the studied environmental parameters to the theoretical number of environmental parameters (informativity defined in the method).

The numerical assessment of the whole environment results in the element quality indices from the environmental load stemming from the total environmental parameters for the environmental elements. The evaluation of Table 4 concerns the results in terms of quality/pollution during the interval, in which case the value of the total environmental load (T_L) is less than the dynamical reference area (A_D).

Environment Informativity Rate ($F_{Env.I}$)

The environment informativity rate ($F_{Env.I}$) shows the depth of monitoring with regard to the environmental elements during the environmental evaluation:

$$F_{Env.I} = \frac{\sum_{j=1}^m n_{pj}}{\sum_{k=1}^m n_{tk}} \quad (10)$$

where $F_{Env.I}$ is the environment informativity rate, n_{pj} is the practical number of environmental parameters in the case of environmental element j , n_{tk} is the theoretical number of environmental parameters in the case of environmental element k , (Table 3), and m is the number of environmental elements.

The environment informativity rate ($F_{Env.I}$) indicates the coverage of the environmental parameters used in the investigation compared to the specified environmental parameters. The environmental impact assessment is more informative if the scope of the environmental parameters is larger.

$$\lim_{n_{pj} \rightarrow n_{tk}} (F_{Env.I}) = 1 \quad (11)$$

According to Eq. 11, the value of $F_{Env.I}$ approaches 1 if the practical number of environmental parameters (n_{pj}) closely resembles the theoretical number of parameters (n_{tk}).

Informative Environment Qualifying Index (I_{IEQ})

The final outcome of the method that is elaborated on is the informative environment qualifying index, which is a complex indicator (Eq. 12). The status of the environment is determined on the basis of the load of the different environmental elements and the informativity. Its value depends on the actual load of the environmental elements as well as the practical and theoretical numbers of environmental parameters.

From the reference radius of Table 4 during the evaluation, I_{IEQ} determines the accurate radius of the area derived from the actual load of the environmental elements:

$$I_{IEQ} = \sqrt{\frac{T_L}{\pi F_{Env.I}}} \quad (12)$$

where I_{IEQ} is the informative environment qualifying index, T_L is the total environmental load (Eq. 8), and $F_{Env.I}$ is the environment informativity rate (Eq. 10).

The application of the informative environment qualifying index provides a solid basis to compare the outcomes of different environmental evaluations since certain cases can differ from each other regarding the parameter sets. I_{IEQ} includes all these variables. The method can be expediently used to evaluate the environment before and after a disaster (e.g. the red mud disaster of Devecser), and the outcomes of the studies can be evaluated as a function of time. The method provides an opportunity to compare different cases (industrial parks, settlements, the natural environment) as well as provides a systemized and comprehensive approach to the evaluation.

2.5 A case study

Zirc is a small city in the heart of the Bakony Mountains in western Hungary. The city and its surroundings is a distinguished touristic area in Hungary with several natural attractions. An arboretum and National Parks are situated in the direct vicinity of the city. The water quality of the Cuha Stream which flows through the city is influenced

Table 5: The measured parameters of Zirc on June 13, 2016

The basic data of surface water		
Environmental parameters	Measured Value	Limit value
Electrical conductivity ($\mu\text{S}/\text{cm}$)	985	1,000
COD _{cr} ($\mu\text{g}/\text{l}$)	3,300	30,000
NO ₃ -N ($\mu\text{g}/\text{l}$)	1,497.24	2,000
NH ₄ -N ($\mu\text{g}/\text{l}$)	50	400
PO ₄ -P ($\mu\text{g}/\text{l}$)	169	200

The basic data of air		
Environmental parameters	Measured Value	Limit value
NO ($\mu\text{g}/\text{m}^3$)	3.708	100
NO _x ($\mu\text{g}/\text{m}^3$)	8.406	200
CO ($\mu\text{g}/\text{m}^3$)	278.77	10,000
O ₃ ($\mu\text{g}/\text{m}^3$)	80.77	120
Benzene ($\mu\text{g}/\text{m}^3$)	0.331	10
PM ₁₀ ($\mu\text{g}/\text{m}^3$)	16	50

by the wastewater treatment plant located here. The population of Zirc is 7,106 and the main economic activity in the region is agriculture.

During the field studies in the summer of 2016, two environmental elements were measured, namely surface water and air. The location of the measurement points is shown in Fig. 6.

In the case of surface water and air, the environmental parameters as defined in Table 5 were measured. The weights as well as quality indices, quality factors and quality indicators of parameters were determined and are summarized in Tables 6 and 7. F_{P_i} in the last rows of Tables 6 and 7 are used as a control since their total value must be equal to 360. Values of E_{L_j}, as defined in Table 2, constitute the basis of the numerical evaluation.

The value of the parameter quality index for the environmental parameter PO₄-P calculated on the basis of Eq. 1 is illustrated below. The measured value of the parameter PO₄-P was 169 mg/l and the limit value pertained to it was 200 mg/l [30].

$$I_{P_{PO_4-P}} = \frac{169(\frac{\text{mg}}{\text{l}})}{200(\frac{\text{mg}}{\text{l}})} 100 = 84.5$$

The parameter quality factor for the environmental parameter PO₄-P is determined on the basis of Eq. 2. The weight of PO₄-P is 0.12 and the five numbers in the denominator include the weight of the five environmental parameters of water.

$$F_{P_{PO_4-P}} = \frac{0.12 \cdot 360}{0.06+0.01+0.06+0.12+0.12} = 116.22$$

The values of I_{P_i} and F_{P_i} calculated for the environmental parameters listed in Tables 6 and 7 constitute the basis of the calculation. Parts A and B of Fig. 7 refer to the surface water and air, respectively.

On the basis of the parametric analysis of surface water, it can be concluded that the maximum limit value is defined for PO₄-P. Therefore, in the following steps, the

maximum weight (F_{P_i} = max) is assigned to PO₄-P. The electrical conductivity is close to the limit value and the parameter quality index of NO₃-N is ~ 75%. These parameters are key to improve the water quality in Zirc and are represented by circles in Fig. 7. A similar analysis of air was also carried out.

For the environmental parameter PO₄-P, the parameter quality indicator is based on Eq. 2 using the parameter quality index (84.50) and parameter quality factor (116.22):

$$\Delta_{P_{PO_4-P}} = 84.5^2 \cdot 3.14 \cdot \frac{116.22}{360} = 7,241.59$$

The quantitative analysis of the environmental elements of surface water and air is depicted in Fig. 8. Parts A and B of Fig. 8 refer to the surface water and air, respectively.

The weights of the environmental parameters can be seen in Fig. 8 during the evaluation procedure (the total of the interior angles of the segments is equal to F_{P_i}). The radii of the sectors are identical to the values of I_{P_i} which provide information on the quality. The load of the environmental element (E_{LW}) of the surface water is equal to 15,296. The qualification system for evaluation of the different environmental elements (Table 2) functions by substitution. An assignment in the category of R = 50 (environmental element with minimal disturbances, Table 2) is obtained. It can be concluded that the water quality of the Cuha Stream was disturbed to a minimal extent. Nevertheless, the ecosystem can tolerate this level of pollution.

By applying Eq. 4, the values of the environmental quality index express the actual loads of the environmental elements. On the basis of measurements in Zirc, the five parameters for surface water represent an area, I_{EW}, equal to R = 69.78, while the six environmental parameters for air represent an area, I_{EA}, of R = 31.58:

$$I_{EW} = \sqrt{\frac{15,295.6}{3.14}} = 69.78$$

$$I_{EA} = \sqrt{\frac{3,132.57}{3.14}} = 31.58$$

Following these steps, the aforementioned algorithm was followed. The element quality factors for water and air, F_{EW} and F_{EA}, were calculated according to the theoretical number of environmental parameters, altogether 92 parameters are to be monitored according to the specifications of GD 2010 [30] and GD 2011 [32]. In the case studies for surface water and air, five and six environmental parameters were investigated, respectively.

$$F_{EW} = \frac{5 \cdot 360}{92} = 19.57$$

$$F_{EA} = \frac{6 \cdot 360}{92} = 23.48$$

Next, the environmental element informativity rate was determined. The environmental element informativity rates for surface water and air are 0.08 and

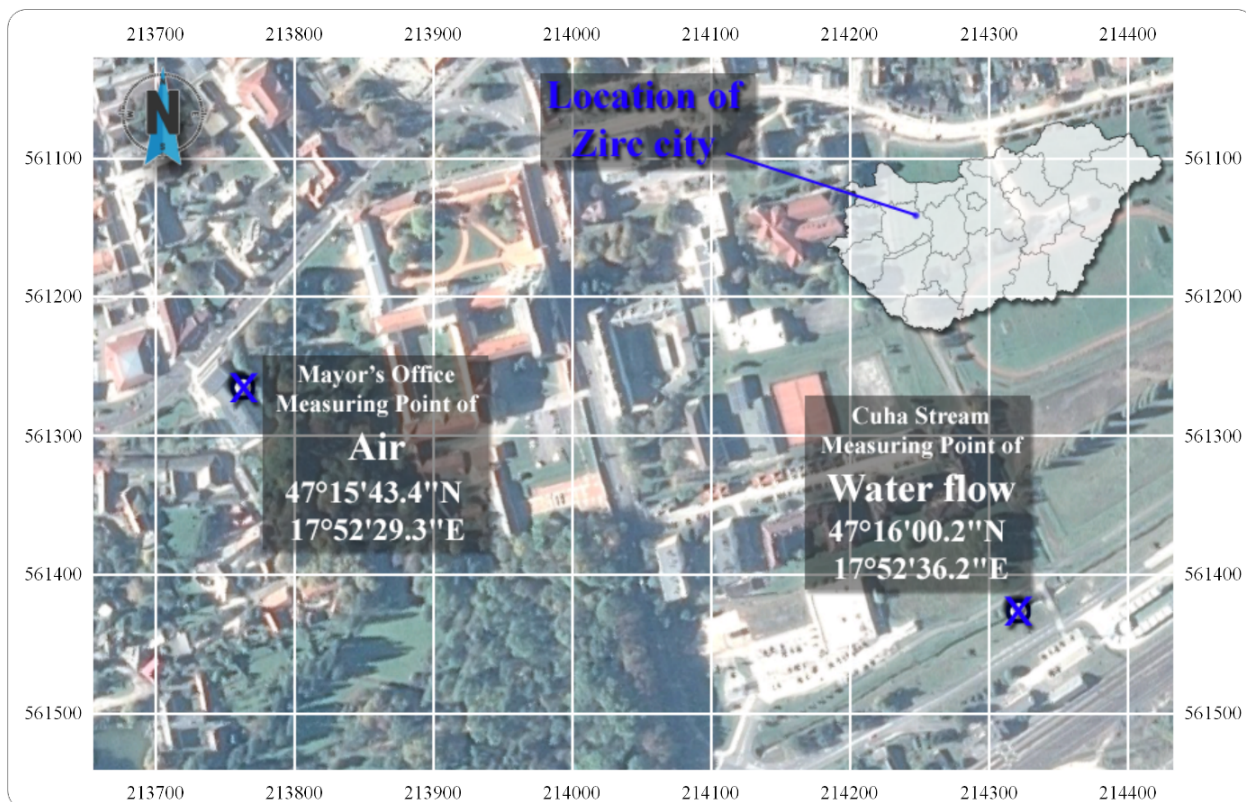


Figure 6: The measuring points and location of Zirc in Hungary

Table 6: The results of the calculations (Eqs. 1-3) for all measured parameters in the case of surface water from Cuha Stream, Zirc

Parameter (unit)	Measured value	Limit value	W_i	I_{Pi}	F_{Pi}	Δ_{Pi}
Electrical conductivity ($\mu\text{S}/\text{cm}$)	985	1,000	0.06	98.5	59.03	4,998.33
COD (mg/l)	3,300	30,000	0.01	11	9.5	10.03
$\text{NO}_3\text{-N}$ (mg/l)	1,497.24	2,000	0.06	74.86	59.03	2,887.19
$\text{NH}_4\text{-N}$ (mg/l)	50	400	0.12	12.5	116.22	158.47
$\text{PO}_4\text{-P}$ (mg/l)	169	200	0.12	84.5	116.22	7,241.59
Total	*n/a	*n/a	*n/a	*n/a	360	$E_{LW} = 15, 296.6$

*n/a: not applicable

Table 7: The results of the calculations (Eqs. 1-3) for all measured environmental parameters in the case of air in the vicinity of the Mayor's Office, Zirc

Parameter (unit)	Measured value	Limit value	W_i	I_{Pi}	F_{Pi}	Δ_{Pi}
NO_2 ($\mu\text{g}/\text{Nm}^3$)	3.71	100	0.09	3.71	58.45	7.01
NO_x ($\mu\text{g}/\text{Nm}^3$)	8.41	200	0.09	4.2	58.45	9.01
CO ($\mu\text{g}/\text{Nm}^3$)	278.77	10,000	0.01	2.79	6.32	0.43
O_3 ($\mu\text{g}/\text{Nm}^3$)	80.77	120	0.09	67.31	58.45	2,310.77
Benzene ($\mu\text{g}/\text{Nm}^3$)	0.33	10	0.14	3.31	89.17	8.53
PM_{10} ($\mu\text{g}/\text{Nm}^3$)	16	50	0.14	32	89.17	796.83
Total	*n/a	*n/a	*n/a	*n/a	360	$E_{LA} = 3, 132.57$

*n/a: not applicable

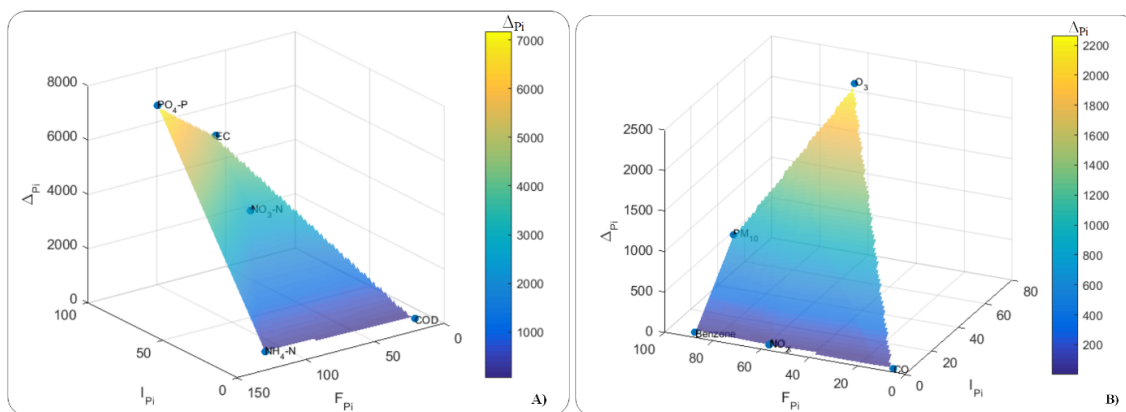


Figure 7: Immission analysis of the surface water (left-hand side, Part A) and air (right-hand side, Part B)

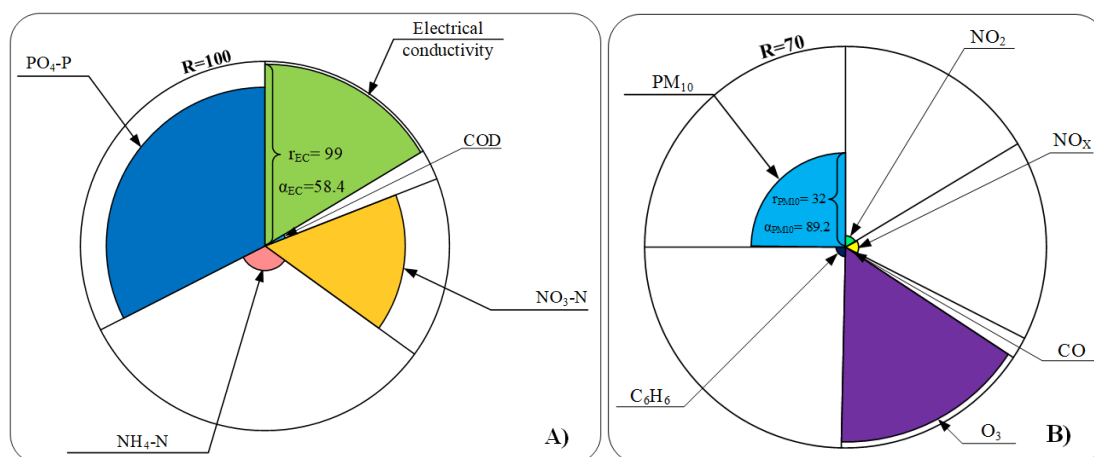


Figure 8: The quantitative analysis of the environmental elements (left-hand side: water, Part A; right-hand side: air, Part B)

0.18, respectively. It should be noted that the total of $F_{EQW}/F_{EIW} = 19.57/0.08 = 230.87$ and $F_{EQA}/F_{EIA} = 23.48/0.18 = 129.13$ is equal to 360.

$$F_{IW} = \frac{5}{59} = 0.08$$

$$F_{IA} = \frac{6}{33} = 0.18$$

On the basis of Eq. 7, the load of the whole environment (Δ_{Ej}) can be calculated using the actual load of the environmental elements. The actual load is substituted into the equation in the square/quadratic form, while n_{pj}/n_{tj} for the informativity is linear.

$$\Delta_{EW} = \frac{69.78^2 \cdot 3.14 \cdot 19.57}{360} = 831.28$$

$$\Delta_{EA} = \frac{31.58^2 \cdot 3.14 \cdot 23.48}{360} = 204.3$$

The total load of the environment is equal to the total of the summarized loads of the environmental elements (Eq. 8). In the case of Zirc, the larger proportion of environmental load stems from the surface-water pollution and the load of the air pollution represents roughly 20%.

$$T_L = 831.28 + 204.3 = 1,035.58$$

The whole environment can be evaluated by the dynamical reference areas as given by Eq. 9 and Table 4.

By substituting T_L into Table 4, it can be stated that the parameters describing the status of the environment are close to the concentrations of limit values. The radius assigned to the environmental quality of the city is equal to $R = 50$.

$$A_{50} = 50^2 \cdot 3.14 \cdot 0.12 = 939$$

In the aforementioned formula, the radius is equal to 50, representing the worst category of quality. The environmental element informativity rate is 0.12 (Eq. 10) which provides information on the number of environmental parameters in the study.

$$F_{Env.I} = \frac{5 + 6}{59 + 33} = 0.12$$

The Informative Environment Qualifying Index (I_{IEQ}) is calculated on the basis of Eq. 12:

$$I_{IEQ} = \sqrt{\frac{1,035.58}{3.14 \cdot 0.12}} = 52.51$$

I_{IEQ} of Zirc is 52.51. By substituting this value into Table 4, it can be seen that the environmental parameters

describing the status of the environment closely resemble the natural conditions with minimal disturbances. Specialists agree with the results, which are supported by the outcome of the field study.

3. Conclusion

The novelty of the Informative Environment Qualifying Index method is that the maximum environmental loads of the environmental parameters as stipulated in the legal specifications and the actually measured/calculated levels of pollution are taken into consideration when compared to the methods published in the literature. During the evaluation, the algorithm is applied at different levels, namely at the levels of environmental parameters, environmental elements and the total environment, to expediently elaborate on the planning of environmental mitigation measures. The quantitative methods used in the environmental impact assessment procedure include several subjective components during the weighting/ranking/scaling which could result in different interpretations with regard to the outcome of the evaluation. The Informative Environment Qualifying Index method is based on the specifications of national regulations, while the weight of the environmental elements depends on their status and the number of environmental parameters included in the study.

The Informative Environment Qualifying Index method is suitable for following up and monitoring the status of the environment in the cases of protected areas, national parks, urban areas, disasters, etc. The applicability of the method was demonstrated in the case of Zirc, a small city in the heart of the Bakony Mountains in western Hungary.

The scope of the evaluation ranges from the category “environment close to the natural conditions or with minimal disturbances” to “natural environmental elements with indirect or direct anthropogenic impacts”. The method casts light on the significant environmental impacts without concealing extreme situations nor distorting the final conclusions.

Acknowledgement

The financial support of Széchenyi 2020 under project GINOP-2.3.2-15-2016-00016 is acknowledged. The financial support of Széchenyi 2020 under the project EFOP-3.6.1-16-2016-00015 is acknowledged.

Nomenclature

Δ_{Ej}	Quality indicator for environmental element j
Δ_{Pi}	Quality indicator for environmental parameter i
A	Subscript, air
A_D	Dynamical reference area (level of the total environment)
A_S	Reference area (level of the environmental elements)
E_{Lj}	Environmental element load of environmental element j
F_{Ej}	Quality factor for environmental element j
$F_{Env.I}$	Informativity rate of total environment
F_{Ij}	Informativity rate of environmental element j
F_{Pi}	Quality factor for environmental element i
G	Subscript, groundwater
I_{Ej}	Quality index for environmental element j
I_{IEQ}	Informative environment qualifying index
I_{Pi}	Quality index for environmental element i
L	Subscript, surface water: lake
L_{vi}	Limit value of environmental parameter i
m	Number of environmental elements
M_{vi}	Measured value of environmental parameter i
n_{Pj}	Practical number of parameters in the case of element j
n_{tk}	Theoretical number of parameters in the case of element k
R	Reference radius
s	Subscript, soil
T_L	Total environmental load
w	Subscript, surface water: water flow
W_i, W_l	Weights of environmental parameters i and l

REFERENCES

- [1] Kılıç, Ş.: Composite index for benchmarking local energy systems of Mediterranean port cities, *Energy*, 2015, **92**(3), 622–638 DOI: [10.1016/j.energy.2015.06.093](https://doi.org/10.1016/j.energy.2015.06.093)
- [2] Kılıç, Ş.: Sustainable development of energy, water and environment systems index for Southeast European cities, *J. Cleaner Prod.*, 2016, **130**(1), 222–234 DOI: [10.1016/j.jclepro.2015.07.121](https://doi.org/10.1016/j.jclepro.2015.07.121)
- [3] Sebestyén, V.; Somogyi V.; Utasi A.: Adapting the SDEWES index to two Hungarian cities, *Hung. J. Ind. Chem.*, 2017, **45**(1), 49–59 DOI: [10.1515/hjic-2017-0008](https://doi.org/10.1515/hjic-2017-0008)
- [4] Toro, J.; Requena, I.; Duarte, O.; Zamorano, M.: A qualitative method proposal to improve environmental impact assessment, *Environ. Impact Assess. Rev.*, 2013, **43**, 9–20 DOI: [10.1016/j.eiar.2013.04.004](https://doi.org/10.1016/j.eiar.2013.04.004)
- [5] Pavlickova, K.; Vyskupova, M.: A method proposal for cumulative environmental impact assessment based on the landscape vulnerability evaluation, *Environ. Impact Assess. Rev.*, 2015, **50**, 74–84 DOI: [10.1016/j.eiar.2014.08.011](https://doi.org/10.1016/j.eiar.2014.08.011)

- [6] Herva, M.; Roca, E.: Review of combined approaches and multi-criteria analysis for corporate environmental evaluation, *J. Cleaner Prod.*, 2013, **39**, 355–371 DOI: [10.1016/j.jclepro.2012.07.058](https://doi.org/10.1016/j.jclepro.2012.07.058)
- [7] Carvalho, A.; Milmoso, A. F.; Mendes, A.N.; Matos, H. A.: From a literature review to a framework for environmental process impact assessment index, *J. Cleaner Prod.*, 2014, **64**, 36–62 DOI: [10.1016/j.jclepro.2013.08.010](https://doi.org/10.1016/j.jclepro.2013.08.010)
- [8] Caeiro, S.; Vaz-Fernandes, P.; Martinho, A. P.; Costa, P. M.; Silva, M. J.; Lavinha, J.; Matias-Dias, C.; Machado, A.; Castanheira, I.; Costa, M. H.: Environmental risk assessment in a contaminate estuary: An integrated weight of evidence approach as a decision support tool, *Ocean Coastal Manage.*, 2017, **143**, 51–62 DOI: [10.1016/j.ocecoaman.2016.09.026](https://doi.org/10.1016/j.ocecoaman.2016.09.026)
- [9] Phillips, J.: A quantitative-based evaluation of the environmental impact and sustainability of a proposed onshore wind farm in the United Kingdom, *Renewable Sustainable Energy Rev.*, 2015, **49**, 1261–1270 DOI: [10.1016/j.rser.2015.04.179](https://doi.org/10.1016/j.rser.2015.04.179)
- [10] Phillips, J.; Gholamalifard, M.: Quantitative evaluation of the sustainability or unsustainability of municipal solid waste options in Tabriz, Iran. *Int. J. Environ. Sci. Technol.*, 2016, **13**(6), 1615–1624 DOI: [10.1007/s13762-016-0997-0](https://doi.org/10.1007/s13762-016-0997-0)
- [11] Robu, B. M.; Jitar, O.; Teodosiu, C.; Strungaru, S. A.; Nicoara, M.; Plavan, G.: Environmental impact and risk assessment of the main pollution sources from the romanian black sea coast, *Environ. Eng. Manage. J.*, 2015, **14**(2), 331–340, <http://eemj.eu/index.php/EEMJ/article/view/2184>
- [12] Sun, R.; Wang, Z.: A comprehensive environmental impact assessment method for shale gas development, *Nat. Gas Ind. B*, 2015, **2**(2-3), 203–210 DOI: [10.1016/j.ngib.2015.07.012](https://doi.org/10.1016/j.ngib.2015.07.012)
- [13] Robu, B. M.; Bulgariu, D.; Bulgariu, L.; Macoveanu, M.: Quantification of impact and risk induced in surface water by heavy metals: case study – Bahlui River Iasi, *Environ. Eng. Manage. J.*, 2008, **7**(3), 263–267 <http://eemj.eu/index.php/EEMJ/article/view/417>
- [14] Robu, B. M.; Căliman, F. A.; Bețianu, C.; Gavrilesco, M.: Methods and procedures for environmental risk assessment, *Environ. Eng. Manage. J.*, 2007, **6**(6), 573–592 <http://eemj.eu/index.php/EEMJ/article/view/371>
- [15] Dee, N.; Baker, J.; Drobny, N.; Duke, K.; Whitman, I.; Fahringer, D.: An environmental evaluation system for water resource planning, *Water Resour. Res.*, 1972, **9**(3), 523–536 DOI: [10.1029/WR009i003p00523](https://doi.org/10.1029/WR009i003p00523)
- [16] Ferreira, A. P.; da Cunha, C. L. N.; Kling, A. S. M.: Environmental evaluation model for water resource planning. Study case: Piabanha hydrographic basin, Rio de Janeiro, Brazil, *Revista Eletoronicado Promeda.*, 2008, **2**(1), 7–18
- [17] Foden, J.; Rogers, S. I.; Jones, A. P.: A critical review of approaches to aquatic environmental assessment, *Mar. Pollut. Bull.*, 2008, **56**(11), 1825–1833 DOI: [10.1016/j.marpolbul.2008.08.017](https://doi.org/10.1016/j.marpolbul.2008.08.017)
- [18] Yu, C.; Yin, X.; Li, Z.; Yang, Z.: A universal calibrated model for the evaluation of surface water and groundwater quality: Model development and a case study in China, *J. Environ. Manage.*, 2015, **163**, 20–27 DOI: [10.1016/j.jenvman.2015.07.011](https://doi.org/10.1016/j.jenvman.2015.07.011)
- [19] Wu, J.; Pu, G.; Ma, Q.; Qi, H.; Wang, R.: Quantitative environmental risk assessment for the iron and steel industrial symbiosis network, *J. Cleaner Prod.*, 2017, **157**, 106–117 DOI: [10.1016/j.jclepro.2017.04.094](https://doi.org/10.1016/j.jclepro.2017.04.094)
- [20] Han, R.; Zhou, B.; An, L.; Jin, H.; Ma, L.; Li, N.; Xu, M.; Li, L.: Quantitative assessment of enterprise environmental risk mitigation in the context of Na-tech disasters, *Environ. Monit. Assess.*, 2019, **191**(4), 1–13 DOI: [10.1007/s10661-019-7351-1](https://doi.org/10.1007/s10661-019-7351-1)
- [21] Meex, E.; Hollberg, A.; Knapen, E.; Hildebrand, L.; Verbeeck, G.: Requirements for applying LCA-based environmental impact assessment tools in the early stages of building design, *Build. Environ.*, 2018, **133**, 228–236 DOI: [10.1016/j.buildenv.2018.02.016](https://doi.org/10.1016/j.buildenv.2018.02.016)
- [22] Rocha, C. A.; Sousa, F. W.; Zanella, M. E.; Oliveira, A. G.; Nascimento, R. F.; Souza, O. V.; Cajazeiras, I. M. P.; Lima, J. L. R.; Cavalcante, R. M.: Environmental quality assessment in areas used for physical activity and recreation in a city affected by intense urban expansion (Fortaleza-CE, Brazil): Implications for public health policy, *Environ. Sci. Pollut. Res.*, 2017, **9**(3), 169–182 DOI: [10.1007/s12403-016-0230-x](https://doi.org/10.1007/s12403-016-0230-x)
- [23] Németh, J.; Sebestyén, V.; Juzsakova, T.; Domokos, E.; Dióssy, L.; Le Phuoc, C.; Huszka, P.; Rédey, Á.: Methodology development on aquatic environmental assessment. *Environ. Sci. Pollut. Res.*, 2017, **24**(12), 11126–11140 DOI: [10.1007/s11356-016-7941-1](https://doi.org/10.1007/s11356-016-7941-1)
- [24] Sebestyén, V.; Németh, J.; Juzsakova, T.; Domokos, E.; Kovács, Zs.; Rédey, Á.: Aquatic environmental assessment of Lake Balaton in the light of physical-chemical water parameters, *Environ. Sci. Pollut. Res.*, 2017, **24**(32), 25355–25371 DOI: [10.1007/s11356-017-0163-3](https://doi.org/10.1007/s11356-017-0163-3)
- [25] Sebestyén, V.; Németh, J.; Juzsakova, T.; Domokos, E.; Rédey, Á.: Lake Balaton: Water Quality of the Largest Shallow Lake in Central Europe, *Encyclopedia of Water: Science, Technology, and Society*, 2019, 1–15 DOI: [10.1002/9781119300762.wsts0063](https://doi.org/10.1002/9781119300762.wsts0063)
- [26] Jiang, L.; Zhou, H.; Bai, L.; Zhou, P.: Does foreign direct investment drive environmental degradation in China? An empirical study based on air quality index from a spatial perspective, *J. Cleaner Prod.*, 2018, **176**, 864–872 DOI: [10.1016/j.jclepro.2017.12.048](https://doi.org/10.1016/j.jclepro.2017.12.048)
- [27] Wang, D.; Wei, S.; Luo, H.; Yue, C.; Grunder, O.: A novel hybrid model for air quality index forecasting based on two-phase decomposition technique and modified extreme learning ma-

- chine, *Sci. Total Environ.*, 2017, **580**, 719–733 DOI: [10.1016/j.scitotenv.2016.12.018](https://doi.org/10.1016/j.scitotenv.2016.12.018)
- [28] Zuhair, S.; Manton, R.; Griffin, C.; Hajdukiewicz, M.; Keana, M. M.; Goggins, J.: An Indoor Environmental Quality (IEQ) assessment of a partially-retrofitted university building, *Build. Environ.*, 2018, **139**, 69–85 DOI: [10.1016/j.buildenv.2018.05.001](https://doi.org/10.1016/j.buildenv.2018.05.001)
- [29] Sanz-Garcia, M. T.; Caselles Moncho, A.; Micó Ruiz, J. C.; Soler Fernández, D.: Including an environmental quality index in a demographic model, *Int. J. Global Warming* 2016, **9**(3), 362–396 DOI: [10.1504/IJGW.2016.075448](https://doi.org/10.1504/IJGW.2016.075448)
- [30] Sebestyén, V.; Somogyi, V.; Szőke, Sz.; Utasi, A.: Adapting the SDEWES index to two Hungarian cities, *Hung. J. Ind. Chem.*, 2017, **45**(1), 49–59 DOI: [10.1515/hjic-2017-0008](https://doi.org/10.1515/hjic-2017-0008)
- [31] GD (2010) Government Decree No. 10/2010. (VIII. 18.) of Ministry of Rural Development (VM) defining the rules for establishment and use of water pollution limits of surface water (in Hungarian)
- [32] GD (2006) Joint Government Decree No. 6/2009. (IV. 14.) of Ministry of Health and Ministry of Agriculture and Rural Development (KvVM-EüM-FVM) from the limit values and the measurement of pollutants for the protection from pollution of soil and groundwater (in Hungarian)
- [33] GD (2011) Government Decree No. 4/2011. (I. 14.) of Ministry of Rural Development (VM) from the ambient air quality limit values and the emission limit values of stationary point sources of air pollutants (in Hungarian)

THE EFFECT OF pH ON BIOSURFACTANT PRODUCTION BY *BACILLUS SUBTILIS* DSM10

RÉKA CZINKÓCZKY¹ AND ÁRON NÉMETH *¹

¹Department of Applied Biotechnology and Food Science, Budapest University of Technology and Economics, Műegyetem rkp. 3, Budapest, 1111, HUNGARY

The genus *Bacillus* has long been known for its ability to produce many industrially useful products. These bacteria mostly produce extracellular products like organic acids, enzymes and biosurfactants. In this paper, the production of surfactin using the *Bacillus subtilis* strain DSM10 is investigated. Biosurfactant was produced in a lab-scale 1-liter fermenter. pH control using different bases (NH₄OH and NaOH) was compared to observe whether the amount of produced biosurfactant or the quality of the product was influenced. The formation of the product was followed by measuring the surface tension, and the product formed was analyzed by reversed-phase chromatography. The investigation of the effect of pH control showed that it can be omitted during the fermentation of the biosurfactant. The highest concentration of surfactin (5 g/L) was achieved without pH control in contrast with when the pH was kept constant (pH = 7).

Keywords: biosurfactant, surfactin, fermentation, purification, *Bacillus subtilis*

1. Introduction

In recent years, the microbial production of tensio-active molecules with various properties, e.g. emulsifying, wetting, foaming, detergency, solubilizing and dispersing, has been gaining interest [1]. Biosurfactants are amphiphilic compounds produced by a variety of microbial communities. Natural surfactants are of great importance in the pharmaceutical, cosmetic, agricultural and food industries due to their beneficial properties including low toxicity, biodegradability, high selectivity and activity under extreme environmental conditions [2, 3]. The market of bio-based surfactants is predicted to be worth \$5.52 billion by 2022 [4]. This is unsurprising given our high degree of dependency on kinds of hygiene products, the majority of which include surfactants or emulsifiers.

Biosurfactants are classified based on their chemical structure into the following groups: glycolipids, lipopeptides, fatty acids and lipids, as well as polymeric and particulate biosurfactants [3, 5]. One of the most effective biosurfactants is surfactin. This lipopeptide-type surfactant contains a cyclic peptide linked to a fatty acid chain (Fig. 1) [6]. Bóka et al. reported that the molecular weights of surfactins range from 993 Da to 1049 Da [7]. Several gram-positive *Bacillus* species naturally produce surfactins, which help the bacteria to stabilize their cell membranes and adhere to a surface [8, 9]. The biosynthesis of surfactin occurs through different mechanisms: the conversion of glucose or glycerol as a substrate

to glucose 6-phosphate through the glycolytic pathway, providing the main precursor of carbohydrates located in the hydrophilic part and the oxidation of glucose to pyruvate then to acetyl-CoA, which serves as a precursor for the synthesis of lipids and amino acids (Asp, Glu, Leu, Val). However, if the substrate is a hydrocarbon, the metabolism is shifted towards the lipolytic pathway (β -oxidation into acetyl-CoA) and gluconeogenesis (acetyl-CoA involved in the synthesis of the precursor glucose 6-phosphate) [1].

The effectiveness of surfactants is defined by their ability to reduce the surface tension (ST), defined as the cohesive force between molecules which is proportional to the concentration of surfactant in the solution [2]. Their efficiency is measured by the critical micelle concentration (CMC) [1, 11]. Above the CMC, surfactants form micellar structures, but below it, the aggregates dissociate into monomers. Lipopeptides from *B. subtilis* are particularly compelling because their surface activity has been reported to be strong [6, 12, 13]. Powerful surfactants can decrease the surface tension of water (72 mN/m at 20 °C) to less than 30 mN/m [14]. The emulsifying capacity can be monitored by calculating the emulsification index (EI, %) and emulsion stability. As the pH decreases, surfactin becomes less soluble in water because the carboxyl group is protonated [12]. Under neutral or basic conditions, the carboxyl group is in the ionic form, thus its solubility and emulsification capability increases [15]. Moro et al. evaluated the influence of the pH on the stability of the surfactants produced by species of *B. subtilis*, *B. gibsonii* and *B.*

*Correspondence: naron@f-labor.mkt.bme.hu

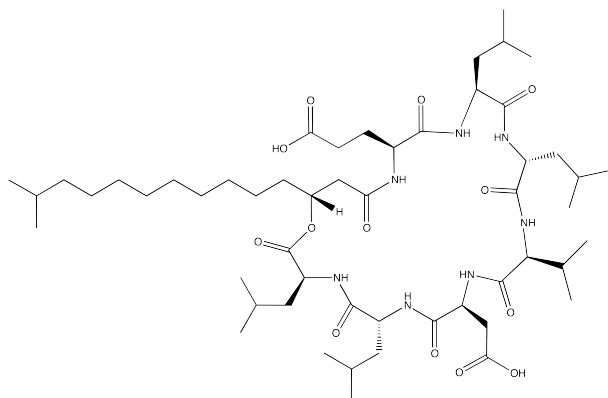


Figure 1: Chemical structure of surfactin: peptide loop of amino acids: five L-amino acids (Val, Asp, Leu, Glu and Leu) two D-amino acids (Leu and Leu), and a α , β -hydroxy C13-C15 fatty acid chain [10]

amyloliquefaciens [9]. All isolates exhibited surface tensions below 30 mN/m. In strongly acidic conditions, the emulsifying activity significantly decreased for both *B. subtilis* ODW02 and *B. subtilis* ODW15. As the pH was increased from 7 to 12, the stability of the surfactant produced by *B. subtilis* ODW02 decreased even further, but the one by *B. subtilis* ODW15 remained stable. In the case of *B. amyloliquefaciens* MO13, a significant increase was observed both under acidic and basic conditions. This different pH-responsive behavior makes surfactin applicable in a variety of industrial fields.

The choice of fermentation cultivation media (i.e. of average composition, carbon source, nitrogen source and trace elements) as well as fermentation strategies (i.e. temperature, pH, aeration and agitation) also need to be considered in relation to the type of applications. Based on a literature review, the best combination among the fermentation conditions was 1.5 vvm at 300 rpm, resulting in a maximum yield of surfactin of 6.45 g/L [16]. *B. subtilis* ATCC 21332 was grown on an iron-enriched minimal salt (MSI) medium including glucose (40 g/L). In a recent study, Yang et al. used nanoparticles (NPs) to improve the total yield of surfactin. 5 g/L of Fe NPs were added to the fermentation medium of *B. amyloliquefaciens* MT45, which increased the titer of surfactin from 5.94 to 9.18 g/L. Modifying the biosynthesis of surfactin with metabolic engineering tools can further increase production and titers of surfactin in *B. subtilis*, as demonstrated by Wu et al. (12.8 g/L) [17]. Few studies have focused on individual characteristics and relative amounts of surfactin variants in the extracts of lipopeptides. Many surfactin variants exist with various lengths of fatty acid chains and different amino acid sequences [5]. Akpa et al. analyzed the replacement of L-glutamic acid with four other amino acids, namely L-leucine, L-valine, L-isoleucine and L-threonine, in the culture medium. The presence of Thr was found to be favorable for the synthesis of longer (C15-C16) fatty acid chains in *B. subtilis* S499 [18]. Supplementation with Mn^{2+} , Cu^{2+} and Ni^{2+}

ions can also promote the production of novel variants of surfactin with different components of fatty acids (C16-C18) and amino acids (central aspartic acid methyl ester residue instead of aspartate) [19]. This approach can be useful for studying specific biological activities.

The objectives of our study were to explore the effect of pH control on the production of biosurfactants (i.e. on titers and productivity) by the *B. subtilis* strain DSM10 and evaluate the properties of biosurfactants, i.e. type, surface tension reduction and emulsifying activity.

2. Materials and methods

2.1 Cultivation conditions

Bacillus subtilis DSM10 (NCAIM B.02624T) was used for biosurfactant fermentation in this study. Cultivation was performed at 37 °C in 250 ml Erlenmeyer flasks containing 100 ml of an inorganic medium based on the composition used by Joshi et al. (2013): 34 g glucose, 1.0 g NH_4NO_3 , 6.0 g KH_2PO_4 , 2.7 g Na_2HPO_4 , 0.1 g $MgSO_4 \cdot 7 H_2O$, $1.2 \cdot 10^{-3}$ g $CaCl_2 \cdot 2 H_2O$, $1.65 \cdot 10^{-3}$ g $FeSO_4 \cdot 7 H_2O$, $1.5 \cdot 10^{-3}$ g $MnSO_4 \cdot 4 H_2O$ and $2.2 \cdot 10^{-3}$ g Na-EDTA [20].

The experiments were carried out in a 1 L benchtop bioreactor, with a working volume of 0.8 L (Biostat Q fermenter, B. Braun Biotech International, Germany) and a 10% v/v inoculum. For biosurfactant production, the temperature was adjusted to 37 °C with an agitation speed of 300 rpm and an aeration rate of 0.25 vvm. The pH was controlled by 25% H_2SO_4 and two different bases, namely 25% NH_4OH and 25% NaOH. Biosurfactant fermentation without external pH control served as a controlled experiment. A cyclone separator for reducing foam was connected to the outlet airstream of the fermenter (Fig. 2). The foam could overflow from the fermenter via the air outlet, through the cyclone separator to the collector flask.

2.2 Analysis of biomass

Bacterial growth was monitored by measuring the optical density of the fermentation broth at 600 nm using a Pharmacia LKB Ultrospec Plus spectrophotometer in comparison with that of the centrifuged supernatant of the sample.

The biomass concentration (g cell dry weight/L) was determined by using a calibration curve ($R^2 = 1$):

$$\text{Biomass [g/L]} = 0.4283 \cdot OD_{600} + 1.4568 \quad (1)$$

The sampled broth was centrifuged at 6,000 rpm for 15 mins. The cell pellets were collected and dried at 105 °C to constant weight by a Sartorius MA35 moisture analyzer to measure the cell dry weight.

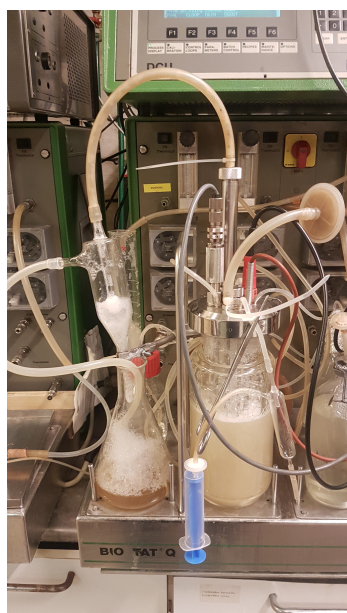


Figure 2: Fermentation setup with foam-separating glass cyclone

2.3 Analysis of glucose consumption

Glucose consumption was determined using the Waters Breeze 2 HPLC System. The mobile phase was 5 mM H_2SO_4 and the rate of elution was 0.5 mL/min. A BIO-RAD Aminex HPX-87H (300 × 7.8 mm, 9 μ m) column (65 °C) was applied with a Refractive Index detector (40 °C).

The glucose concentration was calculated from the peak area by the following calibration curve equation ($R^2 = 1$):

$$\text{Glucose [g/L]} = 4 \cdot 10^{-6} \cdot \text{PeakArea} + 0.0147 \quad (2)$$

2.4 Analysis of biosurfactants

Surface tension measurement

The surface activities of biosurfactants produced by the bacterial strains were determined by measuring the surface tension of the samples of cell-free broth using the stalagmometric method with a Traube Stalagmometer (2.5 mL, Wilmad-LabGlass LG-5050-102 Stalagmometer Tube for samples of low viscosity) at room temperature (25 °C). To increase the accuracy of the surface tension measurements, the averages of triplicates were used in this report. The surface tension can be determined based on the number of drops that fall per unit volume, the density of the sample and the surface tension of a liquid reference, e.g. deionized water.

The actual number of drops was calculated using

$$N = N_0 + \frac{x - y}{c} \quad (3)$$

where N denotes the number of drops of the sample calculated to the nearest tenth of a drop; N_0 represents an integer of drops counted between capillary-scale readings x

and y ; x and y stand for capillary-scale readings based on the maximum data point as 0 and the minimum data point as 40; x and y refer to the distances in millimeters from the beginning of each scale; and c is the capillary-scale calibration in millimeters per drop.

The surface tension (ST in mN/m) was calculated according to

$$ST = \frac{ST_w \cdot N_w \cdot D}{N \cdot D_w} \quad (4)$$

where ST_w denotes the surface tension of water at 25 °C (72 mN/m); N_w represents the number of water drops (20 drops); D stands for the density of the sample in g/mL; N refers to the number of drops of sample, and D_w is the density of water at 25 °C.

Emulsifying activity

The emulsifying activity was determined by the addition of 2 mL of sunflower oil to the same volume of cell-free sample or surfactin solution in a test tube, which was vortex-mixed vigorously for 2 mins. [21]. The tubes were incubated at 25 °C and the emulsification index (EI) determined after 24 hours according to:

$$EI_t = \left(\frac{H_e}{H_t} \right) 100 \quad (5)$$

where H_e and H_t are the height of emulsion and total height of the liquid in the tube, respectively.

To study the emulsion stability, the same protocol was used. The emulsification index (EI, %) was determined after 1 h and the EI measured after 24 h (EI_{24} , %), the tubes were incubated at 25 °C. The emulsion stability was expressed as a function of the changes in EI over the 24 h.

High-performance liquid chromatography (HPLC)

The surfactin concentration was measured by HPLC using a Waters Alliance 2695 Separations Module, which is a high-performance liquid chromatographic system equipped with a Waters 2996 photodiode array detector, at 205 nm and a Symmetry C18 Column (4.6 × 150 mm, 5 μ m - Waters, Ireland). The mobile phase consisted of 20% v/v trifluoroacetic acid (TFA) (3.8 mM) and 80% v/v acetonitrile. The elution rate was 1 mL/min at 25 °C and the sample volume was 10 μ L. The purified surfactin was identified by using commercially available surfactin (Wako Chemicals) as the authentic compound [22].

2.5 Isolation of the biosurfactant

The method for purifying the biosurfactant was adapted from the one outlined by Joshi et al. (2008) [23]. The cell-free broth was obtained by centrifuging the fermentation broth at 4,000 rpm for 20 mins. at 4 °C using a Janetzki MLW K23D centrifuge. The cell-free broth was used for further purification steps. The biosurfactant was recovered from the supernatant by acid precipitation: the

Table 1: Summary of the results of the fermentations

	without pH control	25% NH ₄ OH	25% NaOH
Biomass yield [g/g]	0.06±0.02	0.06±0.02	0.08
Biosurfactant yield [g/g]	0.120±0.04	0.073±0.07	0.123
Glucose conversion [%]	78.90±22	71.40±4	58.35
Final biosurfactant concentration [g/L]	3.36±2.3	2.00±1.5	2.34
Minimum surface tension [mN/m]	51.1±1	54.3±17	68.4
Biomass productivity [g/l·h]	0.060±0.03	0.089±0.05	0.064
Biosurfactant productivity [g/l·h]	0.100±0.05	0.034±0.02	0.064

pH was adjusted to 2.0 using 6 N HCl and kept at 4 °C overnight. The precipitate was collected by centrifugation at 4,000 rpm for 20 mins. at 4 °C, then resuspended in distilled water. The pH was adjusted to 7.0 using 6 N NaOH and the solution lyophilized by a Christ Alpha 2-4 LSC freeze dryer. The concentration of biosurfactant was determined gravimetrically from the resulting yellowish white powder. The concentration of biosurfactant was determined gravimetrically from the lyophilized powder. The identity of the purified biosurfactant was checked by HPLC.

2.6 Calculation of fermentation parameters

To compare the results of the fermentation, the following parameters were determined.

Substrate (glucose) conversion was calculated according to:

$$\Delta S \% = \frac{S_0 - S_f}{S_0} \quad (6)$$

where S_0 and S_f denote the initial substrate and final glucose concentrations, respectively.

The biomass yield on glucose ($Y_{\frac{x}{s}}$, g/g) was defined by:

$$Y_{\frac{x}{s}} = \frac{x_f - x_0}{S_0 - S_f} \quad (7)$$

where x_f and x_0 are the final and initial biomass concentrations, respectively.

The biosurfactant yield on glucose ($Y_{\frac{P}{s}}$, g/g) was defined by:

$$Y_{\frac{P}{s}} = \frac{P_f - P_0}{S_f - S_0} \quad (8)$$

where P_f and P_0 are the final and initial biosurfactant concentrations, respectively.

The volumetric productivities

$$J_x = \frac{x_{\max}}{t_{x_{\max}}} \quad (9)$$

and

$$J_P = \frac{P_{\max}}{t_{P_{\max}}} \quad (10)$$

(g/l · h) were calculated as the quotients of the maximum biomass concentration (x_{\max} , g/l) or the maximum biosurfactant concentration (P_{\max} , g/l) and the fermentation time ($t_{x_{\max}}$ or $t_{P_{\max}}$, h) when the maximum concentration was achieved, respectively.

3. Results and Discussion

To evaluate the effect of pH on surfactin production, a series of batch fermentations were performed either with or without pH control. The biosurfactant solution was analysed quantitatively and qualitatively using the HPLC method reported by Mubarak et al. [24].

An overview of the calculated parameters of the batch runs can be seen in Table 1. In the absence of pH control, the maximum biomass concentration achieved was 4.00 g/L after 35 h (Fig. 3). Without pH control, the increased acidity of the medium inhibited further growth at pH 4.4. The maximum biosurfactant concentration was 4.99 g/L, which resulted in the surface tension decreasing to 50.1 mN/m. In pH-controlled fermentations, the biomass yields (0.06 and 0.08 g/g - pH adjusted with 25% NH₄OH and 25% NaOH to 7.0, respectively) were similar to that in the absence of pH control (0.06 g/g) (Table 1), while the production of biosurfactants was unable, with a few exceptions, to reduce the surface tension significantly (66.5 mN/m with 25% NH₄OH, Table 1; Figs. 4 and 5). This may account for the presence of residual glucose concentrations of 8 to 12 g/L (Figs. 4 and 5). The maximum surfactant concentrations were 3.50 and 2.34 g/L by adjusting the pH using NH₄OH and NaOH, respectively. Although these results are similar to the average yield of surfactants (3.36 g/L) in the absence of pH control, a significant drop in productivity of approxi-

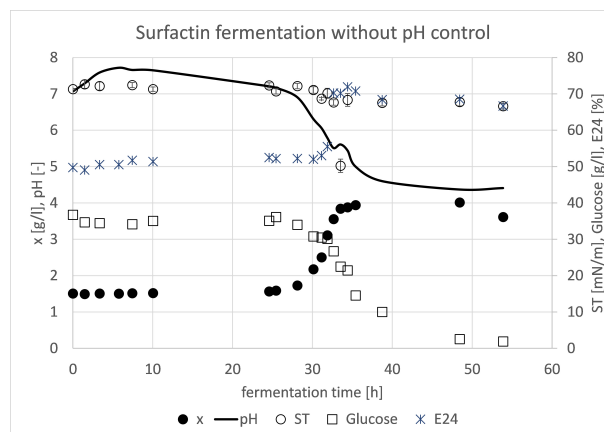


Figure 3: Fermentation of Surfactin - without external pH control

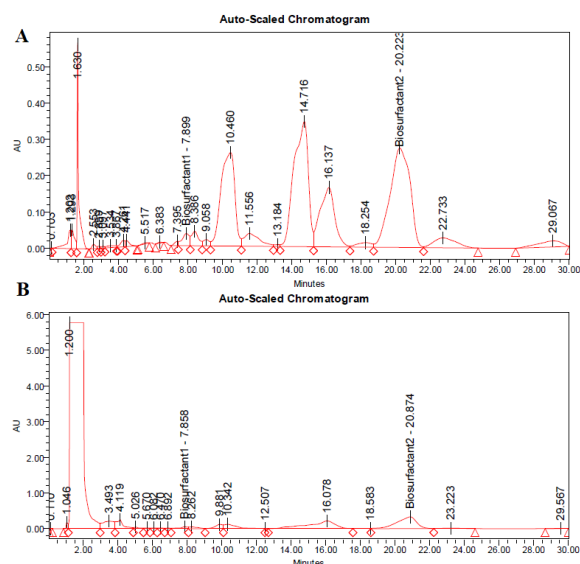


Figure 4: A) HPLC chromatogram of a 1.25 g/L surfactin standard, B) HPLC chromatogram of the isolated biosurfactant fraction from the foam out sample

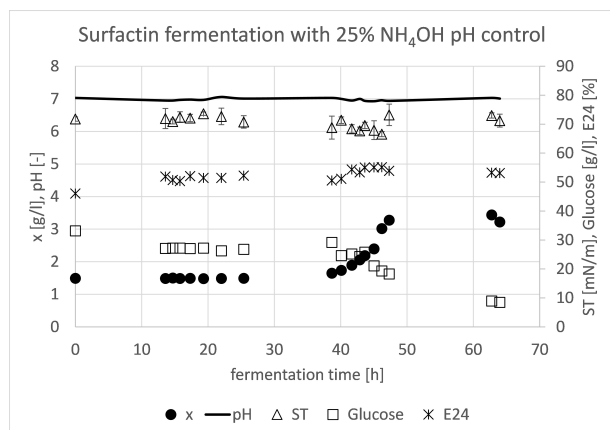


Figure 5: Fermentation of Surfactin - pH controlled by 25% NH₄OH.

mately 50% was observed (Table 1).

The highest value of the emulsifying activity (EI₂₄) was in excess of 70% at the end of the exponential phase of the growth curve (at 35 h, Fig. 3). The EI₂₄ values obtained from samples extracted from pH-controlled experiments increased from 45 to 55% (Figs. 5 and 6, respectively). These inconsistencies can be explained in part by the fact that different *Bacillus* species and strains are capable of producing numerous surfactin variants with distinct properties. It is highly likely that the production of surfactants is independent of cell growth as EI₂₄ decreased and ST increased during the stationary phase perhaps as a result of degradation by enzymatic hydrolysis or uptake under substrate-limiting conditions [25, 26].

Since the spectrum of lipopeptide-type biosurfactants is broad, the profiles of the extracts obtained after the purification process were compared to the surfactin standard. Fig. 4 presents two representative chromatograms:

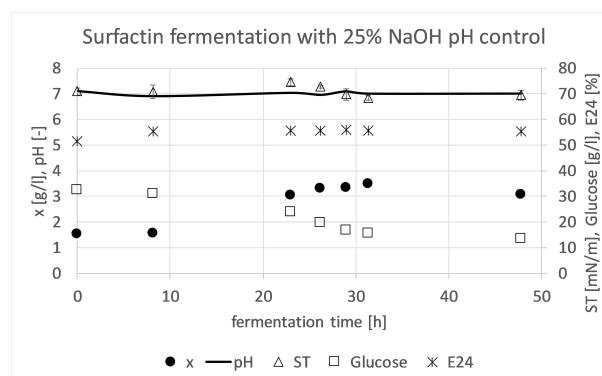


Figure 6: Fermentation of Surfactin - pH controlled by 25% NaOH

(A) surfactin standard and (B) purified culture broth of *B. subtilis DSM10*. Comparatively speaking, the samples from our study exhibited similar peaks (number of peaks, retention time). The intense peak at the beginning of the chromatogram indicates the presence of some non-retained impurities, namely contaminants and inorganic salts such as NH₄NO₃, which are often co-extracted with the targeted biosurfactant, that may need to be separated. Overall, based on the separation of peaks and retention time, the isolated biosurfactant was identified as surfactin.

The surfactin titer of *B. subtilis DSM10* was compared with the results from relevant studies (Table 2). Even though the fermentation strategies differ to some extent, the surfactin concentration from our work compares well with the values previously reported in the literature.

4. Conclusion

The aim of this study was to assess the biosurfactant-producing capability of *Bacillus subtilis DSM10* and establish an economically feasible fermentative process. This paper investigated the effect of pH control on the amount of biosurfactant production. The maximum amount of biosurfactant (approximately 5 g/L) was recovered from fermentation experiments in the absence of pH control at 37 °C. Furthermore, a preliminary characterization of the surface-active compounds produced during fermentation was conducted. HPLC analysis confirmed the presence of surfactin in the purified product.

Table 2: Surfactin production by *Bacillus* species

Strain	Surfactin titer [g/L]	Ref.
<i>B. subtilis ATCC 21332</i>	6.45	[16]
<i>B. subtilis</i>	2.00	[27]
<i>B. subtilis SPB1</i>	4.92	[28]
<i>B. subtilis DSM10T</i>	3.99	[29]
<i>B. subtilis #573</i>	4.80	[6]
<i>B. subtilis CN2</i>	7.15	[30]
<i>B. subtilis DSM10</i>	4.99	this work

The minimum surface tension was 50 mN/m. The emulsifying activity achieved using sunflower oil was approximately 70%. These results represent an initial step towards large-scale production of this biosurfactant. From a technical and economic standpoint, the fermentative process of surfactin carried out in the absence of pH control in a mineral salt medium using glucose as the sole carbon source seems to be an effective strategy for pilot- and industrial-scale production.

Acknowledgment

The research was supported by the Gedeon Richter's Talentum Foundation, founded by Gedeon Richter Plc. (Gedeon Richter Ph.D. fellowship). The research reported in this paper has been supported by the National Research, Development and Innovation Fund TUDFO/51757/2019-ITM, Thematic Excellence Program.

REFERENCES

- [1] Santos, D. K. F.; Rufino, R. D.; Luna, J. M.; Santos, V. A.; Sarubbo, L. A.: Biosurfactants: Multifunctional biomolecules of the 21st century. *Int. J. Mol. Sci.* 2016, **17**(3), 1–31 DOI: 10.3390/ijms17030401
- [2] Satpute, S. K.; Banpurkar, A. G.; Dhakephalkar, P. K.; Banat, I. M.; Chopade, B. A.: Methods for investigating biosurfactants and bioemulsifiers: A review. *Crit. Rev. Biotechnol.* 2010, **30**(2), 127–144 DOI: 10.3109/07388550903427280
- [3] Fenibo, E. O.; Douglas, S. I.; Stanley, H. O.: A review on microbial surfactants: Production, classifications, properties and characterization. *J. Adv. Microbiol.* 2019, **18**(3), 1–22 DOI: 10.9734/jamb/2019/v18i330170
- [4] Markets and Markets. Natural Surfactants Market (Bio-based Surfactants) <https://www.marketsandmarkets.com/search.asp?search=surfactants>
- [5] Sajna, K. V.; Höfer, R.; Sukumaran, R. K.; Gotumukkala, L. D.; Pandey, A.: White biotechnology in biosurfactants. in: *Industrial biorefineries and white biotechnology*; Elsevier B.V., 2015; pp. 499–521 DOI: 10.1016/B978-0-444-63453-5.00016-1
- [6] Gudiña, E. J.; Fernandes, E. C.; Rodrigues, A. I.; Teixeira, J. A.; Rodrigues, L. R.: Biosurfactant production by *Bacillus subtilis* using corn steep liquor as culture medium. *Front. Microbiol.* 2015, **6**, 1–7 DOI: 10.3389/fmicb.2015.00059
- [7] Bóka, B.; Manczinger, L.; Kecskeméti, A.; Chandrasekaran, M.; Kadaikunnan, S.; Alharbi, N. S.; Vágvolgyi, Cs.; Szekeres, A.: Ion trap mass spectrometry of surfactins produced by *Bacillus subtilis* SZMC6179J reveals novel fragmentation features of cyclic lipopeptides. *Rapid Commun. Mass Spectrom.* 2016, **30**(13), 1581–1590 DOI: 10.1002/rcm.7592
- [8] From, C.; Hormazabal, V.; Hardy, S. P.; Granum, P. E.: Cytotoxicity in *Bacillus mojavensis* is abolished following loss of surfactin synthesis: Implications for assessment of toxicity and food poisoning potential. *Int. J. Food Microbiol.* 2007, **117**(1), 43–49 DOI: 10.1016/j.ijfoodmicro.2007.01.013
- [9] Moro, G. V.; Almeida, R. T. R.; Napp, A. P.; Porto, C.; Pilau, E. J.; Lüdtke, D. S.; Moro, A. V.; Vainstein, M. H. Identification and ultra-high-performance liquid chromatography coupled with high-resolution mass spectrometry characterization of biosurfactants, including a new surfactin, isolated from oil-contaminated environments. *Microb. Biotechnol.* 2018, **11**(4), 759–769 DOI: 10.1111/1751-7915.13276
- [10] Surfactin - Wikimedia Commons. <https://commons.wikimedia.org/wiki/File:Surfactin.png>
- [11] De, S.; Malik, S.; Ghosh, A.; Saha, R.; Saha, B.: A review on natural surfactants. *RSC Adv.* 2015, **5**(81), 65757–65767 DOI: 10.1039/c5ra11101c
- [12] Nitschke, M.; Pastore, G. M.: Production and properties of a surfactant obtained from *Bacillus subtilis* grown on cassava wastewater. *Bioresour. Technol.* 2006, **97**(2), 336–341 DOI: 10.1016/j.biortech.2005.02.044
- [13] Fonseca, R. R.; Silva, A. J. R.; De França, F. P.; Cardoso, V. L.; Sérvulo, E. F. C.: Optimizing carbon/nitrogen ratio for biosurfactant production by a *Bacillus subtilis* strain. *Appl. Biochem. Biotechnol.* 2007, **137**(1), 471–486 DOI: 10.1007/s12010-007-9073-z
- [14] Seydlová, G.; Svobodová, J.: Review of surfactin chemical properties and the potential biomedical applications. *Cent. Eur. J. Med.* 2008, **3**(2), 123–133 DOI: 10.2478/s11536-008-0002-5
- [15] Long, X.; He, N.; He, Y.; Jiang, J.; Wu, T.: Biosurfactant surfactin with pH-regulated emulsification activity for efficient oil separation when used as emulsifier. *Bioresour. Technol.* 2017, **241**, 200–206 DOI: 10.1016/j.biortech.2017.05.120
- [16] Yeh, M.-S.; Wei, Y.-H.; Chang, J.-S.: Bioreactor design for enhanced carrier-assisted surfactin production with *Bacillus subtilis*. *Process Biochem.* 2006, **41**(8), 1799–1805 DOI: 10.1016/j.procbio.2006.03.027
- [17] Wu, Q.; Zhi, Y.; Xu, Y.: Systematically engineering the biosynthesis of a green biosurfactant surfactin by *Bacillus subtilis* 168. *Metab. Eng.* 2019, **52**, 87–97 DOI: 10.1016/j.ymben.2018.11.004
- [18] Akpa, E.; Jacques, P.; Wathélet, B.; Paquot, M.; Fuchs, R.; Budzikiewicz, H.; Thonart, P.: Influence of culture conditions on lipopeptide production by *Bacillus subtilis*. *Appl. Biochem. Biotechnol. - Part A Enzym. Eng. Biotechnol.* 2001, **91**, 551–561 DOI: 10.1385/ABAB:91-93:1-9:551
- [19] Bartal, A.; Vigneshwari, A.; Bóka, B.; Vörös, M.; Takács, I.; Kredics, L.; Manczinger, L.; Varga, M.; Vágvolgyi, Cs.; Szekeres, A.: Effects

- of different cultivation parameters on the production of surfactin variants by a *Bacillus subtilis* strain. *Molecules*, 2018, **23**(10), 2675 DOI: [10.3390/molecules23102675](https://doi.org/10.3390/molecules23102675)
- [20] Joshi, S. J.; Geetha, S. J.; Yadav, S.; Desai, A. J.: Optimization of bench-scale production of biosurfactant by *Bacillus licheniformis* R2. *APCBEE Procedia* 2013, **5**, 232–236 DOI: [10.1016/j.apcbee.2013.05.040](https://doi.org/10.1016/j.apcbee.2013.05.040)
- [21] Vaz, D. A.; Gudiña, E. J.; Alameda, E. J.; Teixeira, J. A.; Rodrigues, L. R.: Performance of a biosurfactant produced by a *Bacillus subtilis* strain isolated from crude oil samples as compared to commercial chemical surfactants. *Colloids Surf. B: Biointerfaces* 2012, **89**, 167–174 DOI: [10.1016/j.colsurfb.2011.09.009](https://doi.org/10.1016/j.colsurfb.2011.09.009)
- [22] Freitas de Oliveira, D. W.; Lima França, Í. W.; Nogueira Félix, A. K.; Lima Martins, J. J.; Aparecida Giro, M. E.; Melo, V. M. M.; Gonçalves, L. R. B.: Kinetic study of biosurfactant production by *Bacillus subtilis* LAMI005 grown in clarified cashew apple juice. *Colloids Surf. B: Biointerfaces* 2013, **101**, 34–43 DOI: [10.1016/j.colsurfb.2012.06.011](https://doi.org/10.1016/j.colsurfb.2012.06.011)
- [23] Joshi, S.; Bharucha, C.; Desai, A. J.: Production of biosurfactant and antifungal compound by fermented food isolate *Bacillus subtilis* 20B. *Bioresour. Technol.* 2008, **99**(11), 4603–4608 DOI: [10.1016/j.biortech.2007.07.030](https://doi.org/10.1016/j.biortech.2007.07.030)
- [24] Mubarak, M. Q. E.; Hassan, A. R.; Hamid, A. A.; Khalil, S.; Isa, M. H. M.: A simple and effective isocratic HPLC method for fast identification and quantification of surfactin. *Sains Malaysiana* 2015, **44**(1), 115–120 DOI: [10.17576/jsm-2015-4401-16](https://doi.org/10.17576/jsm-2015-4401-16)
- [25] Mukherjee, S.; Das, P.; Sivapathasekaran, C.; Sen, R.: Antimicrobial biosurfactants from marine *Bacillus circulans*: Extracellular synthesis and purification. *Lett. Appl. Microbiol.* 2009, **48**(3), 281–288 DOI: [10.1111/j.1472-765X.2008.02485.x](https://doi.org/10.1111/j.1472-765X.2008.02485.x)
- [26] Rodríguez, N.; Salgado, J. M.; Cortés, S.; Domínguez, J. M.: Alternatives for biosurfactants and bacteriocins extraction from *Lactococcus lactis* cultures produced under different pH conditions. *Lett. Appl. Microbiol.* 2010, **51**(2), 226–233 DOI: [10.1111/j.1472-765X.2010.02882.x](https://doi.org/10.1111/j.1472-765X.2010.02882.x)
- [27] Amani, H.; Mehrnia, M. R.; Sarrafzadeh, M. H.; Haghighi, M.; Soudi, M. R.: Scale up and application of biosurfactant from *Bacillus subtilis* in enhanced oil recovery. *Appl. Biochem. Biotechnol.* 2010, **162**(2), 510–523 DOI: [10.1007/s12010-009-8889-0](https://doi.org/10.1007/s12010-009-8889-0)
- [28] Ghribi, D.; Ellouze-Chaabouni, S.: Enhancement of *Bacillus subtilis* lipopeptide biosurfactants production through optimization of medium composition and adequate control of aeration. *Biotechnol. Res. Int.* 2011, 1–6 DOI: [10.4061/2011/653654](https://doi.org/10.4061/2011/653654)
- [29] Willenbacher, J.; Rau, J. T.; Rogalla, J.; Syldatk, C.; Hausmann, R.: Foam-free production of surfactin via anaerobic fermentation of *Bacillus subtilis* DSM 10^T. *AMB Express* 2015, **5**(1) DOI: [10.1186/s13568-015-0107-6](https://doi.org/10.1186/s13568-015-0107-6)
- [30] Bezza, F. A.; Chirwa, E. M. N.: Production and applications of lipopeptide biosurfactant for bioremediation and oil recovery by *Bacillus subtilis* CN2. *Biochem. Eng. J.* 2015, **101**, 168–178 DOI: [10.1016/j.bej.2015.05.007](https://doi.org/10.1016/j.bej.2015.05.007)

ADSORPTION OF NICKEL IONS FROM PETROLEUM WASTEWATER ONTO CALCINED KAOLIN CLAY: ISOTHERM, KINETIC AND THERMODYNAMIC STUDIES

ALEXANDER ASANJA JOCK ^{*1}, ANIETIE NDARAKE OKON¹, UCHECHUKWU HERBERT OFFOR¹, FESTUS THOMAS², AND EDMOND OKWUDILICHUKWU AGBANAJE³

¹Department of Chemical and Petroleum Engineering, University of Uyo, PMB 1017, Uyo, NIGERIA

²Department of Engineering Infrastructure, National Agency for Science and Engineering Infrastructure (NASENI), Idu Industrial Area, PMB 391, Garki-Abuja, NIGERIA

³Chemical and Petroleum Technique, Department of Science Laboratory Technology, University of Jos, PMB 2084, Jos, NIGERIA

The removal of nickel ions onto calcined kaolin clay using a batch adsorption technique was conducted. The effect of the adsorbent mass, contact time and temperature on the removal process was investigated. The calcined kaolin clay was characterized using X-ray fluorescence (XRF) and Fourier-Transform InfraRed spectroscopy (FTIR). The adsorption data was analyzed by isotherm, kinetic and thermodynamic studies. The major chemical components in the clay are alumina (41.14 wt %) and silica (53.16 wt %). FTIR showed that the functional groups of aluminium monoxide (Al-O) and silicon monoxide (Si-O) are present in the clay. The study yielded a removal efficiency of 89.89% for nickel ions at 25 °C. The adsorption process appeared to follow a Freundlich isotherm and pseudo-second order kinetics were found to be in good agreement with the experimental data. The thermodynamics of the rate processes showed the adsorption of nickel ions to be endothermic and negative values of Gibbs free energy indicated the spontaneity of these processes. This proves that calcined kaolin clay is a good material for the removal of nickel ions from the wastewater produced by petroleum refineries.

Keywords: Adsorption, Kaolin, Nickel, Wastewater

1. Introduction

Environmental pollution is an anthropogenic phenomenon and mainly a result of industrialization. The contamination of bodies of water by the indiscriminate disposal of heavy metals has led to serious threats to humans as well as aquatic and living creatures. Nickel compounds are highly toxic contaminants and are emitted into the environment from various industries, e.g. mining, metal coatings, batteries, chemical, tanneries, etc., in quantities that pose risks to human health [1].

Many wastewater treatment methods have been introduced to control water pollution such as chemical precipitation, ion exchange, electrodialysis, reverse osmosis as well as membrane filtration and adsorption. Adsorption is one of the most efficient techniques due to its simplicity and affordability, moreover, it is more feasible even at low concentrations of heavy metal ions [2]. The adsorbent used for the adsorption process is of organic origin, e.g. activated carbon and biosorbents, or mineral origin, e.g. natural zeolite, calcium silicate powder and natural clay

[3]. Activated carbon is the most commonly used adsorbent for wastewater treatment but due to its expense, low-cost alternatives such as clay, coal, fly ash, peat, siderite, agricultural wastes and charcoal are being developed. Low-cost adsorbents are those that require little processing and are abundant in nature, by-products or waste materials from industry [4]. Clay minerals such as kaolinite, montmorillonite, vermiculite and illite are potential adsorbents of heavy metals. They have several economic advantages and intrinsic characteristics, e.g. are readily available, inexpensive, have excellent textural and surface properties, are physically and chemically stable in harsh environments as well as offer a cost-effective alternative to the conventional treatment of wastewater [5]. The aim of this study is to investigate the removal of nickel ions from wastewater produced by petroleum refineries using calcined kaolin clay from Alkaleri in North-East Nigeria.

2. Materials and Methods

2.1 Beneficiation and calcination of samples

10 kg of raw kaolin clay was crushed and soaked in water for 24 hours. The clay-water mixture was plunged for 3

*Correspondence: alsanja@gmail.com

hours at room temperature. Colloidal kaolin clay was separated from the quartz-rich sediment and sieved through a 230 mesh Tyler sieve to remove other coarse impurities. The thickened clay was then put in a filter cloth and pressed under hydraulic pressure to squeeze out the water. The cake was dried in an oven at 110 °C to constant weight before being pulverized.

100 g of the beneficiated clay was fired gradually in an electric furnace at 650 °C for 3 hours before being soaked. The calcined clay adsorbent was cooled, characterized and used for adsorption experiments.

2.2 Batch Adsorption

The wastewater used of a known initial concentration of nickel ions was obtained from the effluent of a petroleum refinery operated by Kaduna Refining and Petrochemicals Company. The batch experiments were conducted by varying the adsorbent mass, contact time and temperature as described. The effect of the adsorbent mass was determined at 25 °C and 0.5 g of oven-dried calcined kaolin was mixed with 50 mL of wastewater in a 250 mL Erlenmeyer flask. The mixture was stirred with a magnetic stirrer at 200 rpm for between 10 and 50 mins. The process was repeated by varying the adsorbent mass in increments of 0.5 g, namely 1.0, 1.5, 2.0 and 2.5 g. The effect of the contact time was analyzed using 0.5 g of adsorbent after 10, 20, 30, 40 and 50 mins. The effect of the temperature was investigated within the range of 25-65 °C following a contact time of 30 mins. with adsorbent masses of 0.5 and 2.5 g. The residual Ni(II) ions obtained from the filtrate and determined by Atomic Absorption Spectroscopy (AAS) were analyzed to evaluate the percentage removal, adsorption kinetics and thermodynamics.

3. Results and Discussion

3.1 Characterization of the adsorbent

Chemical composition

The chemical composition of the adsorbent is shown in Table 1. The main components of the clay are SiO₂ (53.158 wt %) and Al₂O₃ (41.143 wt %). Metallic oxides such as TiO₂, MgO and Fe₂O₃ are present in small amounts, while traces of CaO, Cr₂O₃, ZnO and Mn₂O₃ are detected.

The large amounts of SiO₂ and Al₂O₃ present define the sample as an aluminosilicate clay. Generally speaking, kaolin clay, the chemical formula of which is Al₂Si₂O₅(OH)₄, is principally composed of SiO₂, Al₂O₃ and water [6].

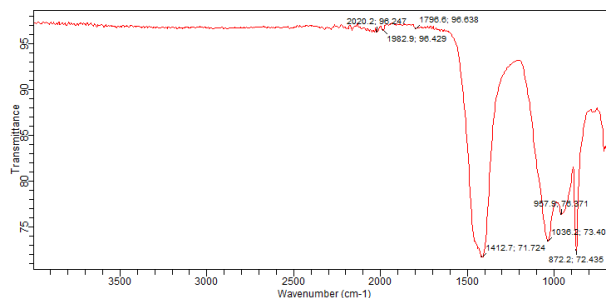


Figure 1: Fourier-transform infrared spectrum of calcined kaolin clay

Fourier-transform infrared spectroscopy

Fourier Transform InfraRed spectroscopy (FTIR) shows the functional groups present in the sample of clay. The FTIR spectra of the kaolin clay shown in Fig. 1 are within the wavenumber range of 4000 - 400 cm⁻¹. The spectra depict three major absorption bands, namely silicon dioxide, alumina and hydroxyl groups. The peaks at 1030, 1045 and 1049 cm⁻¹ are assigned to the stretching vibrations of the Si-O bond and the peak observed at 922 cm⁻¹ corresponds to the Al-Al-OH bonds. Peaks at 733, 750 and 752 cm⁻¹ indicate the presence of OH resulting from the expulsion of water and hydroxyl groups in clay minerals during calcination [7]. The differences in the peak intensities can be attributed to the interaction of Ni(II) ions with functional groups on the kaolin adsorbent surface [8].

3.2 Adsorption studies

Effect of adsorbent mass

The adsorbent mass plays a vital role in adsorption processes. It determines the percentage removal of metal ions and is calculated by:

$$\% \text{Ads} = \frac{c_i - c_f}{c_i} \quad (1)$$

where %Ads denotes the amount of Ni(II) ions removed, and c_i and c_f stand for the initial and final concentrations (ppm) of the Ni(II) ions, respectively. The percentage removal of Ni(II) ions increased from 76.31 to 89.04% when the adsorbent mass was increased from 0.5 to 2.5 g as shown in Fig. 2. As the adsorbent mass increases, more adsorption sites of nickel ions become available.

Effect of contact time on the uptake of nickel ions

The adsorption isotherm describes the adsorption pattern between the Ni(II) ions adsorbed on the kaolin clay and

Table 1: Chemical composition of the calcined kaolin sample

Components	SiO ₂	Al ₂ O ₃	TiO ₂	MgO	Fe ₂ O ₃	CaO	Cr ₂ O ₃	ZnO	Mn ₂ O ₃
Amount (wt %)	53.158	41.143	3.017	0.442	0.126	0.044	0.018	0.013	0.008

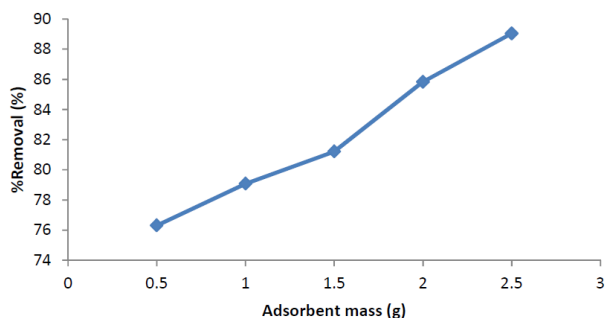


Figure 2: Effect of adsorbent mass on the removal of nickel ion

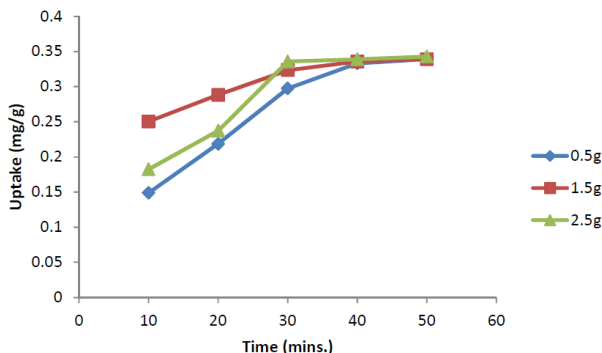


Figure 3: Effect of contact time on the uptake of nickel ions

the residual ions. The equilibrium uptake was determined using:

$$q_e = \frac{(c_i - c_e)V}{m} \tag{2}$$

where c_e denotes the equilibrium concentration, V stands for the volume of the solution and m represents the adsorbent mass.

Fig. 3 shows that the uptake of nickel ions is increased by increasing the contact time and reaches a maximum or saturation point after 30 to 40 mins., and thereafter the rate of adsorption remains almost constant even as the contact time and adsorbent mass are further increased.

The extent of the adsorption of nickel ions initially increased rapidly and then gradually until an equilibrium was attained. The high removal rate was due to the large surface area initially available for adsorption of Ni(II) ions but the capacity of the adsorbent was gradually exhausted over time since the occupation of the few vacant surface sites that remained was inhibited due to repulsive forces between the solute molecules in the solid and bulk phases [9]. As the adsorption sites on the surface become exhausted, the uptake rate is controlled by the rate at which the nickel ions are transported from the exterior to the interior sites of the adsorbent particles [10]. It was reported that during the adsorption of metal ions, initially the Ni(II) ions reach the boundary layer; then have to diffuse onto the surface of the adsorbent and finally, must diffuse into its porous structure. Therefore, this process requires a relatively longer contact time [11].

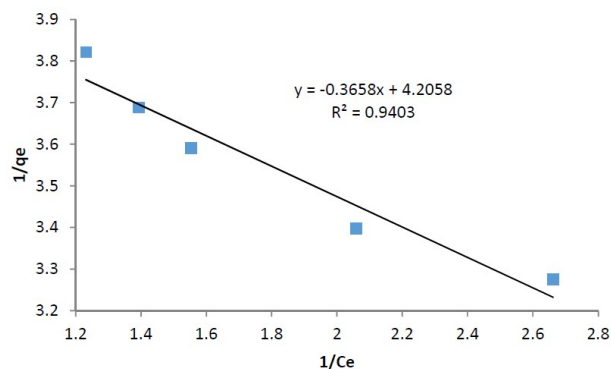


Figure 4: Langmuir isotherm for the adsorption of nickel ions

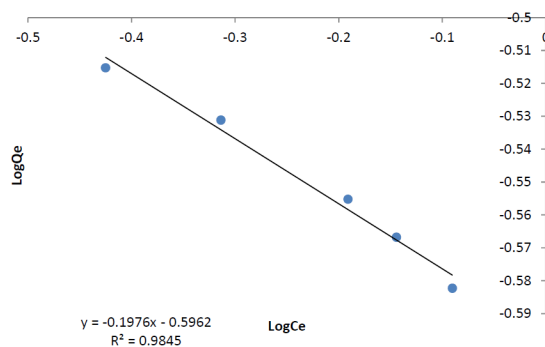


Figure 5: Freundlich isotherm for the adsorption of nickel ions

3.3 Equilibrium isotherms

The Langmuir and Freundlich models describe this isotherm:

$$\frac{1}{q_e} = \frac{1}{q_m} + \frac{1}{q_m b c_e} \tag{3}$$

and

$$\log q_e = \log K_F + \frac{1}{n} \log c_e, \tag{4}$$

where q_e denotes the uptake of Ni(II) ions adsorbed on the clay (mg/g), q_m and b stand for the single-layer adsorption capacity (mg/g) and the Langmuir equilibrium constant (L/mg), respectively, and K_F , n and b represent Freundlich adsorption constants.

The Langmuir and Freundlich constants shown in Table 2 were determined from the gradients and intercepts using the equations displayed in Figs. 4 and 5. The magnitudes of K_F and n are 0.2535 (mg/g)(L/mg)^{1/n} and -5.08 L/mg, respectively. The constant, n , is related to the ionic strength with regard to the adsorption of Ni(II) ions and K_F is related to both the ionic strength and amount of Ni(II) ions adsorbed. The significance of n is as follows: $n < 1$ (chemical process); $n = 1$ (linear process) and $n > 1$ (physical process). The negative value of n (-5.08 L/mg) obtained is indicative of chemical adsorption [12].

The Langmuir constant, b , shows the affinity of binding sites for nickel ions of the adsorbent. Similarly, the

Table 2: Parameters of Freundlich and Langmuir isotherm models

Freundlich Model		
n (L/mg)	K_F (mg/g)(L/mg) $^{1/n}$	R^2 (%)
-5.08	0.2535	98.40
Langmuir Model		
q_m (mg/g)	b (L/mg)	R^2 (%)
0.2378	-11.5210	94.00

Table 3: Pseudo-kinetics constants for the adsorption of nickel onto calcined kaolin

Pseudo-first order kinetics	Pseudo-second order kinetics
$K_1 = -0.0230$ (L/min)	$K_2 = 0.0073$ (mg/(mg/min))
$q_e = 1.127$ (mg/g)	$q_e = 5.291$ (mg/g)
$R^2 = 0.87$	$R^2 = 0.98$

negative value of b (-11.5210 L/mg) suggests a low degree of adsorption of Ni(II) ions by kaolin clay as is shown by the maximum adsorption capacity, q_m (0.2378 mg/g). The experimental data fitted well in the Freundlich model ($R^2 = 98.40\%$) indicating multilayer adsorption on the heterogeneous surface.

3.4 Adsorption kinetics

The kinetics data were determined using the linear equations of pseudo-first and second order kinetics:

$$\log(q_e - q_t) = \log q_e - \frac{1}{2.303} K_1 t \quad (5)$$

and

$$\frac{t}{q_t} = \frac{1}{K_2 q_e^2} + \frac{t}{q_e} \quad (6)$$

The parameters of adsorption kinetics are useful to predict the adsorption rate and provide considerable information to design and model the adsorption process as well as evaluate the adsorbent and operation control [13]. Figs. 6 and 7 showed pseudo-first and second order kinetics, respectively with regard to the adsorption of Ni(II) ions. The kinetics constants are summarized in Table 3.

The pseudo-first order kinetics exhibit a higher rate constant (K_1) and lower uptake (q_e). According to the values of R^2 in Table 3, it is clear that pseudo-second order kinetics fitted better to the adsorption data. This suggests the adsorption process is controlled by a chemisorption mechanism and the rate-limiting step is probably the surface adsorption of nickel ions [5].

3.5 Adsorption thermodynamics

The effect of temperature on the adsorption of nickel ions was investigated between 25 and 65 °C. The thermodynamic parameters determined from equations

$$K_c = \frac{q_e}{c_e} \quad (7)$$

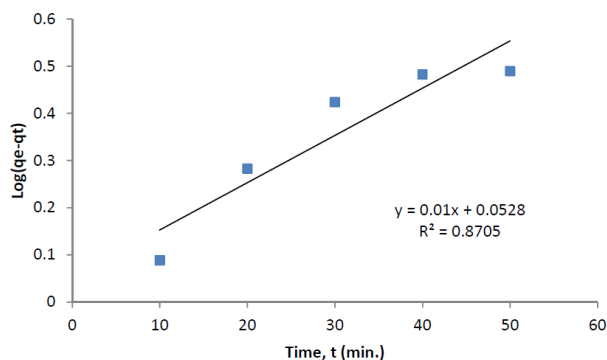


Figure 6: Pseudo-first order kinetics for the adsorption of nickel ions onto calcined kaolin clay

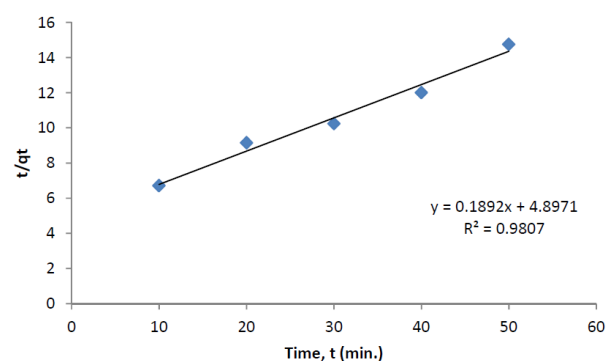


Figure 7: Pseudo-second order kinetics for the adsorption of nickel ions onto calcined kaolin clay

$$\Delta G^\circ = -RT \ln K_c \quad (8)$$

$$\ln K_c = -\frac{\Delta H^\circ}{RT} + \frac{\Delta S^\circ}{R} \quad (9)$$

$$\Delta G^\circ = \Delta H^\circ - T\Delta S^\circ \quad (10)$$

include changes in Gibbs free energy (ΔG°), enthalpy (ΔH°) and entropy (ΔS°). Fig. 8 depicts the Van't Hoff plots used to evaluate the thermodynamic parameters summarized in Table 4. The negative values of ΔG° confirm that the adsorption process is feasible and spontaneous while the positive values of ΔH° show that the adsorption process of Ni(II) ions is endothermic.

ΔH° can indicate the type of adsorption process involved. If ΔH° of the adsorbent exceeds 40 or is less than 20 kJ/mol, chemisorption or adsorption that is physical in nature occurs, respectively [8]. The positive values of ΔH° and ΔS° obtained show that the adsorption process is physical in nature and the solid-aqueous solution interface becomes more irregular and random during the adsorption of Ni(II) ions by the calcined kaolin adsorbent.

4. Conclusions

Thermally activated kaolin clay as an adsorbent was successfully prepared by calcination and used to remove

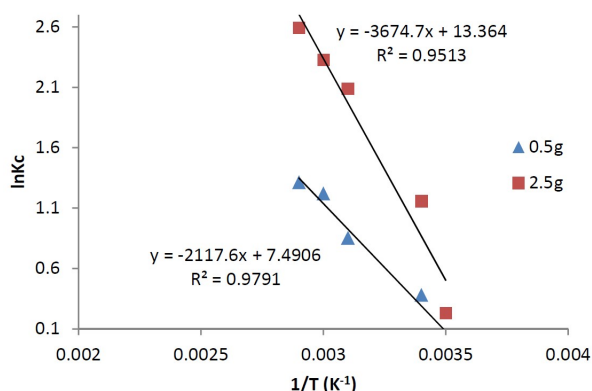


Figure 8: Effect of temperature with regard to the adsorption of nickel (II) ions on calcined kaolin

Table 4: Thermodynamic parameters for the adsorption of nickel (II) ions onto calcined kaolin at 25 °C

Adsorbent mass (g)	ΔG° (J/mol)	ΔS° (J/mol K)	ΔH° (J/mol)	R^2
0.5	-875.26	62.27	17600.74	0.979
2.5	-2553.22	111.07	30545.64	0.951

nickel ions from wastewater produced by a petroleum refinery. Adsorption isotherms, kinetics and thermodynamics were also studied. It was discovered that the adsorbent mass, contact time and temperature significantly influenced the adsorption of nickel ions onto the calcined kaolin adsorbent. The removal efficiency was increased by increasing the adsorbent mass, contact time and temperature. The adsorption data were described well by a Freundlich isotherm and pseudo-second order kinetics fitted well to the adsorption process. The negative values of ΔG° indicated that the adsorption of nickel ions was feasible and spontaneous. The positive values of ΔH° showed that the process was endothermic and irreversible. Generally speaking, the results revealed that calcined kaolin is a potential adsorbent for the treatment of wastewater laden with nickel ions produced by petroleum refineries.

REFERENCES

[1] Padmavathy, K. S.; Madhu, G.; Haseena, P. V.: A study on effects of pH, adsorbent dosage, time, initial concentration and adsorption isotherm study for the removal of hexavalent chromium (Cr(VI)) from wastewater by magnetite nanoparticles. *Procedia Technol.*, 2016, **24**, 585–594 DOI: 10.1016/j.protcy.2016.05.127

[2] Zubir, M. H. M.; Zaini, A. A. M.: Twigs-derived activated carbons via $H_3PO_4/ZnCl_2$ composite activation for methylene blue and congo red dyes removal. *Sci. Rep.*, 2020, **10**(1), 14050 DOI: 10.1038/s41598-020-71034-6

[3] Es-sabbany, H.; Berradi, M.; Nkhili, S.; Hsissou, R.; Allaoui, M.; Loutfi M.; Bassir, D.; Belfaquir, M;

El Youbi, S. M.: Removal of heavy metals (nickel) contained in wastewater-models by the adsorption technique on natural clay. *Mater. Today: Proc.*, 2019, **13**(3), 866–875 DOI: 10.1016/j.matpr.2019.04.050

[4] Alhawas, M.; Alwabel, M.; Ghoneim, A.; Alfarraj, A.; Sallam, A.: Removal of nickel from aqueous solution by low-cost clay adsorbents. *Proc. Int. Acad. Ecol. Env. Sci.*, 2013, **3**(2), 160–169 [http://www.iaees.org/publications/journals/piaees/articles/2013-3\(2\)/removal-of-nickel-from-aqueous-solution.pdf](http://www.iaees.org/publications/journals/piaees/articles/2013-3(2)/removal-of-nickel-from-aqueous-solution.pdf)

[5] Jock, A. A.; Muhammad, A. A. Z.; Abdulsalam, S.; El-Nafaty, U. A.; Aroke, U. O.: Insight into kinetics and thermodynamics properties of multicomponent lead(II), cadmium(II) and manganese(II) adsorption onto Dijah-Monkin bentonite clay. *Part. Sci. Technol.*, 2018, **36**(5), 569–577 DOI: 10.1080/02726351.2016.1276499

[6] Jongs, S. L.; Jock, A. A.; Ekanem, E. O.; Jauro, A.: Statistical analysis on physico-chemical properties of some Nigerian clay deposits. *J. Mat. Sci. Chem. Eng.*, 2019, **7**(8), 52–63 DOI: 10.4236/msce.2019.78007

[7] Jock, A. A.; Muhammad, A. A. Z.; Abdulsalam, S.; El-Nafaty, U. A.; Aroke, U. O.: Physicochemical characteristics of surface modified Dijah-Monkin bentonite. *Part. Sci. Technol.*, 2016, **36**(3), 287–297 DOI: 10.1080/02726351.2016.1245689

[8] Gorzin, F.; Abadi, M. M. B. R.: Adsorption of Cr(VI) from aqueous solution by adsorbent prepared from paper mill sludge: Kinetics and thermodynamics studies. *Adsorp. Sci. Technol.*, 2018, **36**(1-2), 149–169 DOI: 10.1177/0263617416686976

[9] Kumar, P. S.; Sivaprakash, S.; Jayakumar, N.: Removal of methylene blue dye from aqueous solutions using Lagerstroemia indica seed (LIS) activated carbon. *Int. J. Mat. Sci.*, 2017, **12**(1), 107–116 https://www.ripublication.com/ijoms17/ijomsv12n1_12.pdf

[10] Alzaydien, A. S.: Adsorption behavior of methyl orange onto wheat bran: Role of surface and pH. *Orient. J. Chem.*, 2015, **31**(2), 643–651 DOI: 10.13005/ojc/310205

[11] Khodaie, M.; Ghasemi, N.; Moradi, B.; Rahimi, M.: Removal of methylene blue from wastewater by adsorption onto $ZnCl_2$ activated corn husk carbon equilibrium studies. *J. Chem.*, 2013, **2013**, 1–6 DOI: 10.1155/2013/383985

[12] Marrakchi, F.; Hameed, B. H.; Hummadi, E. H.: Mesoporous biohybrid epichlorohydrin crosslinked chitosan/carbon-clay adsorbent for effective cationic and anionic dyes adsorption. *Int. J. Biol. Macromol.*, 2010, **163**, 1079–1086 DOI: 10.1016/j.ijbiomac.2020.07.032

[13] Deniz, F.: Adsorption properties of low-cost biomaterial derived from *Prunus amygdalus* L. for dye removal from water. *Sci. World J.*, 2013, **2013**, 1–8 DOI: 10.1155/2013/961671

CONSIDERATIONS TO APPROACH MEMBRANE BIOFOULING IN MICROBIAL FUEL CELLS

SZABOLCS SZAKÁCS *¹ AND PÉTER BAKONYI¹

¹Research Institute on Bioengineering, Membrane Technology and Energetics, University of Pannonia, Egyetem u. 10, 8200 Veszprém, HUNGARY

Among bioelectrochemical systems, those referred to as microbial fuel cells (MFCs) are widely implemented for wastewater management and simultaneous recovery of electrical energy. MFCs are fundamentally assisted by bacterial populations, mostly mixed cultures to be more exact that, after oxidizing the substrate, are capable of facilitating the passage of electrons to an electron acceptor, usually the anode. However, certain undesired bacterial strains often colonize not only the electrode but the membrane separator over time and cause severe biofouling. The membrane is an architectural element of many MFCs and determines the efficiency of the system. In this paper, this issue is overviewed briefly and some considerations concerning how to approach the problem are presented.

Keywords: microbial fuel cell, membrane, oxygen mass transfer, biofouling

1. Introduction

Bioelectrochemical systems, including Microbial Fuel Cells (MFCs), are often installed with a physical separator such as a membrane as illustrated in Fig. 1 [1].

The membrane, which separates the anode from the cathode, should enable the adequate migration of ions (in this case, cations such as protons) between the electrodes to ensure the MFC continues to produce electricity [2]. Furthermore, the membrane should function as a barrier against the crossover effect of substances to avoid the loss of the substrate (which normally is injected into the anode chamber in order to feed the species of electroactive bacteria shown in Table 1 living on a biofilm on the electrically-conductive anode surface) and penetration of dissolved oxygen from the aerated cathode chamber to the anaerobic anode chamber [3].

In addition to these requirements which are associated with the physical and chemical properties of the material, the membranes should be relatively affordable. Another point that needs to be addressed is the stability of the membrane, which can be influenced by the complex chemical environment of the bulk phases (anolyte in the anode chamber, catholyte in the cathode chamber) in an MFC and microbiological phenomena [5]. Altogether, these effects may cause fouling of the membrane during its operation, moreover, when the underlying mechanism is associated with the metabolism and/or growth of microorganisms, the term “biofouling” is more appropriate [6]. In summary, various membranes can be evaluated

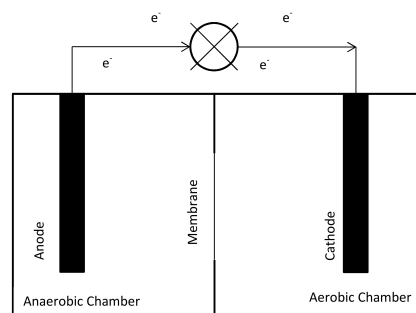


Figure 1: Scheme of an MFC

and ranked based on the characteristics of the membrane materials (typically but not exclusively fabricated from polymers) and their observed behavior during MFC operation which can be monitored by various electrochemical measurements, e.g., recording the cell voltage, as presented in Fig. 2.

2. Membranes and biofouling in MFCs – The potential role of oxygen mass transfer

In accordance with the previous section, the membrane separator divides the anaerobic anode chamber from the aerobic cathode chamber [7]. Therefore, it is reasonable to assume that the actual microbial communities developing on the anode and the membrane have completely different structures and relationships with gaseous oxygen. From the literature, it can be concluded with a good degree of certainty that the electrochemically active bacteria

*Correspondence: szakacs.szabolcs@mk.uni-pannon.hu

Table 1: Electroactive species of bacteria and their oxygen tolerance [4]

Species	Oxygen tolerance
<i>E. coli</i>	facultatively anaerobic https://bacdiv.dsmz.de/strain/4907
<i>Shewanella oneidensis</i>	facultatively anaerobic https://img.jgi.doe.gov/cgi-bin/m/main.cgi?section=TaxonDetail&page=taxonDetail&taxon_oid=637000258
<i>Geobacter sulfurreducens</i>	strict anaerobe https://bacdiv.dsmz.de/strain/5792
<i>Geobacter metallireducens</i>	strict anaerobe https://bacdiv.dsmz.de/strain/5791
<i>Desulfobulbus propionicus</i>	strict anaerobe https://bacdiv.dsmz.de/strain/4004
<i>Geothrix fermentans</i>	strict anaerobe https://bacdiv.dsmz.de/strain/17672
<i>Paracoccus pantotrophus</i>	facultatively anaerobic https://bacdiv.dsmz.de/strain/13703
<i>Rhodospseudomonas palustris DX-1</i>	strict anaerobe https://bacdiv.dsmz.de/strain/1819

on the anode are either strict or facultative anaerobes as shown in Table 1 [4]. However, a considerable knowledge gap seems to exist concerning the populations attached to the surface of the membrane and the occurrence of bio-fouling. In contrast, it is reasonable to suppose that these membrane-bound colonies and biofilms are more tolerant of dissolved oxygen due to the technically direct and long-lasting contact with this substance. In general, the oxygen flux across a membrane in MFCs is described by the oxygen transfer coefficient which can be calculated by [8,9]

$$k_{\text{O}} = -\frac{V}{At} \ln \left[\frac{(C_0 - C)}{C_0} \right] \quad (1)$$

where k_{O} denotes the oxygen transfer coefficient ($\text{cm}^3/\text{cm}^2\text{s}$), V stands for the volume of liquid (cm^3), A represents the surface area of the membrane (cm^2), C_0 refers to the saturation oxygen concentration (mol/dm^3), C is the actual oxygen concentration measured (mol/dm^3) and t denotes the time of the measurement (s); and

$$k_{\text{O}} = \frac{D_{\text{O}}}{L} \quad (2)$$

where D_{O} stands for the oxygen diffusion coefficient (cm^2/s) and L represents the thickness of the membrane (cm).

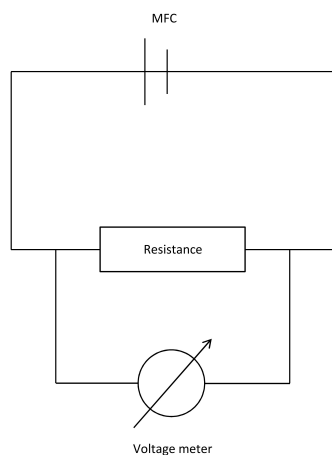


Figure 2: Schematic diagram of the MFC

Therefore, it is worth examining which strains colonize the membrane and how these mixed communities vary depending on k_{O} . Even though some previous papers have demonstrated the use of various microscopic imaging techniques based on visual observations to study these biofouling layers on the surface of membranes [10–12], qualitative and quantitative feedback to highlight “what type of” and “how many” microbes can coexist is scarce. As a result, experimental methodology involving the apparatus of modern molecular biology, e.g. DNA-based identification, should be encouraged and implemented to answer such questions [13].

3. Conclusions

The capability of membranes to permeate dissolved oxygen in microbial fuel cells is key. On the one hand, reduced oxygen transport membranes (OTMs) are likely to maintain the typically less oxygen tolerant, electroactive bacteria located on the surface of the anode in a good condition. On the other hand, oxygen mass transfer through the membrane is expected to affect the biofouling of the separator and thus, how microbial communities respond to changes in material properties, in particular k_{O} , needs to be understood. The assessment of membranes with different values of k_{O} should be carried out relative to Nafion, which is by far the most broadly employed polymer for benchmarking studies [14].

Acknowledgement

This work was supported by the National Research, Development and Innovation Office (NKFIH, Hungary) under grant number FK 131409 and GINOP-2.3.2-15-2016-00016 Excellence of strategic R+D workshops, entitled “Development of modular, mobile water treatment systems and waste water treatment technologies based on University of Pannonia to enhance growing dynamic export of Hungary” (2016-2020)

REFERENCES

- [1] Leong, J. X.; Daud, W. R. W.; Ghasemi, M.; Liew, K. B.; Ismail, M.: Ion exchange membranes separators in microbial fuel cells for bioenergy conversion: A comprehensive review. *Renew. Sustain. Energy Rev.*, 2013, **28**, 575–587 DOI: [10.1016/j.rser.2013.08.052](https://doi.org/10.1016/j.rser.2013.08.052)
- [2] Daud, S. M.; Kim, B. H.; Ghasemi, M.; Daud, W. R. W.: Separators used in microbial electrochemical technologies: Current status and future prospects. *Bioresour. Technol.*, 2015, **195**, 170–179 DOI: [10.1016/j.biortech.2015.06.105](https://doi.org/10.1016/j.biortech.2015.06.105)
- [3] Bakonyi, P.; Koók, L.; Kumar, G.; Tóth, G.; Rózsenszki, T.; Nguyen, D. D.; Chang, S. W.; Zhen, G.; Bélafi-Bakó, K.; Nemestóthy, N.: Architectural engineering of bioelectrochemical systems from the perspective of polymeric membrane separators: A comprehensive update on recent progress and future prospects. *J. Memb. Sci.*, 2018, **564**, 508–522 DOI: [10.1016/j.memsci.2018.07.051](https://doi.org/10.1016/j.memsci.2018.07.051)
- [4] Sharma, V.; Kundu, P. P.: Biocatalysts in microbial fuel cells. *Enzyme Microb. Technol.*, 2010, **47**(5), 179–188 DOI: [10.1016/j.enzmictec.2010.07.001](https://doi.org/10.1016/j.enzmictec.2010.07.001)
- [5] Koók, L.; Bakonyi, P.; Harnisch, F.; Kretzschmar, J.; Chae, K.-J.; Zhen, G.; Kumar, G.; Rózsenszki, T.; Tóth, G.; Nemestóthy, N.; Bélafi-Bakó, K.: Biofouling of membranes in microbial electrochemical technologies: Causes, characterization methods and mitigation strategies. *Bioresour. Technol.*, 2019, **279**, 327–338 DOI: [10.1016/j.biortech.2019.02.001](https://doi.org/10.1016/j.biortech.2019.02.001)
- [6] Noori, Md. T.; Ghangrekar, M. M.; Mukherjee, C. K.; Min, B.: Biofouling effects on the performance of microbial fuel cells and recent advances in biotechnological and chemical strategies for mitigation. *Biotechnol. Adv.*, 2019, **37**(8), 107420 DOI: [10.1016/j.biotechadv.2019.107420](https://doi.org/10.1016/j.biotechadv.2019.107420)
- [7] Patil, S. A.; Gildemyn, S.; Pant, D.; Zengler, K.; Logan, B. E.; Rabaey, K.: A logical data representation framework for electricity-driven bioproduction processes. *Biotechnol. Adv.*, 2015, **33**(6), 736–744 DOI: [10.1016/j.biotechadv.2015.03.002](https://doi.org/10.1016/j.biotechadv.2015.03.002)
- [8] Chae, K. J.; Choi, M.; Ajayi, F. F.; Park, W.; Chang, I. S.; Kim, I. S.: Mass transport through a proton exchange membrane (Nafion) in microbial fuel cells. *Energy and Fuels*, 2008, **22**(1), 169–176 DOI: [10.1021/ef700308u](https://doi.org/10.1021/ef700308u)
- [9] Kim, J. R.; Cheng, S.; Oh, S.-E.; Logan, B. E.: Power generation using different cation, anion, and ultrafiltration membranes in microbial fuel cells. *Environ. Sci. Technol.*, 2007, **41**(3), 1004–1009 DOI: [10.1021/es062202m](https://doi.org/10.1021/es062202m)
- [10] Venkatesan, P. N.; Dharmalingam, S.: Effect of cation transport of SPEEK - Rutile TiO₂ electrolyte on microbial fuel cell performance. *J. Memb. Sci.*, 2015, **492**, 518–527 DOI: [10.1016/j.memsci.2015.06.025](https://doi.org/10.1016/j.memsci.2015.06.025)
- [11] Angioni, S.; Millia, L.; Bruni, G.; Tealdi, C.; Mustarelli, P.; Quartarone, E.: Improving the performances of NafionTM-based membranes for microbial fuel cells with silica-based, organically-functionalized mesostructured fillers. *J. Power Sources*, 2016, **334**, 120–127 DOI: [10.1016/j.jpowsour.2016.10.014](https://doi.org/10.1016/j.jpowsour.2016.10.014)
- [12] Mokhtarian, N.; Ghasemi, M.; Daud, W. W. R.; Ismail, M.; Najafpour, G.; Alam, J.: Improvement of microbial fuel cell performance by using nafion polyaniline composite membranes as a separator. *J. Fuel Cell Sci. Technol.*, 2013, **10**(4), 041008 DOI: [10.1115/1.4024866](https://doi.org/10.1115/1.4024866)
- [13] Saratale, R. G.; Saratale, G. D.; Pugazhendhi, A.; Zhen, G.; Kumar, G.; Kadier, A.; Sivagurunathan, P.: Microbiome involved in microbial electrochemical systems (MESs): A review. *Chemosphere*, 2017, **177**, 176–188 DOI: [10.1016/j.chemosphere.2017.02.143](https://doi.org/10.1016/j.chemosphere.2017.02.143)
- [14] Rahimnejad, M.; Bakeri, G.; Ghasemi, M.; Zirepour, A.: A review on the role of proton exchange membrane on the performance of microbial fuel cell. *Polym. Adv. Technol.*, 2014, **25**(12), 1426–1432 DOI: [10.1002/pat.3383](https://doi.org/10.1002/pat.3383)

NEW CHAINING CRITERIA IN DIPOLAR FLUIDS BASED ON MONTE CARLO SIMULATIONS

SÁNDOR NAGY ^{*1,2}

¹Berzsenyi Dániel Teacher Training Centre, Eötvös Loránd University, Károlyi Gáspár tér 4. A-building, 9700 Szombathely, HUNGARY

²Institute of Mechatronics Engineering and Research, University of Pannonia, Gasparich Márk u. 18/A, 8900 Zalaegerszeg, HUNGARY

A new energy-based chaining criterion was introduced in dipolar systems based on an earlier article by the author, in which the probability of chaining for adjacent particles in a new formula of magnetic susceptibility was used. The probability of chaining and the magnitude of the energy criterion can be calculated from the Monte Carlo (MC) simulation values of magnetic susceptibility. The energy criterion also depends on the dipole moment and the density. At high densities, the energy criterion is well below 70–75%. In addition, it was confirmed by simulation results that the chain length distribution follows a geometric distribution. How the probability of chaining depends on the energy criterion was given empirically and two parameters were fitted to it.

Keywords: dipolar fluids, chain formation, energy criterion

1. Introduction

According to the literature, the criterion of chaining in dipolar systems is unclear. Usually, an energy criterion is used to decide whether two adjacent particles form part of a chain. The energy criterion defines the limit at a certain level of interaction energy between them, which is usually 70 – 75% of the minimum pair interaction energy [1–4]. According to another definition, if the pair interaction energy is negative and the two particles are closer together than 1.3 in diameter unit, then chaining occurs [5, 6]. The problem with this is that the minimum pair interaction energy depends on the magnitude of the dipole moment, so an identical amount of pair interaction energy between two adjacent particles indicates chaining in one case but not in the other. In another article, the author examined [7] the probability density function of pair interaction energies in a dipolar hard sphere (DHS) system and found that no unit jump-like change in the frequency of the pair interaction energy would justify the introduction of a general criterion based on the pair interaction energy. Furthermore, such a general definition does not take into account the effect of density, while it can be assumed that chaining occurs at different densities and different energy levels of the same dipole moments. Therefore, this study seeks to determine the magnitude of the energy criterion from another source, that is, a real, measurable, physical parameter. The physical parameter

in this case is magnetic susceptibility.

In a previous article [8], the author stated that the chain length distribution in dipolar fluids follows a geometric distribution. If the probability that two adjacent particles form a chain is denoted by p , it can be deduced that the chain length distribution is

$$g_k = (1 - p) p^{k-1}, \quad (1)$$

where k stands for the chain length. The particle size distribution, which yields the proportion of particles in exactly k -long chains is

$$h_k = (1 - p)^2 k p^{k-1}. \quad (2)$$

The average chain length is derived from the properties of the geometric distribution: $1/(1 - p)$. Assuming that a chain of length k behaves as if its dipole moment is km , its initial magnetic susceptibility can be deduced (in c.g.s. units) as

$$\chi_0 = \frac{1 + p}{1 - p} \chi_L \left(1 + \frac{4\pi}{3} \chi_L \right), \quad (3)$$

where χ_L denotes Langevin susceptibility [9],

$$\chi_L = \frac{\rho m^2}{3k_B T}, \quad (4)$$

ρ stands for the density, T represents the temperature, and k_B refers to the Boltzmann constant. In Eq. 3, the expression

$$\chi_P = \chi_L \left(1 + \frac{4\pi}{3} \chi_L \right) \quad (5)$$

*Correspondence: sata123.sandor@gmail.com

calculates the initial magnetic susceptibility from Pshenichnikov's theory [10]. Eq. 3 can be used to determine the value of p at a given density and dipole moment, since χ_0 can be determined from simulations and χ_P can be calculated exactly from

$$p = \frac{\chi_0 - \chi_P}{\chi_0 + \chi_P}. \quad (6)$$

If the occurrence of chaining is linked to an energy criterion, it is clear that the value of p depends on the magnitude of the energy criterion. Thus, if the correct value of p is known from Eq. 6, the magnitude of the correct energy criterion can be obtained from the relationship $p - U_{\text{lim}}$. The structure of the results is as follows: firstly, through several examples, it is shown that for any energy criterion, the number of chains follows a geometric distribution; secondly, the p values calculated from the magnetic susceptibility values are given; thirdly, from simulations, the U_{lim} values are determined that provide the desired p value at a given density and dipole moment; finally, by fitting, an empirical formula is derived to describe the relationship $p - U_{\text{lim}}$.

2. Simulations and results

Monte Carlo simulations of DHS fluids were performed using a canonical NVT ensemble. Boltzmann sampling [11], periodic boundary conditions and the minimum-image convention were applied. In order to take into account the long-range character of the dipolar interaction, the reaction field method under periodic boundary conditions of conduction was used. After 100,000 equilibration periods, 1,000,000 production cycles were conducted involving $N = 1,000$ particles. The reduced density was calculated by $\rho^* = \rho\sigma^3$ and the reduced dipole moment by $m^* = m/\sqrt{\sigma^3 k_B T}$, where σ denotes the diameter of the particles. The pair interaction energy between two particles in a DHS system is determined only by the dipolar energy:

$$U_{ij}^{\text{dd}} = -\frac{m^2}{r_{ij}^3} [3(\hat{\mathbf{m}}_i \cdot \hat{\mathbf{r}}_{ij})(\hat{\mathbf{m}}_j \cdot \hat{\mathbf{r}}_{ij}) - (\hat{\mathbf{m}}_i \cdot \hat{\mathbf{m}}_j)], \quad (7)$$

where the particles have dipole moments of strength m of an orientation given by unit vector $\hat{\mathbf{m}}$, moreover, the distance between the centers of the particles is denoted by r_{ij} and $\hat{\mathbf{r}}_{ij} = \mathbf{r}_{ij}/r_{ij}$. The dots symbolize the scalar product. The lowest and most favorable energy value was determined by $U_{\text{min}}^{\text{dd}} = -2m^2/\sigma^3$. The magnitude of the energy criterion (u) was given in the usual way in proportion to this: $u = U^{\text{dd}}/U_{\text{min}}^{\text{dd}}$.

To determine the chain length distribution (g_k), the number of chains of a given length was counted in each cycle. This required a predefined energy criterion. Rearranging Eq. 1 leads to the chain length distribution:

$$\lg(g_k) = \lg(1-p) + (k-1)\lg(p). \quad (8)$$

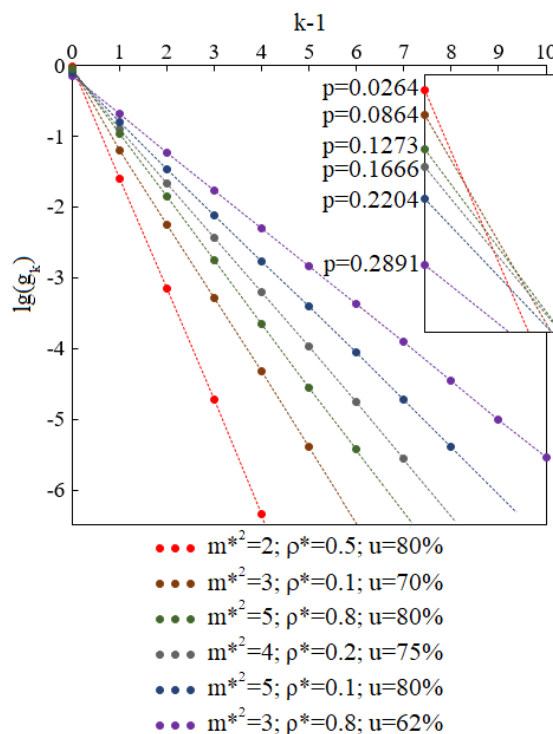


Figure 1: The logarithm of the chain length distribution as a function of chain length at six different dipole moments, densities and energy criteria. According to Eq. 8, the value of p (probability of chaining) is also derived from the gradient of the fitted lines as well as the intercept of the vertical axis.

From this, it can be seen that if the logarithm of the chain length distribution is plotted as a function of $k - 1$, the gradient of the fitted straight line yields the logarithm p , while the logarithm of the vertical intercept gives $1 - p$. Since in each case the resulting lines are linear, it follows that the chain length distribution does indeed follow a geometric distribution. Fig. 1 shows the simulation results for the chain length distribution obtained for six different combinations of dipole moments, densities and energy criteria. It can be seen that the fitted lines are linear on the logarithmic scale in all cases. It is clear from the inset graphs that the larger its gradient, the closer its intercept is to zero. The p values shown in Fig. 1 were derived from the gradient of the fitted lines.

Further results are summarized in Table 1. In the third column of Table 1, using the terms mentioned in the Introduction (Section 1), the values of p are given. The values of χ_P can be precisely calculated from Eq. 5. The values of χ_0 are derived from the simulations. (For the simulation results of χ_0 , reference [12] was used. The missing χ_0 data were supplemented with our own simulation results.)

This was followed by the determination of u_{lim} , also from our own simulations. According to Eq. 2, the number of particles that do not form a chain or, in other words, which form single-element chains is $h_1 = (1-p)^2$. Thus, in each step of the simulation, it was only nec-

Table 1: The probabilities of chaining (3rd column), the values of the energy criterion (4th column) according to the simulations and the values of the fitted curves (5th and 6th columns) according to Eq. 9

$(m^*)^2$	ρ^*	p	u_{lim}	A	B
2	0.1	0.0135	0.74	0.203	2.902
2	0.2	0.0209	0.76	0.358	2.864
2	0.3	0.0316	0.75	0.492	2.863
2	0.4	0.0231	0.80	0.623	2.881
2	0.5	0.0254	0.80	0.751	2.893
2	0.6	0.0387	0.78	0.885	2.901
2	0.7	0.0523	0.77	1.022	2.895
2	0.8	0.1674	0.66	1.167	2.874
2	0.9	0.2641	0.62	1.307	2.821
3	0.1	0.0802	0.68	0.426	2.284
3	0.2	0.0951	0.71	0.607	2.291
3	0.3	0.0772	0.75	0.732	2.333
3	0.4	0.0721	0.77	0.839	2.388
3	0.5	0.0762	0.77	0.943	2.442
3	0.6	0.0840	0.76	1.048	2.498
3	0.7	0.1889	0.67	1.154	2.535
3	0.8	0.3788	0.57	1.270	2.560
3	0.9	0.6745	0.45	1.383	2.547
4	0.1	0.2183	0.67	0.761	1.801
4	0.2	0.1777	0.73	0.900	1.842
4	0.3	0.1278	0.77	0.975	1.900
4	0.4	0.1174	0.78	1.044	1.989
4	0.5	0.1169	0.78	1.107	2.069
4	0.6	0.1818	0.72	1.180	2.159
4	0.7	0.4016	0.59	1.258	2.237
4	0.8	0.6814	0.46	1.341	2.295

essary to count how many particles have the minimum pair interaction energy (counted individually for the other particles) greater than the examined energy criterion. This greatly simplified the complexity of the simulations. Therefore, the value of p belonging to the given energy criterion was determined, and for each dipole moment and density, a function was generated to create a relationship between p and u_{lim} . Of these, four are shown in Fig. 2. The dashed lines indicate the u_{lim} values of the already defined p values of these functions.

The fourth column of Table 1 shows the u_{lim} values for each dipole moment, density and value of p which are also plotted in Fig. 3. (The uncertainty of the functions shown in Fig. 3 stems from the uncertainty of the magnetic susceptibilities. For dipole moments less than $(m^*)^2 = 2$, this new energy criterion cannot be examined precisely because the uncertainty in the magnetic susceptibility is too great.) It can be seen that the frequently mentioned 70 – 75% criterion is more or less valid, although it differs significantly from it at high densities. Interestingly, the energy criterion is higher at medium densities than at low densities. This may be because the

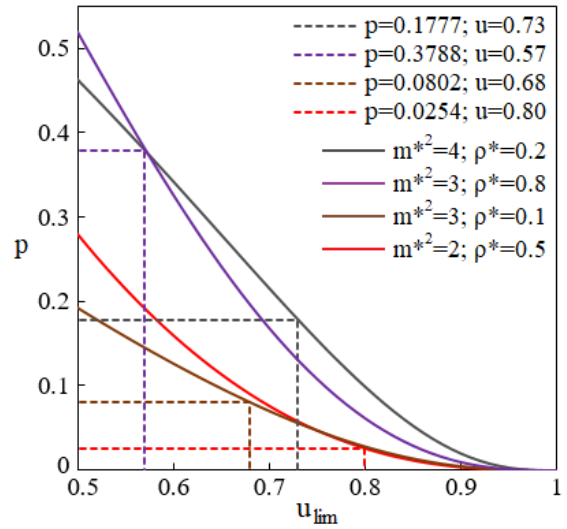


Figure 2: The probability of chaining as a function of the value of the energy criterion at four different dipole moments and densities. The dashed lines show the true values of p and thus u_{lim} as well.

chains are so close to each other at medium densities that they have an effect on each other, but do not at low densities. It is true that at high densities this effect is even stronger, but at the same time, the strength of the forces acting on the chain also increases.

In the following, the relationships between the $p - u_{lim}$ functions are specified by fitting. Four of these are shown in Fig. 2. In Fig. 4, for each of the three dipole moments examined, these functions are plotted at two densities. Since the functions are close to zero around $u_{lim} = 1$, the cosine function seems to be a good choice for describing the curves as follows:

$$p = A \cos^B \left(\frac{\pi}{2} u_{lim} \right) \quad (9)$$

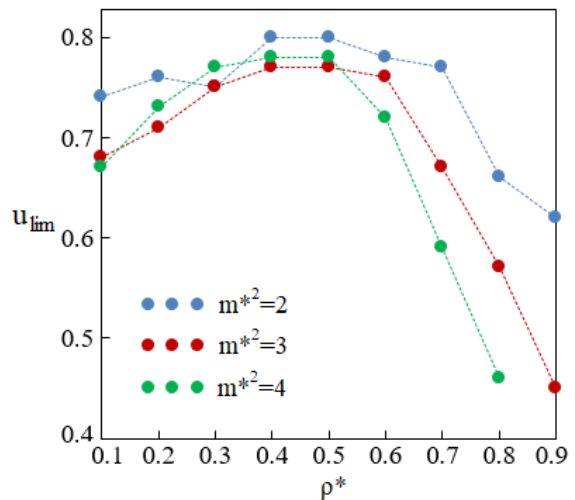


Figure 3: The values of u_{lim} as a function of the reduced density at three different dipole moments.

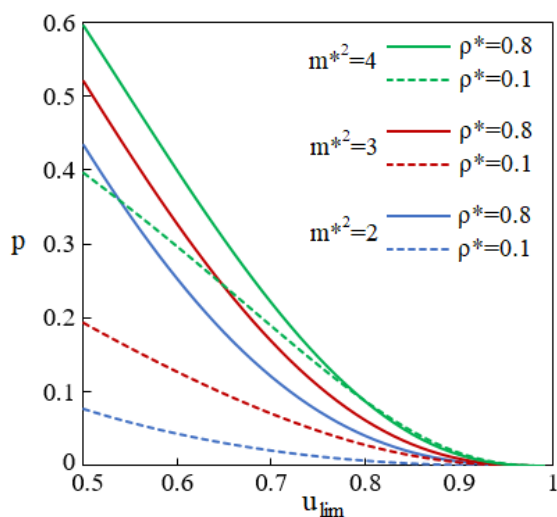


Figure 4: The probability of chaining as a function of the energy criterion at three different dipole moments. Dashed lines refer to low densities ($\rho^* = 0.1$), solid lines refer to high densities ($\rho^* = 0.8$). The lines of intermediate densities are between these two lines.

where A and B are constants and their magnitudes are given in the fifth and sixth columns of Table 1. Fits were made within the range $u_{lim} = 0.5 - 1$. The absolute error in the values of p is not greater than 0.01285 in all the cases examined.

3. Conclusion

The main result of this article is shown in Fig. 3. A well-explained energy-based chaining criterion resulting from magnetic susceptibility was defined. From the simulated values of magnetic susceptibility, the probability of chaining was calculated. From this, the magnitude of the chaining criterion was derived using simulations as well. Therefore, a well-explained theory was developed to define the chaining energy criterion, which produced different results for different values of density and dipole moment in DHS systems. The criterion value of 70–75% commonly given in the literature is only approximately true at low densities ($\rho^* \leq 0.3$). At medium densities ($0.3 < \rho^* < 0.6$), the values are generally higher, while at high densities ($\rho^* \geq 0.6$), they are much lower.

Acknowledgement

This research was supported by the European Union and co-financed by the European Social Fund under the project EFOP-3.6.2-16-2017-00002.

REFERENCES

- [1] Ivanov, A. O.; Wang, Z.; Holm, C.: Applying the chain formation model to magnetic properties of aggregated ferrofluids, *Phys. Rev. E*, 2004, **69**(3), 031206 DOI: [10.1103/PhysRevE.69.031206](https://doi.org/10.1103/PhysRevE.69.031206)
- [2] Wang, Z.; Holm, C.; Müller, H. W.: Molecular dynamics study on the equilibrium magnetization properties and structure of ferrofluids, *Phys. Rev. E*, 2002, **66**(2), 021405 DOI: [10.1103/PhysRevE.66.021405](https://doi.org/10.1103/PhysRevE.66.021405)
- [3] Valiskó, M.; Varga, T.; Baczoni, A.; Boda, D.: The structure of strongly dipolar hard sphere fluids with extended dipoles by Monte Carlo simulations, *Mol. Phys.*, 2010, **108**(1), 87–96 DOI: [10.1080/00268970903514553](https://doi.org/10.1080/00268970903514553)
- [4] Tavares, J. M.; Weis, J. J.; Telo da Gama, M. M.: Strongly dipolar fluids at low densities compared to living polymers, *Phys. Rev. E*, 1999, **59**(4), 4388–4395 DOI: [10.1103/PhysRevE.59.4388](https://doi.org/10.1103/PhysRevE.59.4388)
- [5] Kantorovich, S.; Ivanov, A. O.; Rovigatti, L.; Tavares, J. M.; Sciortino, F.: Nonmonotonic magnetic susceptibility of dipolar hard-spheres at low temperature and density, *Phys. Rev. Lett.*, 2013, **110**(14), 148306 DOI: [10.1103/PhysRevLett.110.148306](https://doi.org/10.1103/PhysRevLett.110.148306)
- [6] Rovigatti, L.; Russo, J.; Sciortino, F.: Structural properties of the dipolar hard-sphere fluid at low temperatures and densities, *Soft Matt.*, 2012, **8**(23), 6310–6319 DOI: [10.1039/C2SM25192B](https://doi.org/10.1039/C2SM25192B)
- [7] Nagy, S.: The frequency of the two lowest energies of interaction in dipolar hard sphere systems, *Anal. Tech. Szeged.*, 2020, **14**(2) in press
- [8] Nagy, S.: The initial magnetic susceptibility of dense aggregated dipolar fluids, *Hung. J. Ind. Chem.*, 2018, **46**(2), 47–54 DOI: [10.1515/hjic-2018-0018](https://doi.org/10.1515/hjic-2018-0018)
- [9] Langevin, P.: Sur la théorie du magnétisme, *J. Phys. Theor. Appl.*, 1905, **4**(1), 678–693 DOI: [10.1051/jphysap:019050040067800](https://doi.org/10.1051/jphysap:019050040067800)
- [10] Pshenichnikov, A. F.; Mekhonoshin, V. V.: Equilibrium magnetization and microstructure of the system of superparamagnetic interacting particles: numerical simulation, *J. Magn. Magn. Mater.*, 2000, **213**(3), 357–369 DOI: [10.1016/S0304-8853\(99\)00829-X](https://doi.org/10.1016/S0304-8853(99)00829-X)
- [11] Allen, M. P.; Tildesley, D. J.: Computer simulation of liquids (Clarendon Press, Oxford) 1987, ISBN: 978-0-198-55645-9
- [12] Theiss, M.; Gross, J.: Dipolar hard spheres: comprehensive data from Monte Carlo simulations, *J. Chem. Eng. Data*, 2019, **64**(2), 827–832 DOI: [10.1021/acs.jced.8b01169](https://doi.org/10.1021/acs.jced.8b01169)

TEMPERATURE AND ELECTRIC FIELD DEPENDENCE OF THE VISCOSITY OF ELECTORRHEOLOGICAL (ER) FLUIDS: WARMING UP OF AN ELECTORRHEOLOGICAL CLUTCH

SÁNDOR MESTER¹ AND ISTVÁN SZALAI *¹

¹Institute of Mechatronics Engineering and Research, University of Pannonia, Gasparich Márk u. 18/A, Zalaegerszeg, 8900, HUNGARY

Cognition of the temperature-dependence of intelligent fluids, e.g. electrorheological (ER) and magnetorheological (MR) fluids, is critical for their application. In this paper, the dependence of the viscosity of ER fluids on temperature and electric field strength is examined. A new correlation equation is presented to describe the dependence of the viscosity on temperature by extending the Andrade equation. Considering the dependence of viscosity on the electric field strength and temperature, that equation is used to model the warming up of an ER clutch.

Keywords: electrorheological fluid, viscosity, heat effect in ER fluids, ER clutch

1. Introduction

Electrorheological (ER) fluids are suspensions made by dispersing micron-sized solid particles with a relative permittivity of ε_p into a carrier fluid with a smaller relative permittivity of ε_f [1–3]. Normally, small concentrations of stabilizers are also used to avoid sedimentation. The structure and, therefore, the rheological properties are altered by applying an external electric field. The dispersed particles, guided by the electric field, form chain-like structures [4]. These structures impair the motion of the suspended particles resulting in an increase in the apparent viscosity. Using silicone oil as the carrier fluid is common, although other oils such as transformer oil have also been examined. The dispersed phase can consist of oxides, carbides, etc. ER and magnetorheological (MR) fluids are used in various applications, e.g. couplings, shock dampers, [5, 6] ultra-smooth polishing materials, etc. [7].

Most of the applications require the viscosity to be precisely adjusted, however, the viscosity alters as the temperature changes. [8,9] This disadvantage greatly limits its industrial use, as a change can impair fine-tuned systems by creating stern operating conditions. Apart from the need to measure the temperature, the dependence of the parameters of the ER fluids on temperature ought to be considered as well. In addition to the ER effect, an ER fluid is also affected by the thermal motion of particles. This motion works against the ER effect, as it disrupts the chain-like structure [10, 11].

2. Experimental

The dependence of the viscosity of fluids on the temperature is characterized by a law proposed by Andrade:

$$\eta = A e^{\frac{B}{T}}, \quad (1)$$

where η denotes the dynamic viscosity of the fluid, T stands for the temperature, while A and B represent characteristic constants of the fluid. The constants are experimentally defined for each fluid. For ER fluids, this equation is inadequate because their dependency on the electric field strength is not addressed. In the following chapters, the dependence on the electric field in Eq. 1 is introduced.

2.1 Samples and viscosity measurements

To study the thermal and field effects, an Anton Paar Physica MCR 301 rotational rheometer was used to measure the viscosity. Different measuring equipment can be used for MR and ER fluids, moreover, the samples can also be thermostated. The usage of a cylindrical probe is shown schematically in Fig. 1. The length of the probe was $L = 40.046$ mm, the radius of the probe was $r_i = 13.33$ mm and the inner radius of the chamber was $r_e = 14.46$ mm.

For the measurements, a self-prepared ER fluid was used. The carrier fluid was silicone oil with a viscosity of 1000 mPas at 298 K. The dispersed phase was silica powder of 0.5 – 10 μm in diameter (as the manufacturer

*Correspondence: szalai@almos.uni-pannon.hu

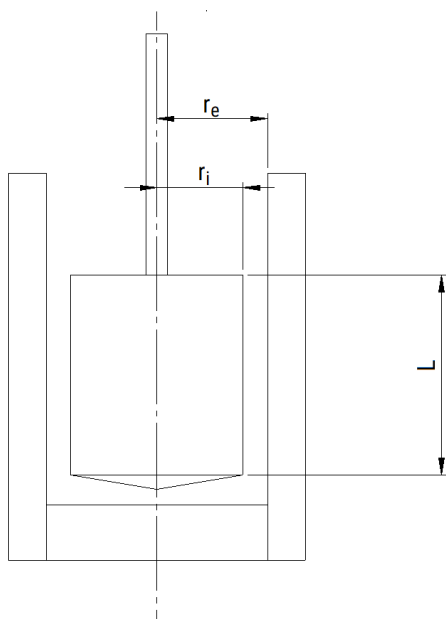


Figure 1: Schematic representation of the probe

claims that 80% of the particles have diameters of between 1 and 5 μm). As a result, three different concentrations of particles were investigated, namely 10, 20 and 30 wt%.

The samples were prepared through a multi-step procedure: after stirring by hand, the fluid was placed in an ultrasonic bath for 15 minutes to mix further. To ensure an air bubble-free ER fluid, the sample was exposed to a vacuum for 10 minutes before being placed in the rheometer.

The samples were measured at six different temperatures at increments of 10 K ranging from 293 K to 343 K. Considering the 1.13 mm gap at the measuring probe, the used voltages resulted in the following electrical field strengths: 0, 0.442, 0.885, 1.327 and 1.769 MV/m.

The samples were constantly stirred in the rheometer. A two-minute-long stirring cycle in the absence of an electric field came after setting the temperature. A ten-minute-long measuring cycle with an electric field was applied and another one-minute-long stirring cycle followed in the absence of an external electric field. The two mixing cycles at the beginning and end ensured that no residual particle arrangements from the previous measurements were present. The viscosity was measured per second.

3. Measurement Results and Analysis

3.1 Temperature dependence of the viscosity

As an example, the measurement results of an 30 wt% ER fluid at a temperature of 293 K are shown in Fig. 2: After an initial rise (while the chain-like structure was forming), the viscosity became roughly constant. The anomalies in the figure were caused by external interferences.

For the analysis, the results of a specific mixing ratio, electric field strength and temperature were averaged into

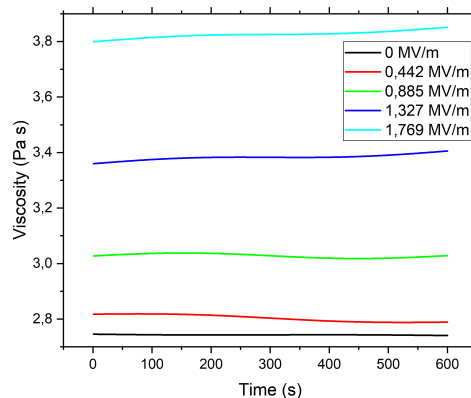


Figure 2: Viscosity measurements under various electric field strengths, $c = 30\%$, $T = 295\text{ K}$

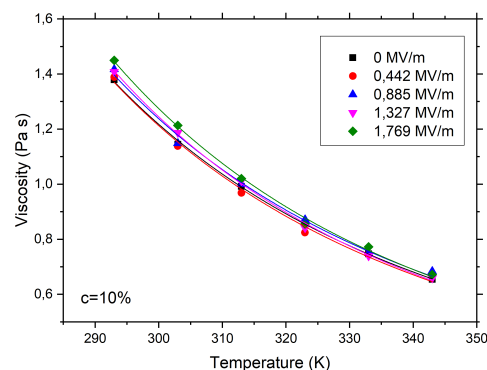


Figure 3: Experimental results and fitted curves (Eq. 2) of viscosity at $c = 10\%$ under various electric field strengths

a single value. The expected tendencies are as follows: as the electric field strength increases, so does the viscosity, while a rise in temperature is inversely proportional to the viscosity.

It was found that Eq. 1 is inappropriate for the exact representation of the dependence of ER viscosity data on temperature, therefore, in terms of the pre-exponential factor, a further temperature dependence was proposed:

$$\eta = (A_0 + A_1 T) e^{\frac{B}{T}}, \quad (2)$$

where A_0 , A_1 and B denote constants derived by fitting Eq. 2 to measurement data.

Figs. 3–5 demonstrate the fitted curves of the different concentrations of ER fluid. The extended formula (Eq. 2) correlates well with the measurements: the worst coefficient of determination for the fittings is $R^2 = 97.3\%$. Eq. 2 can be used to describe the viscosity of electrorheological fluids as a function of the temperature.

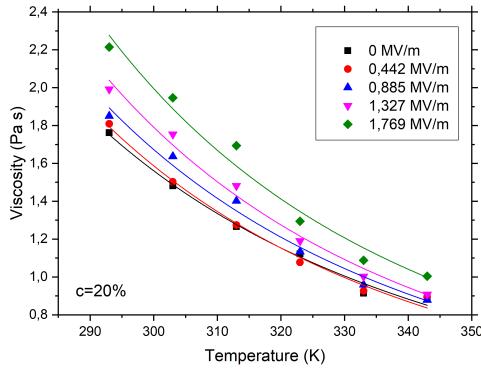


Figure 4: Experimental results and fitted curves (Eq. 2) of viscosity at $c = 20\%$ under various electric field strengths

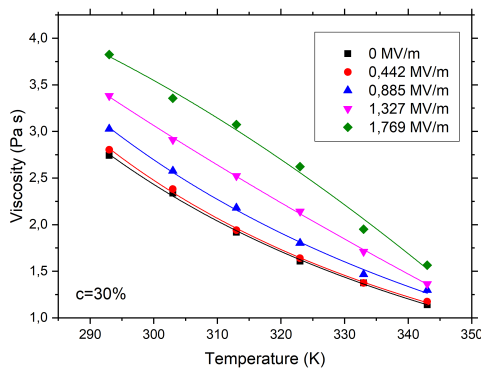


Figure 5: Experimental results and fitted curves (Eq. 2) of viscosity at $c = 30\%$ under various electric field strengths

3.2 Electric field strength dependence of viscosity

The introduced formula does not concern how the viscosity depends on the electric field strength. In the case of many practical applications, the electric field changes, therefore, the temperature-dependent description of viscosity alone is insufficient.

Eq. 2 can be extended by making the pre-exponential factor dependent on the electric field strength as well. This expansion is carried out via the square of the electric field, indicating that the direction of the field is reversible:

$$\eta = [A_0 + A_1 E^2 + (A_2 + A_3 E^2) T] e^{\frac{B}{T}} \quad (3)$$

where A_0 , A_1 , A_2 , A_3 and B denote constants, while E stands for the electric field strength.

Eq. 3 fitted to the measurement data can be seen in Figs. 6–8. Here the viscosity is represented as a function of the electric field strength and temperature. The coefficients of determination for the fittings are $R_{10\%}^2 = 99.62\%$, $R_{20\%}^2 = 98.62\%$ and $R_{30\%}^2 = 99.06\%$. Fitting parameters are summarized in Table 1.

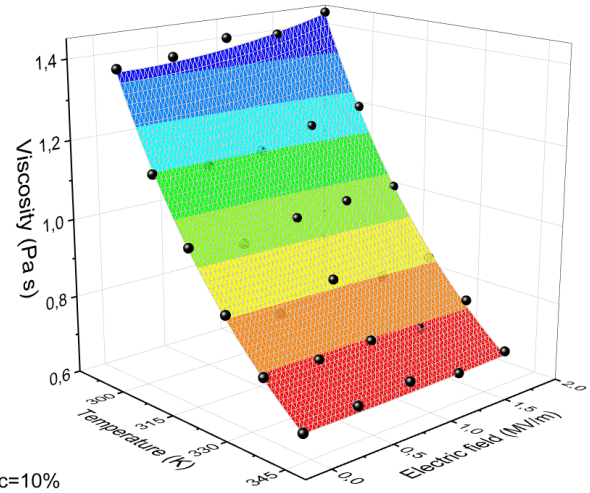


Figure 6: Viscosity measurement data (●) and the fitted surface (Eq. 3) at $c = 10\%$

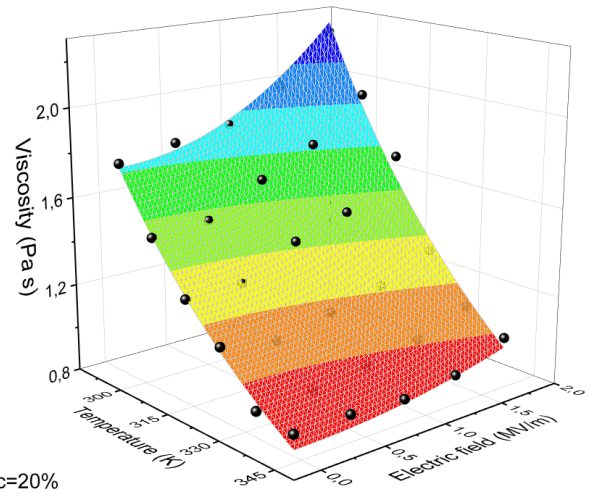


Figure 7: Viscosity measurement data (●) and the fitted surface (Eq. 3) at $c = 20\%$

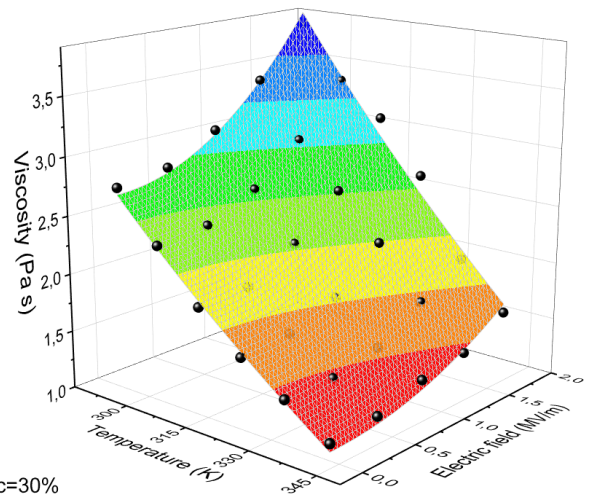


Figure 8: Viscosity measurement data (●) and the fitted surface (Eq. 3) at $c = 30\%$

Table 1: Fitted coefficients of Eq. 3 at different ER fluid concentrations

	Concentration [m/m]		
	10%	20%	30%
A_0	-2.17623E-4	0.12252	3.82564
A_1	2.47298E-16	2.2336E-14	5.10306E-13
A_2	9.7734E-6	-2.32975E-4	-9.89E-3
A_3	-6.84985E-19	-5.8753E-17	-1.2747E-15
B	1831.25188	1017.00608	3.82564

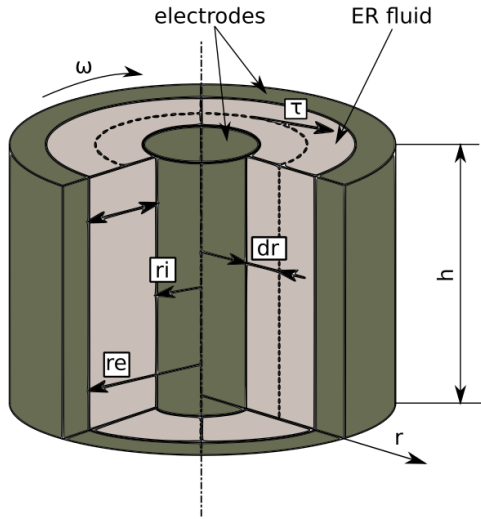


Figure 9: Cylindrical ER clutch model for the dissipation of viscous energy

4. Temperature rise in an ER clutch

4.1 ER clutch model

A schematic diagram of a simple cylindrical electro-rheological clutch is shown in Fig. 9. Nakamura et al. [12] described the temperature rise of similar clutches: their model consisted of several cylinders with gaps between them with radii from $r(i)$ to $r(i+1)$, where $i = 1, 2, \dots, n$ denotes the number of gaps which are filled with ER fluid with a viscosity of η . According to the model, assuming the clutch is insulated, the dissipation of the viscous energy per second in the gap i is

$$dE_i = \frac{\partial(\tau Ar\omega)}{\partial r} dr, \quad (4)$$

where A denotes the surface of the cylinder, τ stands for the shear stress and ω represents the rotational speed. By utilizing the attributes of the cylinders and integrating the formula, the following equation can be derived:

$$T(t + \Delta t) = \frac{1}{C} \left\{ \sum_{i=1}^n \frac{2\pi h \eta(T) \omega^2 r(i)^3}{s} \Delta t \right\} + T(t), \quad (5)$$

where T denotes the temperature, s stands for the gap, C represents the heat capacity of the fluid, ω refers to the relative rotational speed and h is the height of the cylinder.

In our system, only one gap is examined so Eq. 5 can be simplified to a differential equation:

$$\frac{dT}{dt} = \frac{2\pi h \omega^2 r^3}{sC} \eta(T). \quad (6)$$

4.2 Viscous energy dissipation in the clutch

Using the model of the ER clutch (Eq. 6), the viscous energy dissipation was calculated by inserting the formula of the viscosity (Eq.3):

$$\frac{1}{[A_0 + A_1 E^2 + (A_2 + A_3 E^2) T] e^{\frac{B}{T}}} dT = \frac{2\pi h \omega^2 r^3}{sC} dt. \quad (7)$$

The integration of the left-hand side of the equation can be solved numerically using mathematical software. Analytical integration requires the expansion of the exponential term into a Taylor series:

$$\begin{aligned} & \int \frac{e^{-\frac{B}{T}}}{[A_0 + A_1 E^2 + (A_2 + A_3 E^2) T]} dT = \\ & = \int \frac{1 - \frac{B}{T} + \frac{1}{2!} \frac{B^2}{T^2} - \frac{1}{3!} \frac{B^3}{T^3} + \dots}{[A_0 + A_1 E^2 + (A_2 + A_3 E^2) T]} dT \end{aligned} \quad (8)$$

Eq. 7 can be integrated following the expansion into a Taylor series resulting in the following expression:

$$\begin{aligned} & \int_{T_1}^{T_2} \frac{1}{[A_0 + A_1 E^2 + (A_2 + A_3 E^2) T] e^{\frac{B}{T}}} dT = \frac{(-1)^0 B^0}{0!} \frac{1}{a_0} \left[\frac{1}{c} \ln(1 + cT) \right]_{T_1}^{T_2} + \\ & + \frac{(-1)^1 B^1}{1!} \frac{1}{a_0} \left[c^{1-1} (-1)^1 \ln \frac{1 + cT}{T} \right]_{T_1}^{T_2} + \sum_{i=2}^{\infty} \frac{(-1)^i B^i}{i!} \frac{1}{a_0} \left[c^{i-1} (-1)^i \ln \frac{1 + cT}{T} + \sum_{j=2}^i \frac{(-1)^{i-j+1} c^{i-j}}{(j-1) T^{j-1}} \right]_{T_1}^{T_2}, \end{aligned} \quad (9)$$

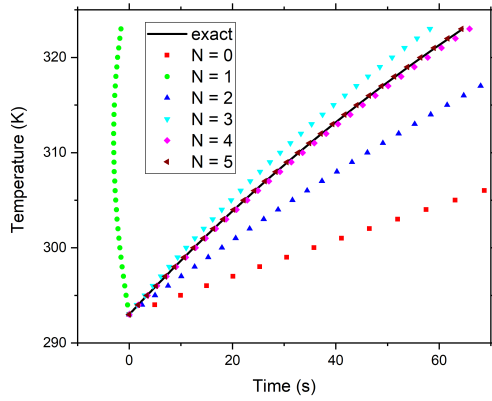


Figure 10: Heating of an ER clutch model as a function of the number of addends, $c = 30\%$, $E = 1.327$ MV/m and $T = 295$ K

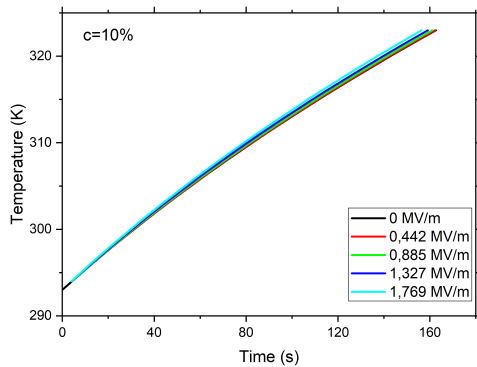


Figure 11: Heating of an ER clutch model over time, $c = 10\%$

$$\text{where } a_0 = A_0 + A_1 E^2 \text{ and } c = \frac{A_2 + A_3 E^2}{a_0}.$$

The expression in Eq. 9 can be used to calculate the time needed for the clutch to be heated to a given temperature. The closed formula, a double infinite sum, yields varying results depending on how many terms are used. In the present calculation, the following parameters are used: $h = 0.04$ m, $r = 0.0133$ m, $s = 0.0113$ m, $\omega = 4.057$ rad/s and $C = 0.05$ J/K.

The temperature as a function of the number of addends N is shown in Fig. 10. After the 5th addend, the numerical and analytical solutions are almost identical. To calculate the amount of heating, the physical properties of the Anton Paar probe and the calculated parameters (A_0 , A_1 , etc.) of the examined ER fluids were used.

Figs. 11–13 show the heating results using three different concentrations of ER fluids. As can be observed, as the electric field strength and concentration increase, the temperature also rises faster due to the internal friction.

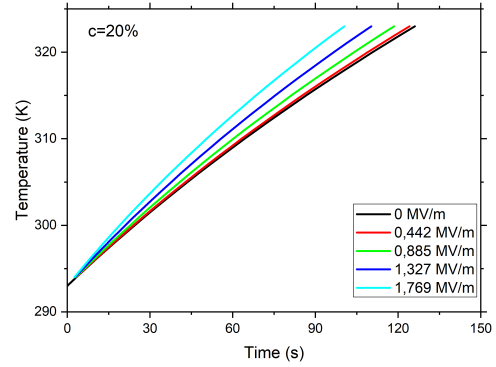


Figure 12: Heating of an ER clutch model over time, $c = 20\%$

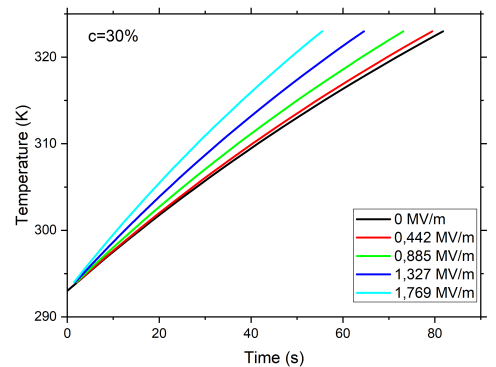


Figure 13: Heating of an ER clutch model over time, $c = 30\%$

5. Conclusion

In our paper, a new correlation equation was proposed to describe the dependence of the viscosity of ER fluids on temperature and electric field strength. The proposed equation describes the measurement results with a correspondingly small deviation. The temperature rise of the model system examined by using the aforementioned equations can also form the basis for the description of real systems. The applied model can be further refined, e.g. by taking into account the dependence of heat capacities on temperature.

Acknowledgement

This research was supported by the European Union and co-financed by the European Social Fund under project EFOP-3.6.2-16-2017-00002.

REFERENCES

- [1] Shin, K.; Kim, D.; Cho, J.-C.; Lim, H. S.; Kim, J. W.; Suh, K. D.: Monodisperse conducting colloidal dipoles with symmetric dimer structure for enhancing electrorheology properties, *J. Coll. Interf. Sci.*, 2012, **374**(1), 18–24 DOI: [10.1016/j.jcis.2012.01.055](https://doi.org/10.1016/j.jcis.2012.01.055)

- [2] Wu, J.; Xu, G.; Cheng, Y.; Liu, F.; Guo, J.; Cui, P.: The influence of high dielectric constant core on the activity of core-shell structure electrorheological fluid, *J. Coll. Interf. Sci.*, 2012, **378**(1), 36–43 DOI: [10.1016/j.jcis.2012.04.044](https://doi.org/10.1016/j.jcis.2012.04.044)
- [3] Rankin, P. J.; Ginder, J. M.; Klingenberg, D. J.: Electro- and magneto-rheology, *Curr. Op. Coll. Interf. Sci.*, 1998, **3**(4), 373–381 DOI: [10.1016/S1359-0294\(98\)80052-6](https://doi.org/10.1016/S1359-0294(98)80052-6)
- [4] Sanchis, A.; Sancho, M.; Martínez, G.; Sebastián, J.; Muñoz, S.: Interparticle forces in electrorheological fluids: effects of polydispersity and shape, *Colloid Surf. A*, 2004, **249**(1-3), 119–122 DOI: [10.1016/j.colsurfa.2004.08.061](https://doi.org/10.1016/j.colsurfa.2004.08.061)
- [5] Olabi, A. G.; Grunwald, A.: Design and application of magneto-rheological fluid, *Mat. Design*, 2007, **28**(10), 2658–2664 DOI: [10.1016/j.matdes.2006.10.009](https://doi.org/10.1016/j.matdes.2006.10.009)
- [6] Bucchi, F.; Forte, P.; Frendo, F.; Musolino, A.; Rizzo, R.: A fail-safe magnetorheological clutch excited by permanent magnets for the disengagement of automotive auxiliaries, *J. Int. Mat. Sys. Struct.*, 2014, **25**(16), 2102–2114 DOI: [10.1177/1045389X13517313](https://doi.org/10.1177/1045389X13517313)
- [7] Peng, W.; Li, S.; Guan, C.; Li, Y.; Hu, X.: Ultra-precision optical surface fabricated by hydrodynamic effect polishing combined with magnetorheological finishing, *Optik*, 2018, **156**, 374–383 DOI: [10.1016/j.ijleo.2017.11.055](https://doi.org/10.1016/j.ijleo.2017.11.055)
- [8] Ayani, M.; Hosseini, L.: The Effect of Temperature and Electric Field on the Behavior of Electrorheological Fluids, in 4th Annual (International) Mechanical Engineering Conference (Isfahan University of Technology, Isfahan, Iran)
- [9] Mokeev, A. A.; Gubarev, S. A.; Korobko, E. V.; Bedik, N. A.: Microconvection heat transfer in electrorheological fluids in rotating electric field, *J. Phys.: Conf. Ser.*, 2013, **412**, 012008 DOI: [10.1088/1742-6596/412/1/012008](https://doi.org/10.1088/1742-6596/412/1/012008)
- [10] Spaggiari, A.: Properties and applications of Magnetorheological fluids, *Frattura ed Integrità Strutturale*, 2012, **7**(23), 48–61 DOI: [10.3221/IGF-ESIS.23.06](https://doi.org/10.3221/IGF-ESIS.23.06)
- [11] Wang, R.; Wang, Y.C.; Feng, C.Q.; Zhou, F.: Experimental Research on the Heat Transfer Characteristics of Electrorheological Fluid Shock Absorber, in Advances in Industrial and Civil Engineering, *Advanced Materials Research*, 2012, **594–597** (Trans Tech Publications Ltd), 2836–2839 DOI: [10.4028/www.scientific.net/AMR.594-597.2836](https://doi.org/10.4028/www.scientific.net/AMR.594-597.2836)
- [12] Nakamura, T.; Saga, N.; Nakazawa, M.: Thermal Effects of a Homogeneous ER Fluid Device, *J. Int. Mat. Sys. Struct.*, 2003, **14**(2), 87–91 DOI: [10.1177/1045389X03014002003](https://doi.org/10.1177/1045389X03014002003)